Nonlinear Properties of Soft Glass Waveguides

Steffensen, Henrik; Bang, Ole; Rottwitt, Karsten; Jepsen, Peter Uhd

Publication date:
2012

Document Version
Publisher's PDF, also known as Version of record

Link back to DTU Orbit

Citation (APA):
Steffensen, H., Bang, O., Rottwitt, K., & Jepsen, P. U. (2012). Nonlinear Properties of Soft Glass Waveguides. Kgs. Lyngby: Technical University of Denmark (DTU).

DTU Fotonik
Department of Photonics Engineering

Technical University
of Denmark

Nonlinear Properties of Soft Glass Waveguides

Henrik Steffensen
30 November 2012

Main Supervisor:
Professor Karsten Rottwitt, DTU Fotonik
Co-Supervisors:
Professor Ole Bang, DTU Fotonik
Professor Peter Uhd Jepsen, DTU Fotonik

Abstract

This thesis builds around the investigation into using soft glass materials for mid-infrared and THz applications. Soft glasses is a term that covers a wide range of chemical compositions where many are yet to be fully investigated. The work in this thesis is separated in two parts, the mid-infrared applications and the THz applications.

In the mid-infrared, it is investigated whether soft glasses are a suitable candidate for supercontinuum generation (SCG). A few commercially available fluoride fibers are tested for their zero dispersion wavelength (ZDW), a key property when determining the possibility of SCG in a fiber. A group of soft glasses, namely the chalcogenides, are known to display two photon absorption (TPA) which could potentially limit the SCG when this is initiated within the frequency range where this nonlinear process occur. An analytic model is presented to estimate the soliton self frequency shift (SSFS), another key element in SCG, when TPA is present. To show the validity of this model, it is used with chalcogenide fiber parameters from the literature to show that a frequency shift is limited due to the TPA effect.

It is only resent, that soft glass materials have come into focus for THz applications, thus these materials remain relatively unknown. A selection of GeAsSe chalcogenides is investigated to determine whether they have potential as transparent glasses for THz applications. In order to do so, these glasses are tested experimentally in both transmission and reflection measurements to determine the complex refractive index. Knowledge of the index and loss is key in determining if these glasses will be interesting candidates for future applications.

Henrik Steffensen
30 November 2012

Resume

Denne afhandling er bygget op omkring en undersøgelse om hvorvidt bløde glasser har et potentiale for at bruges til applikationer i det midt infrarøde og i THz området. Udtrykket bløde glasser dækker over en bred vifte af glasser med varierende kemiske sammensætninger hvor mange endnu ikke er undersøgt til bunds. Arbejdet i denne afhandling fokuser primært på to områder, superkontinuum generering i det midt infrarøde og på at undersøge en serie glasser i THz området.

Det undersøges om en række specifikke glasser er egnede kandidater til brug i superkontinuum generering. En række fluor baserede glas fibre fra kommercielle udbydere undersøges for deres nul-dispersion, en væsentlig parameter når det skal vurderes om en fiber er egnet til at bruges til superkontinuum generering. En af glas grupperne der ofte bruges som fiber i superkontinuum generering er chalcogenide. Men denne type glas har mulighed for to-photons tab, hvilket fører til øget tab i fibre af dette glas. I afhandlingen præsenteres en model der kan estimere hvor meget dette ulineære tab reducerer det frekvensskifte der er forårsaget er Raman effekten i fiberen og som ligeledes er et væsentligt element i at opnå et bredt superkontinuum spektrum. For at understrege denne effekt er modellen brugt på fiber parametre fra litteraturen, hvormed det kan vises at denne effekt begrænser det frekvensskifte der ville kunne opnås hvis denne effekt ikke var til stede.

Det er kun i nyere tid at man er begyndt at interessere sig for brugen af bløde glasser i THz området. Derfor er disse materialer stadig relativt ukendte ved disse frekvenser. I denne afhandling undersøges en række glasser af GeAsSe chalcogenid typen derfor, for at se om de udviser et potentiale. De testes eksperimentelt, både i transmissions og refleksions målinger, for at bestemme deres brydningsindeks og tab. Ud fra denne viden kan det afklares om disse glasser har et potentiale for at arbejde videre med dem til THz brug.

Preface

This thesis is submitted in candidacy for the PhD degree from the Technical University of Denmark (DTU). The project has been carried out at DTU Fotonik - Department of Photonics Engineering from 2009 to 2011 with Professor Karsten Rottwitt as main supervisor and Professors Ole Bang and Peter Uhd Jepsen as co-supervisors. The work was mainly carried out at DTU Fotonik, but a three month external stay was spent at School of Physics, University of Sydney, Australia with Associate Professor Stuart Jackson.

Acknowledgments

First of all, I would like to thank my supervisors, Professors Karsten Rottwitt, Ole Bang and Peter Uhd Jepsen. Karsten for introducing me to nonlinear optics and parametric amplifiers, Ole and Peter for teaching me all about Supercontinuum Generation and THz optics respectively. I also thank them all for always having the time for questions and discussions. Secondly I thank Associate Professor Stuart Jackson for being a good host during my visit in Sydney. I also thank Jens Kristian Lyngsø and NKT Photonics for use of their facilities and equipment and Dr. Rongping Wang at the Laser Physics Centre, Australia National University in Canberra for providing chalcogenide samples. Furthermore I would like to thank all my friends and coworkers at DTU Fotonik and University of Sydney I have had the opportunity to work with throughout this project including Lars Rishøj, Martin Pedersen, Christian Agger, Mikkel Heuck, Johan Ott, Daniel Buccoliero, Darren Hudson, Alex Judge, Krzysztof Iwaszczuk, Jonas Due Buron, Drew Strikwerda, Tianwu Wang and Maksim Zalkovskij.

Last, but certainly not least, I would like to thank Ange Woods, the rest of my family and my friends for their support and patience throughout this project.

Henrik Steffensen
30 November 2012

List of Publications

Scientific Journals

- C. Agger, C. Petersen, S. Dupont, H. Steffensen, J. K. Lyngsø, C. L. Thomsen, J. Thøgersen, S. R. Keiding and O. Bang, "Supercontinuum generation in ZBLAN fibers – detailed comparison between measurement and simulation," *Journal of Optical Society of America B*, **29**(3): 635–645 (2012)

- H. Steffensen, C. Agger and O. Bang, "Influence of two-photon absorption on soliton self-frequency shift," *Journal of Optical Society of America B*, **29**(3): 484–492 (2012)

- D. Buccoliero, H. Steffensen, H. Ebendorff-Heidepriem, T. M. Monro and O. Bang, "Midinfrared optical rogue waves in soft glass photonic crystal fiber," *Optics Express*, **19**(19): 17973–17978 (2011)

- H. Steffensen, J. R. Ott, K. Rottwitt and C. J. McKinstrie, "Full and semi-analytic analysis of two-pump parametric amplification with pump depletion," *Optics Express*, **19**(7): 6648–6656 (2011)

- D. Buccoliero, O. Bang, H. Steffensen, H. Ebendorff-Heidepriem and T. M. Monro, "Thulium pumped high power supercontinuum in loss-determined optimum lengths of tellurite photonic crystal fiber," *Applied Physics Letters*, **97**: 061106 (2010)

Conference Proceedings

- H. Steffensen, K. Rottwitt, P. U. Jepsen and O. Bang, "Influence of two-photon absorption on soliton self-frequency shift," *Proceedings of Nonlinear Optics: Materials, Fundamentals and Applications (NLO)*, NWE16 (2011)

- C. Agger, C. Petersen, S. Dupont, H. Steffensen, J. K. Lyngsø, C. L. Thomsen, S. R. Keiding and O. Bang, "Supercontinuum generation in ZBLAN fibers –

detailed comparison between measurement and simulation," *Proceedings of CLEO – Conference on Lasers and Electrooptics*, CThBB2 (2011)

Book Chapters

- K. Rottwitt, A. C. Brunetti, J. Lægsgaard, J. Weirich, L. S. Rishøj, X. Liu, L. Scolari, M. E. V. Pedersen, A. T. Pedersen, H. Steffensen and L. Wei, "Enhancing the capacity of light," *Beyond optical horizons - Today and tomorrow with photonics*, 75–87 (2009)

Contents

1

Introduction

Mid-infrared and THz optical technologies are receiving an increasing amount of interest in recent years. The interest in these frequencies is based in the possibilities with light at these frequencies to create spectroscopy devices useful for any range of applications within testing of physical, biological and chemical sensing [1, 2, 3, 4].

There has been great interest in creating new sources such as fiber lasers [5], quantum cascade lasers [6] and frequency combs [7] in the mid-infrared and in THz sources such as optical rectification in lithium niobate [8]. In resent years, there has also been great interest in creating broadband sources covering as much as the mid-infrared spectrum as possible. Mainly these sources are based on Supercontinuum Generation (SCG) in materials that are transparent in the mid-infrared such as soft glasses [9, 10, 11].

In the THz regime, novel materials are also of an interest, as work has been carried out in creating THz guiding optical fibers using low loss polymers [12, 13]. Soft glass materials appear as a promising alternative for the use of polymers. Some of the soft glasses, namely tellurite and chalcogenide, are highly nonlinear in the mid-infrared [14], they might also have a substantial nonlinearity in the THz spectrum which would make them candidates for nonlinear optical devices in the THz range.

This thesis begins with an outline of what soft glasses are comprised of and with a discussion of their known properties. Following this the soft glasses are investigated in respect to their usability as a medium in SCG, specifically the focus is on the dispersion of commercially available fluoride fibers, to see whether these are an option, secondly the focus is on to which extend the Two-Photon Absorption (TPA) that is inherently present in chalcogenide reduces the possibilities of using these fibers for SCG. The soft glass materials are also considered for use in the THz regime, a range of chalcogenide glasses from the GeAsSe family is tested to investigate their potential in this spectral range.

2

Soft Glass Materials

Soft glass materials are a range of materials that is getting an increasing amount of interest in research. Common for these materials are, as the name implies, the amorphous glass structure and the low melting temperature for these glasses compared to the more commonly used silica glass. The soft glass materials are composed of a whole range of different glasses, which for the main can be placed in three overall groups, namely fluoride glasses, tellurite glasses and chalcogenide glasses. Besides the common denominator in the lower melting temperature, all these glasses appear to have a significantly lower loss than silica in the mid and far-infrared region. First in this chapter will be a introduction to the chemical compositions of these materials, after which the glass properties will be discussed.

2.1 Chemical Compositions

2.1.1 Fluoride Glasses

Flouride glasses are a generally non-oxide range of glasses based on metal fluorides. The glasses within this class can be further grouped into such sub-groups as fluorozirconate glasses, based on zirconium fluoride, fluoroaluminate glasses, based on aluminium fluoride, and fluorophosphate glass, which differs from the other two as it is a compound of metal fluorides and metaphosphate containing oxygen.

Fluoride glasses are often referred to by acronyms of the metal fluorides the glasses are based on, such examples are ZBLAN (ZrF_4-BaF_2-LaF_3-AlF_3-NaF), ZBLA (ZrF_4-BaF_2-LaF_3-AlF_3), CLAP (CdF_2-LiF-AlF_3-PbF_2) and BZnYbT (BaF_2-ZnF_2-YbF_3-ThF_4) [15]. As the materials are all compound glasses, the concentration of each metal fluoride can be reasonably freely chosen at production. ZBLAN is the most used of these glasses and is also regarded as the most stable fluoride glass [16]. It is currently used in a range of applications such as doped with rare earth ions for fiber lasers and amplifiers and for mid-infrared transmission fibers [15, 16].

Flouride fiber is soluble in water, and the material are thus prone to water intruding into the material from the air if not properly sealed [17, 11].

2.1.2 Tellurite Glasses

Tellurite differ from flouride glasses in it being based mainly on a single molecule, namely tellurium dioxide in its orthorhombic mineral tellurite form, β-TeO_2. In its pure form, tellurite forms a crystal structure, however in combination with small molar concentrations of other compounds, it will form a glass structure. Examples of tellurite glass compositions include $75TeO_2$-$20ZnO$-$5Na_2O$ [18], (95-x)TeO_2-(x)Li_2O-$5TiO_2$ [19] and $75TeO_2$-$12ZnO$-$5PbO$-$3PbF_2$-$5Nb_2O_5$ [20]. As with fluoride glasses, the composition of the added chemical compounds are variable, leaving with many various options of creating a tellurite glass.

2.1.3 Chalcogenide Glasses

Chalcogenide is a chemical compound consisting of at least one chalcogen ion and at least one other ion being more electropositive than the chalcogen. Chalcogen ion are all ions in group 16 of the periodic table, although also oxygen is included in this group, chalcogen and the term chalcogenide usually excludes all oxides and refers primarily to sulfides, selenides and tellurides [21]. Chalcogenides are also a group of non-crystalline or amorphous semiconductors which causes these materials to display two-photon absorption in the near-infrared [22]. However it is reported that, differing from crystalline semiconductors, amorphous chalcogenide is inherently p-type [23], meaning that at excitation, only free holes are created while free electrons are not.

Chalcogenide glasses also has potential as photonic chip material as it is possible to use planar wafer technology known from the silicon chip production to modify these glasses.

2.2 Comparison

In the near-infrared regime, silica is the preferred material as it is easy to handle and has a low loss. As we go into the mid- and far-infrared, the loss in silica is greatly increases which is why other glasses is preferred in this range. In Table 2.1 is listed some key material properties of soft glasses and silica for comparison [24, 25, 14, 26, 27, 28, 18, 29, 9, 30, 31, 11, 32]. As mentioned earlier, there is a great number of different chemical compositions available or making soft glasses, and with many of them not being fully studied yet, thus these material property values are approximate only.

Table 2.1: Properties of soft glasses in comparison with silica

	Silica	Flouride	Tellurite	Chalcogenide
Refractive index, n	1.46	1.5	1.8–2.3	2.4–2.8
Nonlinear index, n_2 [m^2/W]	2.7×10^{-20}	2.1×10^{-20}	6×10^{-19}	10×10^{-18}
Raman Stokes shift [THz]	13	17.7	22.5	6.8
Near- and mid-infrared transmission range [μm]	0.2–2.5	0.2–7	0.4–5.0	0.8–16
Fiber loss [dB/km]	0.2	40	2.9×10^3	0.4
at [μm]	1.5	2.0	1.55	6.5
ZDW (material) [μm]	1.3	1.6	2.5	4–5
Glass transition temp* [°C]	1000	300	300	300
Band gap* [nm]	120		440–670	516–700

($*$): Highly dependent on the chemical composition.

As it shows from the table, fluoride fibers are those that closest resemble silica, as they have comparable nonlinearity and fiber dispersion, though the loss is much higher. In comparison, chalcogenide and tellurite glasses both have a substantially higher Zero Dispersion Wavelength (ZDW) and nonlinearity.

All the soft glass fibers have a much lower glass transition temperature than silica, causing the drawing temperature to be set much lower when drawing these materials into fibers. For flouride glasses especially, the glass melting temperature is only slightly higher than the glass transition temperature, leaving it practically impossible to create flouride fibers with a hole structure in them. For chalcogenide and tellurite, several examples have been reported of succesfully made Photonic Crystal Fibers (PCFs) [33, 21, 9]. Furthermore, soft glass materials are more difficult to handle than silica fibers, they are more brittle and it is thus not as straight forward to, for instance splice fibers together, as it is with silica.

3

Mid-Infrared Supercontinuum Generation in Soft Glass Materials

Broadband light sources in the mid-infrared range, 2-15 μm, are of significant interest due to the many infrared applications in astronomy [34, 35], spectroscopy of biological [2, 3] and chemical [1] samples, IR microscopy [36], gas sensing [37] and military countermeasures [38]. Broadband light sources based on SCG [39] in silica fibers are widely used in the visible and near-infrared wavelength range [40]. However a mid-infrared supercontinuum light source cannot use silica fibers because of the loss edge at around 2.2 μm. Instead other glasses with a higher transparency in the mid-infrared can be used, such as ZBLAN [41, 42], bismuth [28], tellurite [20, 9] or chalcogenide [43, 10]. Chalcogenide glasses generally have a nonlinear index two orders of magnitude higher than silica, whereas bismuth and tellurite have one order of magnitude higher and finally ZBLAN have a nonlinear index comparable to that of silica [27], see also Table 2.1. The material ZDW is also higher than that of silica with chalcogenide having the highest at around 4-5 μm depending on the chemical composition [28].

This chapter begins with a brief discussion of SCG in general then discusses in more detail the possibilities and perspectives of generating Supercontinuum (SC) in soft glass materials. Afterwards a section is dedicated to discussing the importance of knowing the dispersion of the fiber used for a SCG, with description of how this was measured and the results obtained. Lastly I present the work on an analytical model to predict the Soliton Self Frequency Shift (SSFS), which is essential in SCG. With this model I then show how TPA in especially chalcogenide affects the red-shift of solitons.

3.1 Obtaining Supercontinuum Generation

The fundamentals in SCG is pumping the nonlinear fiber close to the ZDW and by Modulation Instability (MI) or soliton fission to generate fundamental solitons and have them redshift [39]. Thus the location of the ZDW is one of the key elements in obtaining SCG as well as the possibility to have them red-shift far while also forming dispersive waves in the blue region of the spectrum. It is possible to use any laser as the optical pumping source for SCG, however for simplicity, a fiber laser would be preferable, as with a fiber laser it is possible to avoid free space coupling. Two of the most available fiber laser are ytterbium fiber lasers, usually with a wavelength around 1064 nm, or erbium fiber laser, with a typical wavelength around 1564 nm. Using either of these, standard silica fiber is not a good choice here, as the ZDW is typically around 1317 nm for standard SMF28 fiber [44]. Various methods are thus used to engineer the ZDW of the fiber to enable the use of fiber lasers, methods such as using PCFs [45, 39] that can be dispersion engineered for optimal SCG [46], tapers [47, 48, 43, 49] or by the use of silica fiber to either redshift the pulse [50] or to initialize the SCG [41] before coupling to a soft-glass fiber. Other advantages of using PCFs include the possibility of creating the fiber endlessly single-moded and having a tighter confinement in the fiber thus increasing the nonlinear constant.

Of the three material options, only step-index chalcogenide [51, 52] and ZBLAN fibers [53, 54] are readily available commercially. The chalcogenide fibers available are usually offered based either on arsenic selenide (As_2Se_3) or arsenic sulfide (As_2S_3). Chalcogenide have the highest nonlinear index of the two, and would thus be an interesting candidate if not for the high ZDW which makes it challenging to use a fiber laser [43]. ZBLAN on the other hand have a lower ZDW that more easily allows for using a fiber laser to pump the SCG. If looking at non-commercial fiber, tellurite and chalcogenide are both very interesting, as it is possible to create PCFs in these glasses [33, 21, 9], which makes it possible to tailor the dispersion to suit SCG [46].

3.2 Dispersion

Knowing the ZDW is essential in good SCG and since the soft glasses are relatively un-investigated together because of the high degree of variation in the composition of the materials between suppliers, it is necessary to investigate each specific fiber considered for SCG. First the experimental setup is described with a description of the fibers tested and the results of the measurements in the following section.

3.2.1 Experiment

To measure the dispersion of the fibers, a low coherence interferometric setup is used [55, 56]. The experiment is based on a broadband source or a tunable laser where the light is divided in two, the one arm being propagated through the fiber, the other is propagated through air alone. The two light beams are then combined and sent to a Optical Spectrum Analyzer (OSA) to measure the power spectrum. A schematic of the experiment is shown in Fig. 3.1. In this experiment, a SC source is used as the broadband source. This experiment is only suitable for Single-Mode Fibers (SMFs), as it is required that the light propagating through the fiber is confined in a single mode, otherwise it is not possible to calculate the dispersion of the fiber. The dispersion can be found as

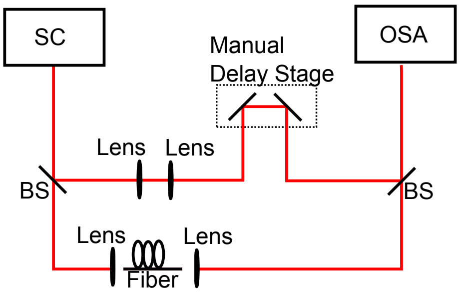

Figure 3.1: Schematic of the dispersion measurement setup. A SC laser is used as the light source, the light is split in two parts, one to propagate through the test fiber, the other is propagated through air (reference). In the reference beam, the same two lenses are placed to reduce any effect the lenses used to couple in and out of the fiber might have. The manual delay stage is used to adjust the length of the reference arm to increase the visibility of the interference pattern measured with the OSA.

$$D(\lambda) = \frac{1}{Lc}\left[\frac{1}{\Delta\lambda^2}\left(2\lambda\cdot\Delta\lambda - \lambda^2\frac{d\Delta\lambda}{d\lambda}\right)\right], \tag{3.2.1}$$

where L is the length of the fiber and $\Delta\lambda$ is the distance in wavelength between the peaks in the interference pattern. The derivation of this equations is described in detail in App. A.1, is it based on differentiating the phase of the combined electric field, where the derivative of the phase can be estimated based on the periodicity of the interference pattern.

If the fiber is not single moded, it is highly likely that some light is coupled into the higher order modes. In this case, the power spectrum measured does not comprise solely of the light traveled through the reference arm and the fundamental mode of the fiber, and the premise behind Eq. (3.2.1) is no longer valid. However the experiment can still be used to give an inclination of where the ZDW will be. If only the light traveling through the fiber is measured, then if any light is coupled into the higher order modes, an interference pattern will emerge as the propagation constant of the modes is not the same. Thus changing the coupling of the light to reduce the interference pattern as much as possible will ensure that only little light will couple into the higher order modes. If the power in the fundamental mode can be assumed much greater than the light in any other mode, Eq. (3.2.1) can still be used to give an estimated dispersion curve. It is however important to note that the error in this measurement is much greater than when measuring on a SMF, and should only be used to give a qualitative estimate of where the ZDW is.

3.2.2 Fibers Measured

ZBLAN fibers from two different suppliers were considered for use, one being IrPhotonics [53] providing samples from both an old and a new batch, denoted (1) and (2) respectively, and from FiberLabs [54] as the second manufacturer. As the fibers are from different manufacturers, the composition of the fibers vary between IrPhotonics and FiberLabs. IrPhotonics changed the composition of the fiber during the investigation in order to obtain a less brittle fiber. However in which way this was done was not disclosed, thus the fibers are treated as being different. Further details of the fibers are shown in Table 3.1.

Table 3.1: Fibers tested for ZDW

Fiber	NA	Core Diameter	Cut-off λ
IrPhotonics (1)	0.17	9μm	2μm
IrPhotonics (2)	0.17	9μm	2μm
FiberLabs	0.2	10.7μm	2.8μm

Fig. 3.2 shows the measured dispersion for the three fibers. It shows the two fibers having a ZDW at 1832nm and 1846nm respectively for fibers (1) and (2), and at 1583nm for the fiber from FiberLabs. This is for all fibers well below the cut-off wavelength, and the dispersion measurements should thus only be regarded qualitatively, however it clearly shows a significant difference in location of the ZDW. As it is optimum for SCG to pump just slightly above the ZDW, it shows that if using either of the IrPhotonics fibers, the pump wavelength should be above roughly 1850nm, which could make thulium doped fiber lasers an option, or if using the FiberLabs fiber, a pump around roughly 1600nm is necessary.

Furthermore, attempts were done to measure dispersion on drawn tellurite fiber for use in simulations of SCG [9], however these yielded no result as the fiber was poorly shaped and proved impossible to sufficiently couple into the fundamental mode.

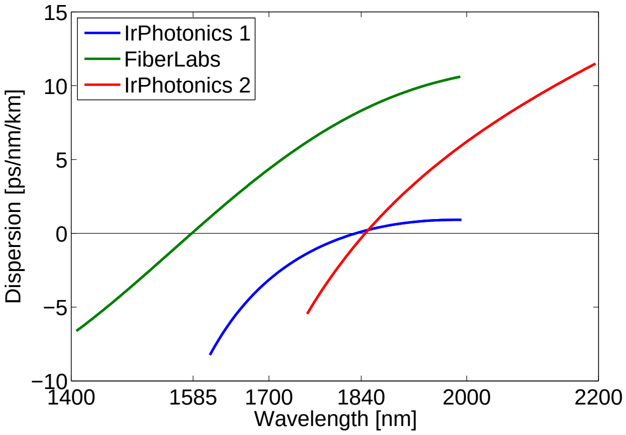

Figure 3.2: The measured dispersion for three different fibers. Two different fibers from commercial supplier IrPhotonics and one from commercial supplier FiberLabs. The two fibers have roughly the same ZDW, with (1) being at 1832nm and (2) being at 1846nm, whereas the fiber from FiberLabs have a ZDW at 1583nm.

3.3 Soliton Self-Freguency Shift Model by Method of Moments

The SSFS effect was analytically shown by Gordon [57] by looking at the Raman amplification as a perturbation to the Nonlinear Schrödinger (NLS). Later works extended the description by including self-steepening and Third Order Dispersion (TOD) for long pulses [58] and linear losses [59]. Judge *et. al.* extended the original model to be used in fiber tapers [60, 61] and recent work has been shown that includes the full Raman description as well as linear loss, TOD and self-steepening effects by the use of method of moments [62]. As chalcogenide is increasingly being used as a new material for SCG, it is now necessary to extend the previous work to also include TPA which is present in various chalcogenide materials, for instance As_2Se_3. As it was shown that including loss in the description of SSFS had a great effect of the predicted red-shift [59], it is expected that TPA will further reduce the red shift.

The NLS equation expressed as [63],

$$\partial_z u(z,t) = -\mathrm{i}\frac{\beta_2}{2}\partial_t^2 u(z,t) + \mathrm{i}\gamma_0^r |u(z,t)|^2 u(z,t), \tag{3.3.1}$$

where $u(z,t)$ is the complex envelope op the electric field at carrier frequency ω_0, β_2 is the Group Velocity Dispersion (GVD) coefficient, and γ_0^r is the real part of the nonlinear constant

$$\gamma_0^r = \frac{\omega_0 n_2}{c A_{\text{eff}}}, \tag{3.3.2}$$

with n_2 is the nonlinear refractive index, c is the speed of light and A_{eff} is the effective area, has a fundamental soliton solution given by

$$u(z,t) = \sqrt{P_0}\text{sech}\left(\frac{t}{T_0}\right)\exp\left(-\mathrm{i}\frac{\beta_2}{2T_0^2}z\right), \tag{3.3.3}$$

with T_0 as the pulse width, P_0 is the peak power and with the two constraints that $\beta_2 < 0$, i.e. anomalous dispersion, and that

$$\frac{\gamma_0^r P_0 T_0^2}{|\beta_2|} = 1. \tag{3.3.4}$$

This solution is named the fundamental soliton and it will propagate unchanged through the fiber. However, the NLS equation neglects effects such as Raman scattering, self-steepening and TPA. Thus a more accurate description of the propagation in a fiber is the Generalized Nonlinear Schrödinger (GNLS) equation, given as [62]

$$\begin{aligned}\partial_z u(z,t) = &-\frac{\alpha}{2}u(z,t) + \mathrm{i}\sum_{m\geq 2}\frac{\mathrm{i}^m\beta_m}{m!}\partial_t^m u(z,t)\\ &+\mathrm{i}\sum_{n\geq 0}\frac{\mathrm{i}^n\gamma_n}{n!}\partial_t^n\left\{u(z,t)\int R(t')|u(z,t-t')|^2\mathrm{d}t'\right\},\end{aligned} \tag{3.3.5}$$

where α is the linear loss, β_m is the m'th derivative of the propagation constant with respect to ω, γ_n is the n'th derivative where by the zero'th derivative is meant the nonlinear constant itself as given by [64]

$$\gamma_0 = \frac{\omega_0 n_2}{c A_{\text{eff}}} + i\frac{\beta_{\text{TPA}}}{2A_{\text{eff}}}, \tag{3.3.6}$$

with nonlinear loss, β_{TPA}, included in the imaginary part of the nonlinear constant. The integral is performed over the entire domain, e.g. $\int \mathrm{d}t = \int_{-\infty}^{\infty}\mathrm{d}t$ and

$$R(t) = (1 - f_R)\delta(t) + f_R h_R(t), \tag{3.3.7}$$

is the time response function for the nonlinear susceptibility where $h_R(t)$ is the Raman response function and f_R is the fractional Raman response.

The derivation of the SSFS model is based on utilizing the Method of Moments (MoM) [65, 58]. The more common variational technique cannot be applied because the GNLS equation, Eq. (3.3.5), does not have a Lagrangian when the temporally asymmetric nonlocal Raman term is included. Had the nonlocality been symmetric, then variational techniques could have been applied [66, 67].

The MoM require a relevant ansatz to be chosen. Since the solution to the NLS is a fundamental soliton, the ansatz is assumed to follow a similar shape, thus the ansatz is chosen as

$$u(z,t) = \sqrt{P_0(z)}\mathrm{sech}\left(\frac{t-t_c(z)}{T_0(z)}\right)\exp\left[\mathrm{i}\Phi(z) - \mathrm{i}b(z)(t-t_c(z)) - \mathrm{i}\mu(z)(t-t_c(z))^2\right], \tag{3.3.8}$$

where P_0 is the peak power, T_0 is the pulse width in time, t_c is the pulse shift in time, Φ is the time-independent phase shift, b is the angular frequency shift and finally μ is the quadratic chirp. All these pulse characteristics is assumed to vary with z.

In this model for SSFS, the two first terms of each sum in the GNLS is included, namely the two dispersion terms, GVD and TOD, and the nonlinear terms which included the Kerr nonlinearity, the Raman scattering and the self-steepening. Thus the governing equation is assumed to be

$$\begin{aligned}\partial_z u(z,t) = &-\frac{\alpha}{2}u(z,t) - \mathrm{i}\frac{\beta_2}{2}\partial_t^2 u(z,t) + \frac{\beta_3}{6}\partial_t^3 u(z,t)\\ &+ \mathrm{i}\gamma_0 u(z,t)\int R(t')|u(z,t-t')|^2\mathrm{d}t' - \gamma_1\partial_t\left\{u(z,t)\int R(t')|u(z,t-t')|^2\mathrm{d}t'\right\}.\end{aligned} \tag{3.3.9}$$

The MoM require the same number of moments as the number of included pulse characteristics, however as b, P_0, T_0, μ and t_c is not dependent on the phase shift, only 5 moments is required. These 5 moments are

$$Q(z) = \int |u(z,t)|^2\mathrm{d}t, \tag{3.3.10a}$$

$$P_M(z) = \frac{1}{2}\int (u(z,t)\partial_t u^*(z,t) - u^*(z,t)\partial_t u(z,t))\mathrm{d}t, \tag{3.3.10b}$$

$$I_1(z) = \int t|u(z,t)|^2\mathrm{d}t, \tag{3.3.10c}$$

$$I_2(z) = \int (t-t_c)^2|u(z,t)|^2\mathrm{d}t, \tag{3.3.10d}$$

$$I_3(z) = \int (t-t_c)(u^*(z,t)\partial_t u(z,t) - u(z,t)\partial_t u^*(z,t))\mathrm{d}t. \tag{3.3.10e}$$

If necessary, it is possible to define a 6th moment to derive an equation for the change in Φ [68].

The evolution equations for the 5 pulse characteristics are then found by first calculating each moment by inserting the ansatz. These are then differentiated with respect to z which, after rewriting, results in 5 differential equations for the 5 pulse characteristics as a function of the derivatives of the moments. These derivatives can then be found by differentiating Eq. (3.3.10) with respect to z, inserting Eq. (3.3.9) followed by the ansatz. This derivation of the coupled differential equations can be seen in more detail in App. A.2.

The result of this is these 5 coupled differential equations,

$$\begin{aligned}\partial_z b = &-\frac{8}{15}\frac{(\gamma_0^r + b\gamma_1^r)P_0}{T_0} f_R \int h_R(t) A_1\left(\frac{t}{T_0}\right)\mathrm{d}t \\ &+ \frac{4}{3}\mu\gamma_1^r P_0\left[1 - f_R + f_R\int h_R(t)B_1\left(\frac{t}{T_0}\right)\mathrm{d}t\right] \\ &- \frac{4}{3}\mu(\gamma_0^i + b\gamma_1^i)P_0T_0 f_R\int h_R(t)A_2\left(\frac{t}{T_0}\right)\mathrm{d}t \\ &- \frac{4}{5}\frac{\gamma_1^i P_0}{T_0^2}\left[1 - f_R + f_R\int h_R(t)B_2\left(\frac{t}{T_0}\right)\mathrm{d}t\right] \\ &- 4\left(\frac{\pi^2}{9} - \frac{2}{3}\right)\mu^2\gamma_1^i P_0 T_0^2\left[1 - f_R + f_R\int h_R(t)B_3\left(\frac{t}{T_0}\right)\mathrm{d}t\right]\end{aligned} \tag{3.3.11a}$$

$$\begin{aligned}\partial_z t_c = &\, b(\beta_2 + b\beta_3) + \frac{1}{2}\beta_3\left[\frac{\pi^2}{3}\mu^2T_0^2 + \frac{1}{3T_0^2} - b^2\right] \\ &+ \gamma_1^r P_0\left[1 - f_R + f_R\int h_R(t)B_4\left(\frac{t}{T_0}\right)\mathrm{d}t\right] \\ &- \frac{2}{3}(\gamma_0^i + b\gamma_1^i)P_0T_0 f_R\int h_R(t)A_2\left(\frac{t}{T_0}\right)\mathrm{d}t \\ &- 2\left(\frac{\pi^2}{9} - \frac{2}{3}\right)\mu\gamma_1^i P_0 T_0^2\left[1 - f_R + f_R\int h_R(t)B_3\left(\frac{t}{T_0}\right)\mathrm{d}t\right]\end{aligned} \tag{3.3.11b}$$

$$\begin{aligned}\partial_z T_0 = &\, 2\mu T_0(\beta_2 + b\beta_3) + \frac{8}{\pi^2}\gamma_1^r P_0 f_R\int h_R(t)A_3\left(\frac{t}{T_0}\right)\mathrm{d}t \\ &+ \frac{4}{\pi^2}(\gamma_0^i + b\gamma_1^i)P_0T_0\left[1 - f_R + f_R\int h_R(t)B_5\left(\frac{t}{T_0}\right)\mathrm{d}t\right] \\ &- \left(\frac{4}{3} - \frac{12}{\pi^2}\right)\mu\gamma_1^i P_0T_0^2 f_R\int h_R(t)A_4\left(\frac{t}{T_0}\right)\mathrm{d}t\end{aligned} \tag{3.3.11c}$$

$$\begin{aligned}\partial_z P_0 = &-\alpha P_0 - 2\mu P_0(\beta_2 + b\beta_3) - \left(\frac{8}{\pi^2} + \frac{8}{15}\right)\frac{\gamma_1^r P_0^2}{T_0} f_R \int h_R(t) A_5\left(\frac{t}{T_0}\right)\mathrm{d}t \\ &- \left(\frac{4}{3} + \frac{4}{\pi^2}\right)(\gamma_0^i + b\gamma_1^i)P_0^2\left[1 - f_R + f_R\int h_R(t) B_6\left(\frac{t}{T_0}\right)\mathrm{d}t\right] \\ &- \frac{12}{\pi^2}\mu\gamma_1^i P_0^2 T_0 f_R \int h_R(t) A_6\left(\frac{t}{T_0}\right)\mathrm{d}t \end{aligned} \tag{3.3.11d}$$

$$\begin{aligned}\partial_z \mu = &(\beta_2 + b\beta_3)\left(\frac{2}{\pi^2}\frac{1}{T_0^4} - 2\mu^2\right) + \frac{2}{\pi^2}\frac{(\gamma_0^r + b\gamma_1^r)P_0}{T_0^2}\left[1 - f_R + f_R\int h_R(t) B_7\left(\frac{t}{T_0}\right)\mathrm{d}t\right] \\ &- \left(\frac{8}{15} - \frac{4}{\pi^2}\right)\frac{\mu\gamma_1^r P_0}{T_0} f_R \int h_R(t) A_7\left(\frac{t}{T_0}\right)\mathrm{d}t - \frac{76}{15\pi^2}\frac{\gamma_1^i P_0}{T_0^3} f_R \int h_R(t) A_8\left(\frac{t}{T_0}\right)\mathrm{d}t. \end{aligned} \tag{3.3.11e}$$

where γ_n^r and γ_n^i are the real and imaginary parts of γ_n respectively.

The eight $A_n(x)$ functions,

$$A_1(x) = \frac{15}{8}\mathrm{csch}^4(x)\left[4x + 2x\cosh(2x) - 3\sinh(2x)\right] \tag{3.3.12a}$$

$$A_2(x) = 3x\,\mathrm{csch}^3(x)\left[x\cosh(x) - \sinh(x)\right] \tag{3.3.12b}$$

$$A_3(x) = \frac{1}{4}\mathrm{csch}^4(x)\left[-\left(2x^3 + 6x\right)\cosh(2x) + 9x^2\sinh(2x) - 4x^3 + 6x\right] \tag{3.3.12c}$$

$$A_4(x) = \frac{3}{\pi^2 - 9}x\,\mathrm{csch}^3(x)\left[\left(3x^3 + \pi^2 x\right)\cosh(x) - \left(6x^2 + \pi^2\right)\sinh(x)\right] \tag{3.3.12d}$$

$$\begin{aligned}A_5(x) = &\frac{15}{8\pi^2 + 120}\mathrm{csch}^4(x)\left[\left(18x^2 - 3\pi^2\right)\sinh(2x) - \left(4x^3 + 12x - 2\pi^2 x\right)\cosh(2x)\right. \\ &\left.-8x^3 + 12x + 4\pi^2 x\right]\end{aligned} \tag{3.3.12e}$$

$$\begin{aligned}A_6(x) = &\frac{1}{304}\mathrm{csch}^5(x)\left[\left(68\pi^2x^2 - 180x^2 + 75\pi^2 - 450\right)\cosh(3x) - \left(158\pi^2 x - 720x\right)\sinh(3x)\right. \\ &\left.+ \left(412\pi^2x^2 - 2700x^2 - 75\pi^2 + 450\right)\cosh(x) - \left(306\pi^2 x - 2520x\right)\sinh(x)\right]\end{aligned} \tag{3.3.12f}$$

$$\begin{aligned}A_7(x) = &\frac{15}{8\pi^2 - 60}\mathrm{csch}^4(x)\left[16x^3 + 4\pi^2 x - 6x + \left(8x^3 + 2\pi^2 x + 6x\right)\cosh(2x)\right. \\ &\left.- \left(18x^2 + 3\pi^2\right)\sinh(2x)\right]\end{aligned} \tag{3.3.12g}$$

$$A_8(x) = \frac{45}{152}\mathrm{csch}^5(x)\left[8x\sinh(3x) + 28x\sinh(x) - \left(2x^2 + 5\right)\cosh(3x) - \left(30x^2 - 5\right)\cosh(x)\right] \tag{3.3.12h}$$

is normalized such that $A_n(x \to 0) = x$, while the seven $B_n(x)$ functions

$$B_1(x) = \frac{3}{2}\operatorname{csch}^4(x)\left[\left(6x^2-1\right)\cosh(2x) - 8x\sinh(2x) + 12x^2 + 1\right] \tag{3.3.13a}$$

$$B_2(x) = \frac{5}{12}\operatorname{csch}^5(x)\left[7\sinh(3x) + 27\sinh(x) - 3x\cosh(3x) - 45x\cosh(x)\right] \tag{3.3.13b}$$

$$B_3(x) = \frac{3}{\pi^2-6}\operatorname{csch}^3(x)\left[\left(4x^3+\pi^2 x\right)\cosh(x) - \left(6x^2+\pi^2\right)\sinh(x)\right] \tag{3.3.13c}$$

$$\begin{aligned}B_4(x) = {}&\frac{1}{36}\operatorname{csch}^5(x)\left[\left(18x^2+61\right)\sinh(3x) + \left(54x^2+297\right)\sinh(x)\right.\\ &\left.-48x\cosh(3x) - 432x\cosh(x)\right]\end{aligned} \tag{3.3.13d}$$

$$B_5(x) = \operatorname{csch}^3(x)\left[3x^2\sinh(x) - 2x^3\cosh(x)\right] \tag{3.3.13e}$$

$$B_6(x) = \frac{3}{\pi^2+3}\operatorname{csch}^3(x)\left[\left(3x^2-\pi^2\right)\sinh(x) - \left(2x^3-\pi^2 x\right)\cosh(x)\right] \tag{3.3.13f}$$

$$B_7(x) = \frac{3}{2}\operatorname{csch}^4(x)\left[4x\sinh(2x) - \left(2x^2+1\right)\cosh(2x) - 4x^2 + 1\right], \tag{3.3.13g}$$

are normalized such that $B_n(x \to 0) = 1$. Not all these functions are linearly independent, it shows that

$$A_5(x) = \frac{1}{\pi^2+15}\left[\pi^2 A_1(x) + 15A_3(x)\right] \tag{3.3.14a}$$

$$A_8(x) = \frac{1}{\pi^2-6}\left[\pi^2 A_2(x) - 6A_6(x)\right] \tag{3.3.14b}$$

$$B_6(x) = \frac{1}{\pi^2+3}\left[9B_5(x) + \left(\pi^2-6\right)B_3(x)\right] \tag{3.3.14c}$$

$$B_7(x) = \frac{1}{\pi^2}\left[2\pi^2 B_2(x) + \left(2\pi^2-12\right)B_3(x) - 3\pi^2 B_4(x) + 12B_5(x)\right]. \tag{3.3.14d}$$

It is thus only necessary to calculate integrals over 11 functions and not the 15 mentioned A_n and B_n functions, reducing the computational need.

Since the first order parameters, β_2 and γ_0, appear as linear expansions, it is possible to introduce a moving frame of reference [62]. The moving frame is based on using a soliton with a fixed carrier frequency, ω_0, with the dispersion and nonlinearity parameters evaluated at this frequency and then to update this frequency to follow the red-shift as $\omega_0(z+dz) = \omega_0(z) + db$. With this, the equations can be reduced to

$$\begin{aligned}\partial_z b = &-\frac{8}{15}\frac{\gamma_0^r P_0}{T_0} f_R \int h_R(t) A_1\left(\frac{t}{T_0}\right)\mathrm{d}t + \frac{4}{3}\mu\gamma_1^r P_0\left[1-f_R+f_R\int h_R(t)B_1\left(\frac{t}{T_0}\right)\mathrm{d}t\right]\\ &-\frac{4}{3}\mu\gamma_0^i P_0 T_0 f_R\int h_R(t)A_2\left(\frac{t}{T_0}\right)\mathrm{d}t - \frac{4}{5}\frac{\gamma_1^i P_0}{T_0^2}\left[1-f_R+f_R\int h_R(t)B_2\left(\frac{t}{T_0}\right)\mathrm{d}t\right]\\ &-4\left(\frac{\pi^2}{9}-\frac{2}{3}\right)\mu^2\gamma_1^i P_0 T_0^2\left[1-f_R+f_R\int h_R(t)B_3\left(\frac{t}{T_0}\right)\mathrm{d}t\right]\end{aligned} \tag{3.3.15a}$$

$$\begin{aligned}\partial_z t_c = &\frac{1}{6}\beta_3\left[\pi^2\mu^2T_0^2+\frac{1}{T_0^2}\right]+\gamma_1^r P_0\left[1-f_R+f_R\int h_R(t)B_4\left(\frac{t}{T_0}\right)\mathrm{d}t\right]\\ &-\frac{2}{3}\gamma_0^i P_0 T_0 f_R\int h_R(t)A_2\left(\frac{t}{T_0}\right)\mathrm{d}t\\ &-2\left(\frac{\pi^2}{9}-\frac{2}{3}\right)\mu\gamma_1^i P_0 T_0^2\left[1-f_R+f_R\int h_R(t)B_3\left(\frac{t}{T_0}\right)\mathrm{d}t\right]\end{aligned} \tag{3.3.15b}$$

$$\begin{aligned}\partial_z T_0 = &\,2\mu T_0\beta_2+\frac{8}{\pi^2}\gamma_1^r P_0 f_R\int h_R(t)A_3\left(\frac{t}{T_0}\right)\mathrm{d}t\\ &+\frac{4}{\pi^2}\gamma_0^i P_0 T_0\left[1-f_R+f_R\int h_R(t)B_5\left(\frac{t}{T_0}\right)\mathrm{d}t\right]\\ &-\left(\frac{4}{3}-\frac{12}{\pi^2}\right)\mu\gamma_1^i P_0 T_0^2 f_R\int h_R(t)A_4\left(\frac{t}{T_0}\right)\mathrm{d}t\end{aligned} \tag{3.3.15c}$$

$$\begin{aligned}\partial_z P_0 = &-\alpha P_0 - 2\mu P_0\beta_2-\left(\frac{8}{\pi^2}+\frac{8}{15}\right)\frac{\gamma_1^r P_0^2}{T_0}f_R\int h_R(t)A_5\left(\frac{t}{T_0}\right)\mathrm{d}t\\ &-\left(\frac{4}{3}+\frac{4}{\pi^2}\right)\gamma_0^i P_0^2\left[1-f_R+f_R\int h_R(t)B_6\left(\frac{t}{T_0}\right)\mathrm{d}t\right]\\ &-\frac{12}{\pi^2}\mu\gamma_1^i P_0^2 T_0 f_R\int h_R(t)A_6\left(\frac{t}{T_0}\right)\mathrm{d}t\end{aligned} \tag{3.3.15d}$$

$$\begin{aligned}\partial_z\mu = &\,\beta_2\left(\frac{2}{\pi^2}\frac{1}{T_0^4}-2\mu^2\right)+\frac{2}{\pi^2}\frac{\gamma_0^r P_0}{T_0^2}\left[1-f_R+f_R\int h_R(t)B_7\left(\frac{t}{T_0}\right)\mathrm{d}t\right]\\ &-\left(\frac{8}{15}-\frac{4}{\pi^2}\right)\frac{\mu\gamma_1^r P_0}{T_0}f_R\int h_R(t)A_7\left(\frac{t}{T_0}\right)\mathrm{d}t-\frac{76}{15\pi^2}\frac{\gamma_1^i P_0}{T_0^3}f_R\int h_R(t)A_8\left(\frac{t}{T_0}\right)\mathrm{d}t.\end{aligned} \tag{3.3.15e}$$

The normalization of the $A_n(x)$ and $B_n(x)$ functions, is such that all integrals over B_n functions in Eq. (3.3.15) goes towards 1 as the pulse width is increased while integrals over A_n functions goes towards $T_R/(f_R T_0)$, where

$$T_R = f_R \int t\, h_R(t) \mathrm{d}t \tag{3.3.16}$$

Reducing the complete solution for broad pulses is thus straightforward, resulting in

$$\partial_z b = -\frac{8}{15}\frac{\gamma_0^r P_0 T_R}{T_0^2} + \frac{4}{3}\mu\gamma_1^r P_0 - \frac{4}{3}\mu\gamma_0^i P_0 T_R - \frac{4}{5}\frac{\gamma_1^i P_0}{T_0^2} - 4\left(\frac{\pi^2}{9} - \frac{2}{3}\right)\mu^2\gamma_1^i P_0 T_0^2, \tag{3.3.17a}$$

$$\partial_z t_c = \frac{1}{6}\beta_3\left[\pi^2\mu^2 T_0^2 + \frac{1}{T_0^2}\right] + \gamma_1^r P_0 - \frac{2}{3}\gamma_0^i P_0 T_R - 2\left(\frac{\pi^2}{9} - \frac{2}{3}\right)\mu\gamma_1^i P_0 T_0^2. \tag{3.3.17b}$$

$$\partial_z T_0 = 2\mu T_0 \beta_2 + \frac{8}{\pi^2}\frac{\gamma_1^r P_0 T_R}{T_0} + \frac{4}{\pi^2}\gamma_0^i P_0 T_0 - \left(\frac{4}{3} - \frac{12}{\pi^2}\right)\mu\gamma_1^i P_0 T_0 T_R, \tag{3.3.17c}$$

$$\partial_z P_0 = -\alpha P_0 - 2\mu P_0 \beta_2 - \left(\frac{8}{\pi^2} + \frac{8}{15}\right)\frac{\gamma_1^r P_0^2 T_R}{T_0^2} - \left(\frac{4}{3} + \frac{4}{\pi^2}\right)\gamma_0^i P_0^2 - \frac{12}{\pi^2}\mu\gamma_1^i P_0^2 T_R, \tag{3.3.17d}$$

$$\partial_z \mu = -2\mu^2\beta_2 + \frac{2}{\pi^2}\frac{\beta_2}{T_0^4} + \frac{2}{\pi^2}\frac{\gamma_0^r P_0}{T_0^2} - \left(\frac{8}{15} - \frac{4}{\pi^2}\right)\frac{\mu\gamma_1^r P_0 T_R}{T_0^2} - \frac{76}{15\pi^2}\frac{\gamma_1^i P_0 T_R}{T_0^4}. \tag{3.3.17e}$$

As can be seen from Eq. (3.3.15), the angular frequency shift is neither directly or indirectly dependent of the pulse shift in time, t_c, it is thus only necessary to model the four differential equations for b, P_0, T_0 and μ.

3.3.1 Comparison of Models

A SSFS model based on the same approach has previously been proposed by Chen *et. al.* [62] though not including the imaginary part of the nonlinear constant, i.e. TPA. It is thus appropriate to compare the model proposed here with the model of Chen *et. al.* as well as with simulations of the GNLS equation. The model of Chen *et. al.* does not account for any nonlinear loss, so in the comparison, $\gamma_n^i = 0$ in order to properly compare the two models. The simulation of the GNLS is performed with the interaction-picture method described by Travers *et. al.* [69].

For comparison, a fundamental soliton input at 1550 nm is considered, in a 50 m silica fiber with a loss of 0.2 dB/km. The dispersion parameters are assumed as $\beta_2 = -5.1$ ps^2/km and $\beta_3 = 0.1$ ps^3/km. The nonlinear constants are assumed to be $\gamma_0^r = 2$ W^{-1}km^{-1} and $\gamma_1 = \gamma_0^r/\omega_0$. The input peak power is defined by the chosen pulse width, according to the relation $P_0 = |\beta_2|/(\gamma_0^r T_0^2)$, as a fundamental soliton is assumed. For the Raman response function, the data shown in Fig. 3.3 has been used.

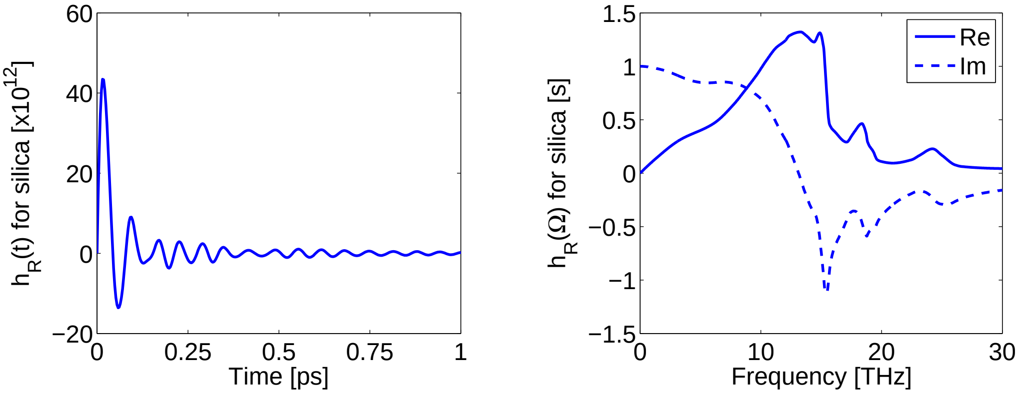

Figure 3.3: The Raman response function for silica in time (left) and frequency (right).

Fig. 3.4 shows the SSFS results for both a 100 fs and a 25 fs broad pulse. The broader pulse shows a good level of agreement between the two MoM models and the simulation in both frequency shift and evolution of the peak power and pulse width. The 25 fs pulse is showing good agreement in frequency shift although the two models predict the evolution of the peak power and pulse width with bigger variation then the numerical simulations. When the pulse width is reduced to 10 fs, as is shown in Fig. 3.5, the two MoM models begin to break down. This breakdown is due to the increased effect of higher order effects, such as TOD and self-steepening, and the chosen ansatz not being able to accommodate these, as the ansatz is based on a fundamental soliton. A more complex ansatz would be possible, but any added complexity would lead entail more parameters to account for in the model, thus also greatly increasing the computational time.

Figs. 3.4 and 3.5 also show, that with decreased pulse width, a greater difference between the two MoM models starts to show, thus indicating a difference in the two analytical models. In the paper of Chen *et. al.* the pulse energy, E, and a

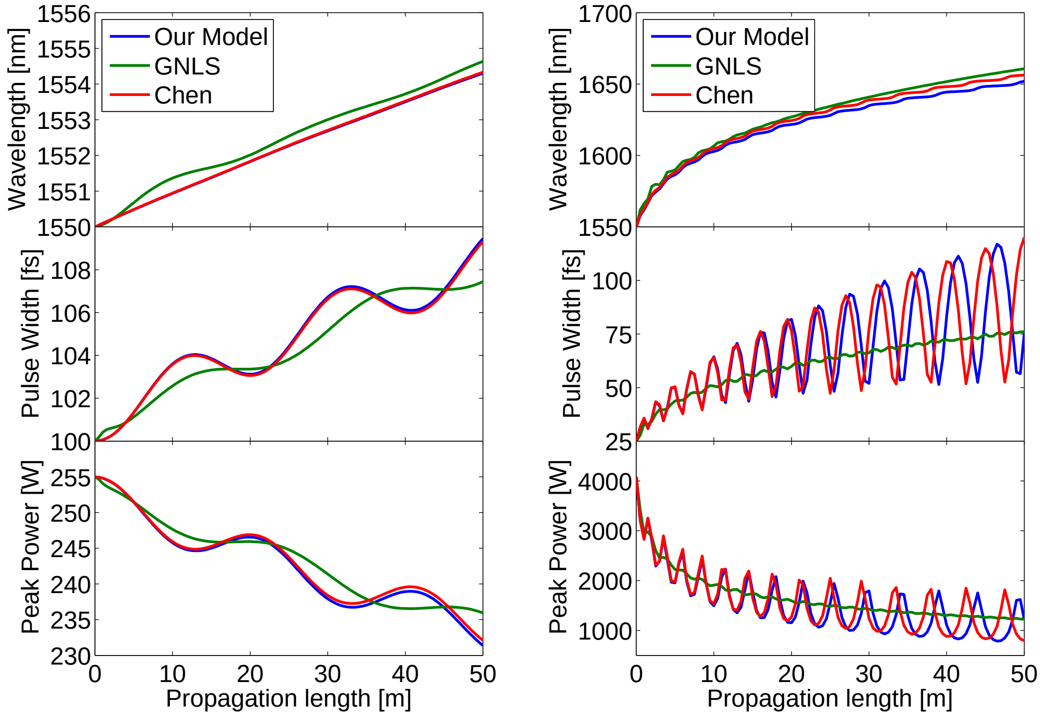

Figure 3.4: Center wavelength (top), pulse width (middle) and peak power (bottom) as a function of propagation distance for a pulse with initial width of 100 fs (left) and 25 fs (right). It shows that there is generally a good agreement between the analytical models and the result from the simulations of the GNLS equation.

normalized quadratic chirp, C, is used instead of peak power and quadratic chirp,

$$E = \frac{2P_0}{T_0}, \tag{3.3.18a}$$

$$C = \frac{\mu}{2T_0^2}. \tag{3.3.18b}$$

With this redefinition, and also neglecting any nonlinear loss, meaning that $\gamma_n^i = 0$, in order to compare the models, as Chen *et. al.* does not account for this, the

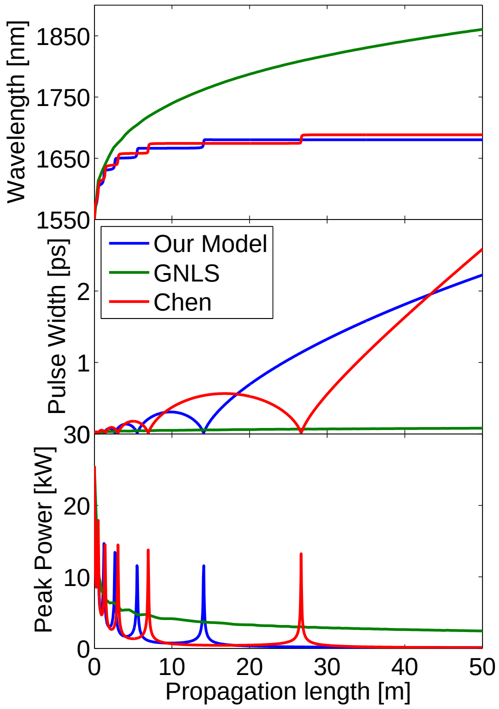

Figure 3.5: Center wavelength (top), pulse width (middle) and peak power (bottom) as a function of propagation distance for a pulse with initial width of 10 fs. In this case there is a bigger discrepancy between the MoM models and the simulation of the GNLS equation.

differential equations can be expressed as

$$\partial_z b = -\frac{4}{15}\frac{(\gamma_0^r + b\gamma_1^r)E}{T_0^2} f_R \int h_R(t) A_1\left(\frac{t}{T_0}\right) \mathrm{d}t \\ + \frac{1}{3}\frac{\gamma_1^r EC}{T_0^3}\left[1 - f_R + f_R \int h_R(t) B_1\left(\frac{t}{T_0}\right) \mathrm{d}t\right], \tag{3.3.19a}$$

$$\partial_z t_c = b(\beta_2 + b\beta_3) + \frac{1}{2}\beta_3\left[\frac{\pi^2}{12}\frac{C^2}{T_0^2} + \frac{1}{3T_0^2} - b^2\right] \\ + \frac{1}{2}\frac{\gamma_1^r E}{T_0}\left[1 - f_R + f_R \int h_R(t) B_4\left(\frac{t}{T_0}\right) \mathrm{d}t\right], \tag{3.3.19b}$$

$$\partial_z T_0 = \frac{(\beta_2 + b\beta_3)C}{T_0} + \frac{4}{\pi^2}\frac{\gamma_1^r E}{T_0} f_R \int h_R(t) A_3\left(\frac{t}{T_0}\right) \mathrm{d}t, \tag{3.3.19c}$$

$$\partial_z E = -\alpha E - \frac{4}{15}\frac{\gamma_1^r E^2}{T_0^2} f_R \int h_R(t) A_1\left(\frac{t}{T_0}\right) \mathrm{d}t, \tag{3.3.19d}$$

$$\partial_z C = \left(C^2 + \frac{4}{\pi^2}\right)\frac{(\beta_2 + b\beta_3)}{T_0^2} + \frac{2}{\pi^2}\frac{(\gamma_0^r + b\gamma_1^r)E}{T_0}\left[1 - f_R + f_R \int h_R(t) B_7\left(\frac{t}{T_0}\right) \mathrm{d}t\right] \\ + \frac{150 - 4\pi^2}{15\pi^2}\frac{\gamma_1^r EC}{T_0^2} f_R \int h_R(t) A_9\left(\frac{t}{T_0}\right) \mathrm{d}t, \tag{3.3.19e}$$

where we have used Eq. (3.3.14a) and have introduced

$$A_9(x) = \frac{1}{150 - 4\pi^2}\left[120A_3(x) - \left(4\pi^2 - 30\right)A_7(x)\right], \tag{3.3.20}$$

in order to ease the comparison. By direct comparison, it shows that a completely agreement with Chen *et. al.* would require that

$$A_3(x) = A_9(x) = A_1(x) = \frac{15}{8}\mathrm{csch}^4(x)\left[4x + 2x\cosh(2x) - 3\sinh(2x)\right], \tag{3.3.21}$$

and that

$$\int h_R(t)B_1\left(\frac{t}{T_0}\right)\mathrm{d}t = \int h_R(t)B_4\left(\frac{t}{T_0}\right)\mathrm{d}t = 1. \tag{3.3.22}$$

After careful scrutiny, no mistakes were found in this work, so the origin of the difference between the two models remains uncertain. This difference between the models is reduced as the pulse width is increased, as the A_n and B_n functions can be reduced, which reduces this model to that presented by Chen *et. al.* Fig. 3.6 shows the value of these functions while Fig. 3.7 shows the value of the integral over these functions. It shows that while the A_n functions differ, the integral value display approximately the same value, whereas the integral over the B_n functions shows a significant difference, leading to the different outcomes of the two MoM models.

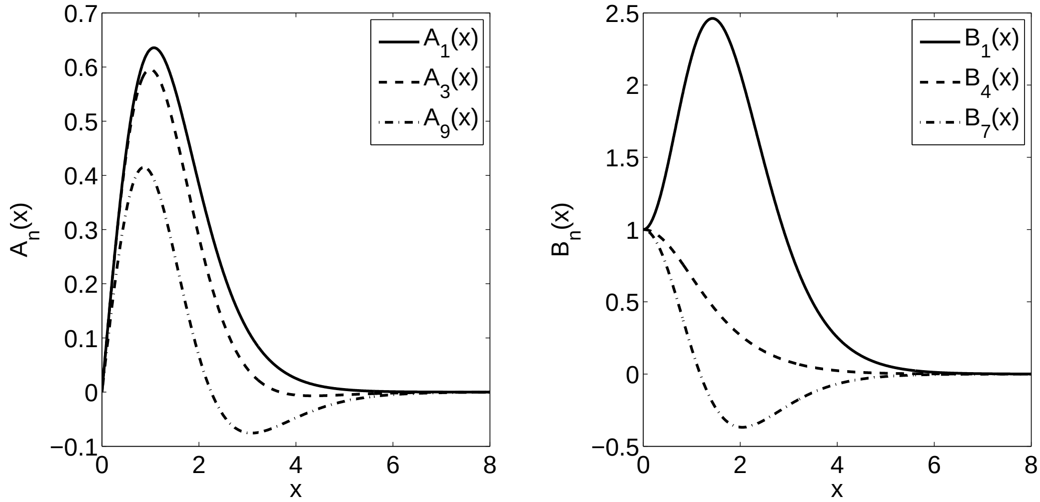

Figure 3.6: A_n (left) and B_n (right) functions used in Eq. (3.3.19).

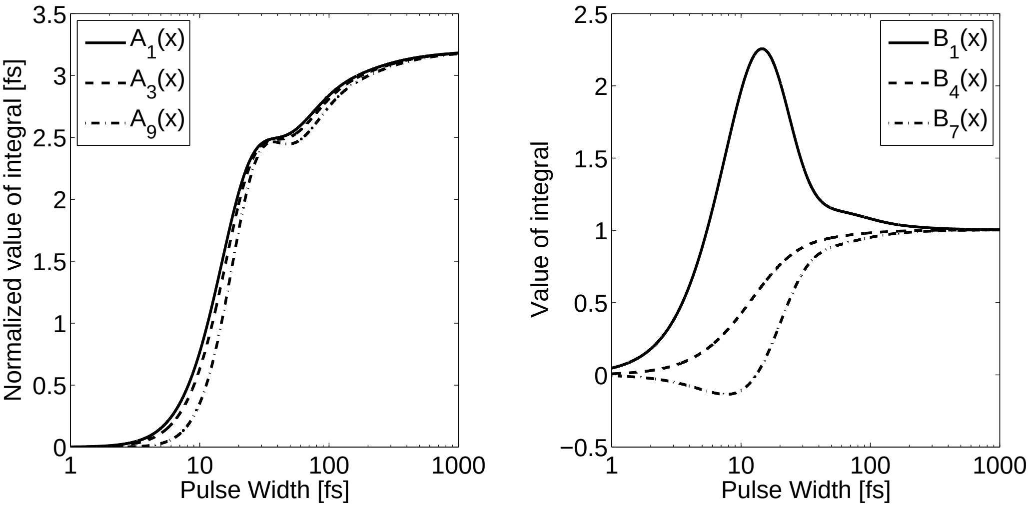

Figure 3.7: Value of $\int h_R(t)f(t/T_0)\mathrm{d}t$ for A_n (left) and B_n (right) functions used in Eq. (3.3.19) in the case of a silica Raman response. For A_n functions, the integral value has been normalized with $f_R T_0$.

3.4 Effect of Two-Photon Absorption

As TPA is a power reducing effect and the Raman effect is dependent on power, it is expected that the nonlinear loss will lead to a decrease in red-shift. If a wide chirp free pulse is considered, then Eq. (3.3.17) reduces to

$$\partial_z P_0 = -\alpha P_0 - \left(\frac{4}{3} + \frac{4}{\pi^2}\right)\gamma_0^i P_0^2. \tag{3.4.1a}$$

$$\partial_z T_0 = \frac{8}{\pi^2}\frac{\gamma_1^r P_0 T_R}{T_0} + \frac{4}{\pi^2}\gamma_0^i P_0 T_0 \tag{3.4.1b}$$

$$\partial_z b = -\frac{8}{15}\frac{\gamma_0^r P_0 T_R}{T_0^2} \tag{3.4.1c}$$

where also the dispersion of TPA has been neglected. These reduced differential equations offer an insight into the effect of TPA and make it possible to give some qualitative predictions of the influence of the nonlinear loss. As seen from the 2nd term of the Right Hand Side (RHS) side of Eq. (3.4.1a), the peak power is reduced due to the TPA while simultaneously, as seen from the 2nd term on the RHS of Eq. (3.4.1b), the pulse width is initially increased. As the rate of red-shift is proportional to the peak power and inversely proportional to the pulse width squared, it's seen that at least initially, and while the pulse is still chirp free, the rate of red-shift is decreased.

The approximation to the peak power, Eq. (3.4.1a), is analytically solvable and is used to define a nonlinear loss length, including both linear and TPA loss, as the length after which the peak power has been reduced to $1/e$ of the initial value, given by

$$L_{\text{loss}} = \frac{1}{\alpha}\ln\left[\frac{e + \left(\frac{4}{3} + \frac{4}{\pi^2}\right)\frac{\gamma_0^i P_0(0)}{\alpha}}{1 + \left(\frac{4}{3} + \frac{4}{\pi^2}\right)\frac{\gamma_0^i P_0(0)}{\alpha}}\right]. \tag{3.4.2}$$

This nonlinear loss length gives us a qualitative expression for the length after which the peak power is reduced to the extend where the red-shifting of the soliton is effectively halted. For a case where TPA can be neglected, it is seen that the loss length is reduced to only depend on the linear loss. In Fig. 3.8 is shown the results

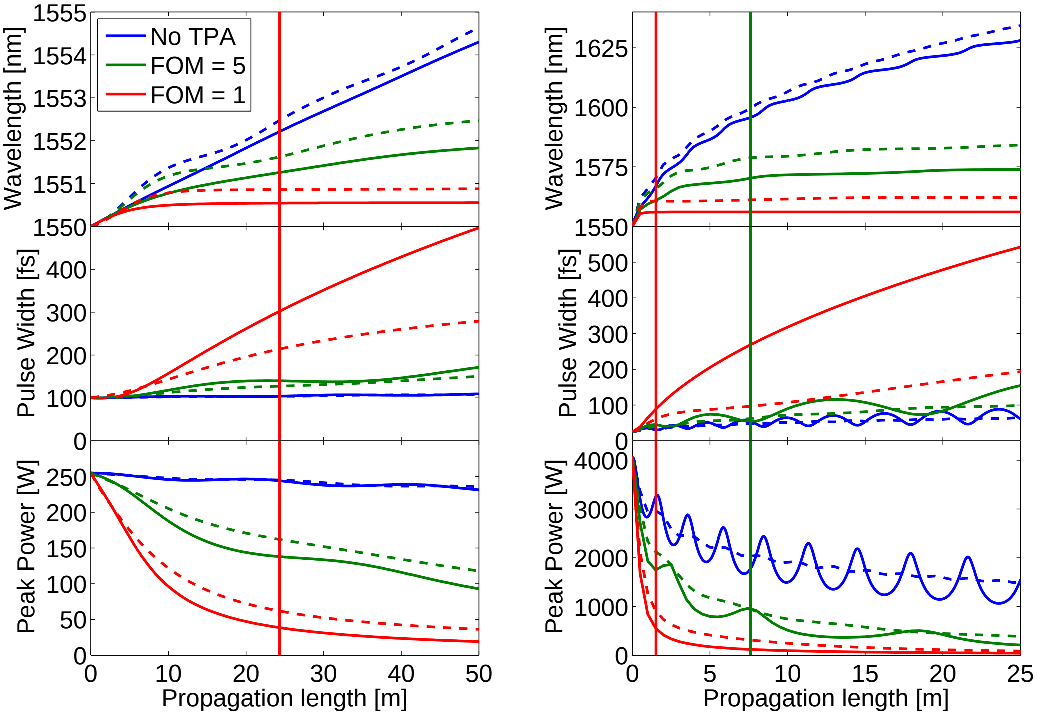

Figure 3.8: Center wavelength (top), pulse width (middle) and peak power (bottom) as a function of propagation distance for a pulse with initial width of 100 fs (left) and 25 fs (right). The results from the proposed model (solid) and numerical simulations (dashed) are shown for different levels of TPA.

for a scenario, where the material properties from the silica fiber used in Sec. 3.3.1 and a non-zero TPA coefficient is assumed. Although this is unphysical, it is useful to show the effect of including TPA and to compare the model with numerical simulations. The TPA coefficient is given in the form of a Figure of Merit (FOM), defined as

$$\text{FOM} = \frac{n_2}{\lambda\beta_{\text{TPA}}} = \frac{\gamma_0^r}{4\pi\gamma_0^i}, \tag{3.4.3}$$

and thus the lower the FOM, the greater the nonlinear loss. The results shows that there is a good qualitative agreement between the proposed model and the simulations. Both the red-shift and peak power shows the same characteristics, with the predictions of the pulse width being slightly more varied, however a significant difference does not occur until the power is greatly reduced and the red-shift already shows to have effectively halted. In all cases this also shows to happen before the define nonlinear loss length. Furthermore it shows that, as predicted, the greater the TPA, the lower the accumulated red-shift. The nonlinear loss length, L_{loss}, has been plotted as vertical lines in each case, and it shows as a good measure of the distance after which the red-shift has effectively halted. At the distance, L_{loss}, the simulations and the model show that the peak power has decreased more than to the $1/e$ value, which is due to the way the term has been derived where pulse broadening, which also cause a decrease in peak power, was neglected.

3.4.1 Red-Shift in Chalcogenide

Some soft glasses, like the chalcogenide materials arsenic selenide, As_2Se_3, and arsenic sulfide, As_2S_3, have substantial two photon absorption coinciding with the wavelengths used in telecommunication, which can limit the performance of these materials. Table 3.2 lists measured values of the nonlinear parameters for arsenic selenide found in the literature. In Yeom *et. al.* [43], a chalcogenide fiber was tapered in order to decrease the ZDW below 1550 nm, enabling the possibility to pump the fiber in the anomalous dispersion regime with an erbium fiber laser to create a mid-infrared supercontinuum. The obtained dispersion and effective area are found to be $\beta_2 = -360$ ps^2/km, $\beta_3 = 3.85$ ps^3/km and $A_{\text{eff}} = 0.4773$ μm^2. The nonlinear coefficients are calculated from the values in Table 3.2 with the assumption that the effective area is independent of frequency in order to differentiate $\gamma_0(\omega)$. Finally

Table 3.2: Used values of the nonlinearity and two photon absorption for a As_2Se_3 Chalcogenide fiber by Nguyen *et. al.* [22].

λ (nm)	n_2 (10^{-18}m^2/W)	β_{TPA} (10^{-11}m/W)	FOM
1415	11.0†	0.97	0.8†
1434	14.0†	1.10	0.9†
1456	13.0†	0.80†	1.1†
1491	9.9†	0.46†	1.45†
1515	8.9†	0.31	1.9†
1554	7.0†	0.25	1.8†

($\dagger$) marks values read off from a figure.

the Raman response function, $h_R(t)$, is based on Hu *et. al.* [29], where, by fitting to the estimated gain peak position and Full Width Half Maximum (FWHM), the response has been approximated with a decaying harmonic oscillator as given by

$$h_R(t) = \frac{\tau_1^2 + \tau_2^2}{\tau_1 \tau_2^2} \exp\left(-\frac{t}{\tau_2}\right) \sin\left(\frac{t}{\tau_1}\right), \tag{3.4.4}$$

with $\tau_1 = 23$ fs, $\tau_2 = 210$ fs and using the reported fraction of the Raman response, $f_R = 0.1$. The comparison to that of silica is shown in Fig. 3.9. The resulting nonlinear constant for the chalcogenide tapered fiber is 62.4 $\mathrm{W}^{-1}\mathrm{m}^{-1}$, 4 orders of magnitude higher than that of a typical silica fiber as used in Sec. 3.3.1.

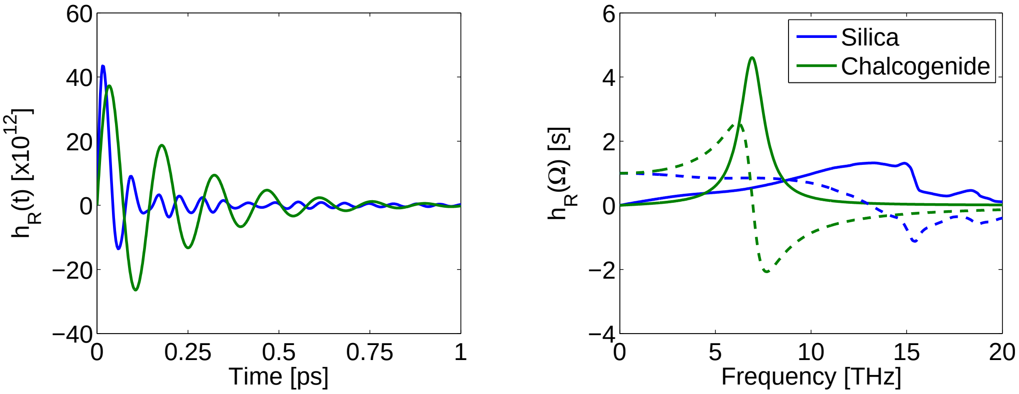

Figure 3.9: Comparison of the Raman response function of silica and $\mathrm{As_2Se_3}$.

The difference in including TPA in modelling SSFS is seen in Fig. 3.10, where the evolution of a fundamental soliton is shown for a pulses with a width of 50 fs and 25 fs, respectively. For both pulses it shows that the TPA greatly reduce the expected red-shift due to a combined decrease in peak power and increase in pulse width.

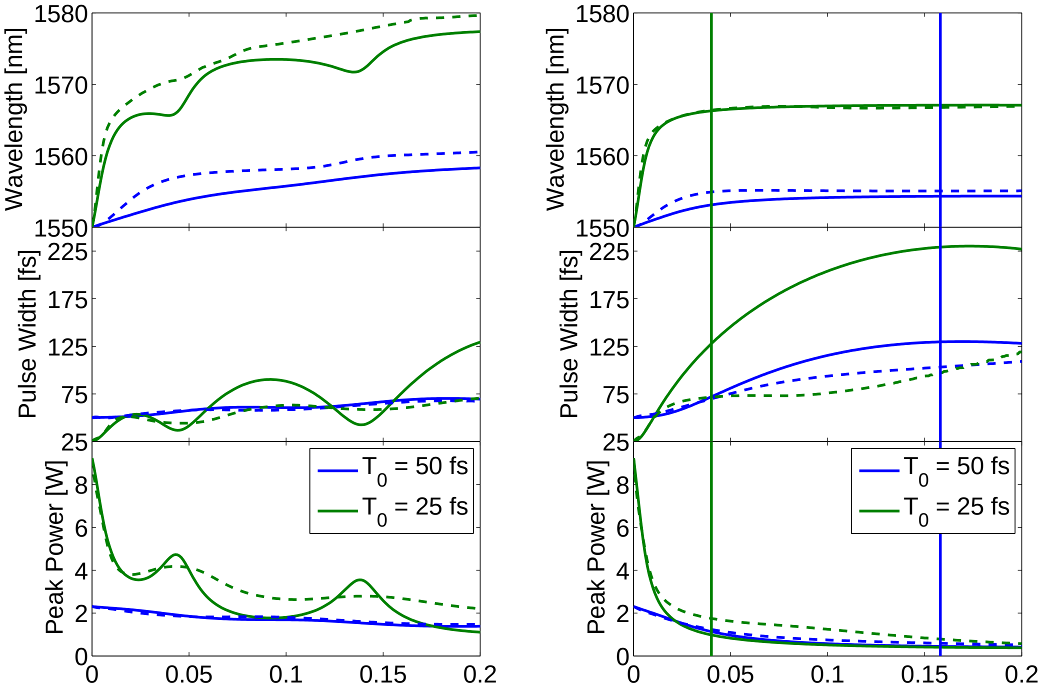

Figure 3.10: Center wavelength (top), pulse width (middle) and peak power (bottom) as a function of propagation distance for a pulse with initial width of 50 fs propagated where TPA is neglected (left) and included (right). Comparison between the proposed model (solid) and numerical simulations (dashed) is also shown with the nonlinear loss length shown as the vertical lines.

4

Terahertz

THz technologies have gotten increased interest in recent years with the ability to use THz pulses for spectroscopy of a wide range of physical, chemical and biological samples [70, 4]. There has been a great focus on developing methods for THz radiation and detection [8, 71], which has enabled the field to expand. With the ability to create and detect THz has come an interest in creating THz devices to expand the field, with such examples as waveguides [72, 73], filters [74, 75] and modulators [76, 77]. It is in this light that new materials are investigated to show if they have potential as basis for optical devices. Soft glasses is known to display good transmission properties in the mid-infrared, and they are thus of interest as well as they might have transmission bands reaching out to the THz regime.

This chapter begins with an explanation of THz Time Domain Spectroscopy (THz-TDS) and the theory behind how it is used to determine the complex refractive index. The different experimental techniques used to perform the measurements is then discussed after which the resulting data is presented. First with an in-depth analysis of a single sample to outline the method of retrieving the index, then the resulting index for all the samples are discussed. Finally an attempt at performing Time Resolved THz Spectroscopy (TRTS) is outlined and discussed with the chapter ending with a discussion on the next step in investigating these materials.

4.1 THz Time Domain Spectroscopy

With the ability of measuring the electric field of a THz pulse, and not just the intensity of the field, it is possible to perform THz-TDS which can be used to measure the complex refractive index of materials [4, 78].

4.1.1 Measuring The Complex Refractive Index

If we assume a plane wave incident perpendicular on a surface, the transmission, T, and reflection, Γ, coefficients for an electric field traveling from region 1 with index $\tilde{n}_1$ perpendicular on region 2 with index $\tilde{n}_2$ are

$$T_{1-2} = \frac{2\tilde{n}_2}{\tilde{n}_2 + \tilde{n}_1}, \tag{4.1.1a}$$

$$\Gamma_{1-2} = \frac{\tilde{n}_2 - \tilde{n}_1}{\tilde{n}_2 + \tilde{n}_1}, \tag{4.1.1b}$$

where the complex refractive index is given as

$$\tilde{n} = n + \mathrm{i}\kappa \tag{4.1.2}$$

with κ representing the linear loss as $\alpha = 2\omega\kappa/c$. By comparing a measured electric field where a sample is present in the beam path to a reference measurement where there is no sample, it is possible for us to determine the transfer function and thus use this to determine the index. There is two possibilities to perform this measurement, either by measuring the transmitted field from a sample or the reflected field.

In Transmission

In transmission the sample is placed at the focus of the beam path. The electric field is measured, E_{sample}, as well as the electric field when the sample is not present to use as the reference electric field, E_{ref}. E_{sample} will consist of the first part of the pulse propagated straight through the sample as well as the transmitted echoes of the remainder of the pulse that have been bouncing back and forth inside the sample. This can be expressed as

$$\begin{aligned}\tilde{E}_{sample}(\omega) = &T_{s-a} \left[e^{\mathrm{i}k_0(\tilde{n}_s-\tilde{n}_a)d} + \Gamma_{s-a}^2 e^{\mathrm{i}k_0(\tilde{n}_s-\tilde{n}_a)(3d)}\right.\\ &\left. + \Gamma_{s-a}^4 e^{\mathrm{i}k_0(\tilde{n}_s-\tilde{n}_a)(5d)} + \Gamma_{s-a}^6 e^{\mathrm{i}k_0(\tilde{n}_s-\tilde{n}_a)(7d)} + \ldots\right] T_{a-s}\tilde{E}_{ref}(\omega),\end{aligned} \tag{4.1.3}$$

where the subscripts s and a refers to sample and air, respectively. The first term in the sum is the pulse propagating straight through the sample, with thickness d. The exponential term expresses the phase change that the field experience from traveling through the sample instead of the air, where k_0 is the vacuum propagation constant. Second term in the sum is the transmission of the first echo. This echo have been reflected inside the sample twice and traveled a total distance of $3d$, the remaining terms follow from the same method, and thus

$$\begin{aligned}\tilde{T}(\omega) =&\frac{\tilde{E}_{sample}(\omega)}{\tilde{E}_{ref}(\omega)}\\ =&T_{s-a}T_{a-s}e^{ik_0(\tilde{n}_s-\tilde{n}_a)d}\sum_{m=0}^{\infty}\left[\Gamma_{s-a}^2 e^{i2k_0(\tilde{n}_s-\tilde{n}_a)d}\right]^m\\ =&T_{s-a}T_{a-s}e^{\mathrm{i}k_0(\tilde{n}_s-\tilde{n}_a)d}\frac{1}{1-\Gamma_{s-a}^2 e^{\mathrm{i}2k_0(\tilde{n}_s-\tilde{n}_a)d}}.\end{aligned} \tag{4.1.4}$$

This expression for the transmission assumes an infinite sampling length in time, or as an approximation all measurable echoes above the noise. However, if the sample is thick, it is possible to distinguish the echoes in time, and thus the total transmission can be approximated as

$$\begin{aligned}\tilde{T}(\omega) =&T_{s-a}T_{a-s}e^{\mathrm{i}k_0(\tilde{n}_s-\tilde{n}_a)d}\\ =&\frac{4\tilde{n}_s}{\tilde{n}_s+1}e^{\mathrm{i}k_0(\tilde{n}_s-1)d}.\end{aligned} \tag{4.1.5}$$

This expression has to be numerically solved, which is best done by separating the problem into two coupled real equations, thus with the total transmission coefficient being defined as $\tilde{T}(\omega) = |\tilde{T}(\omega)|\exp\left[\mathrm{i}\Phi_T(\omega)\right]$, we have

$$|\tilde{T}(\omega)| = \frac{4\sqrt{n^2+\kappa^2}}{(n+1)^2+\kappa^2}e^{-\frac{\omega}{c}\kappa d} \tag{4.1.6a}$$

$$\Phi_T(\omega) = \frac{\omega}{c}(n-1)d - \tan^{-1}\left(\frac{\kappa\left(n^2+\kappa^2-1\right)}{n(n+1)^2+\kappa^2(n+2)}\right), \tag{4.1.6b}$$

which can be readily solved with numerical tools such as Matlab. If the absorption of the material is small, such that $\kappa \ll n$, the transmission coefficients from air to sample and again from sample to air can be regarded as real, decoupling the two equations and instead result in [4]

$$|\tilde{T}(\omega)| = \frac{4n}{(n+1)^2}e^{-\frac{\omega}{c}\kappa d} \tag{4.1.7a}$$

$$\Phi_T(\omega) = \frac{\omega}{c}(n-1)d, \tag{4.1.7b}$$

or

$$n = 1+\frac{c}{\omega d}\Phi_T(\omega) \tag{4.1.8a}$$

$$\kappa = -\frac{1}{k_0 d}\ln\left[\frac{(n+1)^2}{4n}|\tilde{T}(\omega)|\right]. \tag{4.1.8b}$$

In deriving this, it was assumed that the electric field could be assumed as a plane wave. If instead the electric field is propagating as a Gaussian beam, then it is also necessary to account for the Gouy phase shift [79]. This phase shift is $-\pi/2$ at an infinite negative propagation distance from the beam waist to $\pi/2$ at an infinite positive propagation distance. Thus the measured phase shift should potentially be adjusted with up to π depending on the beam properties. It was shown, that the index retrieved with the plane wave approximation would have a negative correction when accounting for the Gouy phase shift [79], however, as the beam profile of this experiment is not characterized, the plane wave approximation is assumed.

The complication with performing a transmission measurement occurs when the sample does not transmit light in the entire frequency region. In this case, it makes it impossible to determine the accurate phase of any light with a frequency above the black region, thus making it difficult to evaluate the refractive index.

In Reflection

If the reflected field is measured instead, the reference electric field is the reflected field off a known sample. The known sample should always be a metal, as in this case, the reflection coefficient is 1, meaning that the measured reference electric field is the field that will be incident on the sample. As with the transmitted field, the reflected field also have contributions from the echoes in the sample, thus the total reflection coefficient can be expressed as

$$\begin{aligned}
\tilde{\Gamma}(\omega) =& \frac{\tilde{E}_{sample}(\omega)}{\tilde{E}_{ref}(\omega)} \\
=& \Gamma_{a-s} + T_{s-a}\left[\Gamma_{s-a}e^{ik_0(\tilde{n}_s-\tilde{n}_a)(2d)} + \Gamma_{s-a}^3 e^{ik_0(\tilde{n}_s-\tilde{n}_a)(4d)}\right. \\
&\qquad \left. + \Gamma_{s-a}^5 e^{ik_0(\tilde{n}_s-\tilde{n}_a)(6d)} + \Gamma_{s-a}^7 e^{ik_0(\tilde{n}_s-\tilde{n}_a)(8d)} + \ldots\right] T_{a-s} \\
=& \Gamma_{a-s} + T_{s-a}T_{a-s}\Gamma_{s-a}e^{i2k_0(\tilde{n}_s-\tilde{n}_a)d}\sum_{m=0}^{\infty}\left[\Gamma_{s-a}^2 e^{i2k_0(\tilde{n}_s-\tilde{n}_a)d}\right]^m \\
=& \Gamma_{a-s} + \frac{T_{s-a}T_{a-s}\Gamma_{s-a}e^{i2k_0(\tilde{n}_s-\tilde{n}_a)d}}{1-\Gamma_{s-a}^2 e^{i2k_0(\tilde{n}_s-\tilde{n}_a)d}}. \qquad (4.1.9)
\end{aligned}$$

As with a transmission measurement, if the sample is sufficiently thick or lossy, the echoes can be ignored and the total reflection can be assumed to be just the initial reflection. This results in a analytically solvable equation, given the complex refractive index as

$$\tilde{n} = \frac{1+\tilde{\Gamma}}{1-\tilde{\Gamma}}. \qquad (4.1.10)$$

A complication in using the reflection method to measure the refractive index, is that if the metal mirror used as a reference is not positioned exactly where the surface of the sample will be, there will be a phase change due to the different path length of the beam. If Δx represent the distance the metal mirror is position ahead of the sample in the beam path, then $\tilde{\Gamma}(\omega)$ has to be multiplied with a $\exp\left(i2\frac{w}{c}\Delta x\right)$ phase change. This phase change will have to be assessed by looking at the initially measured phase of the reflection, and then trying to determine the size of the displacement Δx.

In Fig. 4.1 is shown the theoretical phase of Γ as a function of κ for various values of n. As it shows, the phase of Γ will never be negative and for an index greater than 2, it is bounded at roughly 0.5 rad.

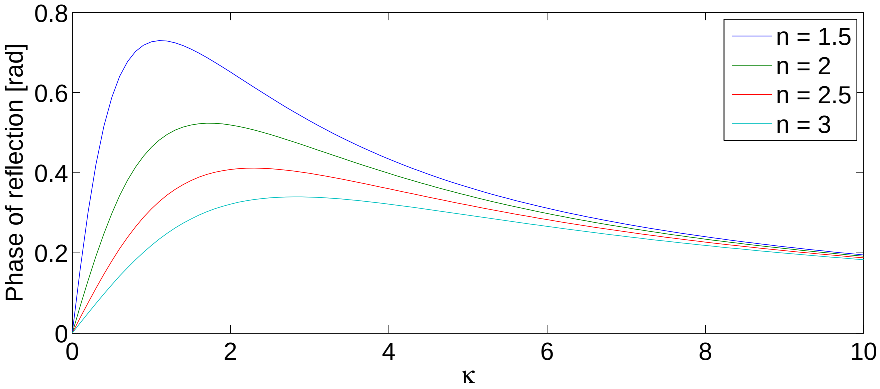

Figure 4.1: The phase of Γ as a function of κ for various values of n.

4.1.2 Measuring the Refractive Index of Thick Samples

As it is difficult to accurately estimate the corrective phase change in a reflection measurement, a transmission measurement is often preferred. However as mentioned if the sample have a black region, i.e. no light is transmitted, it is not possible to determine the phase of the light for any frequencies above this region, nor is it of course possible to determine the index in the black region itself. Thus for thick samples, a reflection measurement has to be performed in order to have the possibility of determining the refractive index for the entire frequency region. However, as there is usually an unknown phase change to account for in the reflection measurement, the transmission spectrum can be used as a reference when trying to determine this phase change.

4.1.3 Experimental Setups

There electric field was measured in two different experimental setups. At low frequencies, a commercial system called Picometrix was used [80], while for higher frequencies, a broadband Air Based Coherent Detection (ABCD) setup was used.

The principles behind these two THz systems are explained in the below. Other options for creating THz radiation also include using a $\chi^{(2)}$ nonlinear crystal for optical rectification. Two nonlinear crystals commonly used for this process are ZnTe [81] or $LiNbO_3$ [8]. The principle behind using a nonlinear crystal, specifically $LiNbO_3$ are briefly outlined in Sec. 4.4.

Finally for additional comparison, the samples were also tested with Fourier Transform Infra Red (FTIR) spectroscopy, which does not allow for index determination, but will further validate the results obtained with the Picometrix and ABCD experiments.

Picometrix

The commercial time-domiain system used is from commercial supplier Picometrix with the product name "T-Ray 4000® TD-THz System" [80]. The system has a 0.02 - 2 THz bandwidth with a high Signal-to-Noise Ratio (SNR) of above 70 dB. As this system is from a commercial supplier, the specific generation and detection scheme is not divulged, however, comparable systems make use of the exciting a photoconductive switch by a femtosecond (fs) pulse for THz generation and use a similar photoconductive switch as an antenna and have it sampled by the same fs pulse train for detection of the field [4].

The principle behind using a photoconductive switch to generate THz radiation is based on the oscillation of an electric dipole. In time domain, the electric field generated by an oscillating dipole moment can be expressed as [4]

$$E(r,\theta,t) = \frac{1}{4\pi\varepsilon_0}\left[\frac{1}{r^3}\mathbf{p}\left(t-\frac{r}{c}\right) + \frac{1}{cr^2}\partial_t\mathbf{p}\left(t-\frac{r}{c}\right)\frac{1}{c^2r}\partial_t^2\mathbf{p}\left(t-\frac{r}{c}\right)\right]\sin\left(\theta\right), \tag{4.1.11}$$

where r and θ is the distance and angle, respectively, from the dipole moment $\mathbf{p}$. In the far field region, where $r \gg \lambda \gg d$ and d is the size of the dipole, only the last term on the RHS is significant, and thus the electric field is only dependent on the second derivative of the dipole moment or the first derivative of the current density $j(t)$. Biasing two electrodes on a semiconductor layer, and then impinge a fs pulse onto the biased semiconductor surface, will excite electrons in the semiconductor and create a current between the two electrodes creating the THz radiation. For detection, a similar structure can be used as an antenna, though with the bias being provided by a portion of the fs pulse train used to generate the THz field. The fs pulse gates the antenna and the THz field then drives a current over the antenna which will be proportional to the THz electric field strength.

ABCD Setup

The ABCD setup is named after the ABCD scheme used to detect the THz pulse [71]. The characteristics of this setup is the ability to create a broadband THz pulse, ranging from about 2 to about 18 THz, a schematic of the setup can be seen in Fig. 4.2.

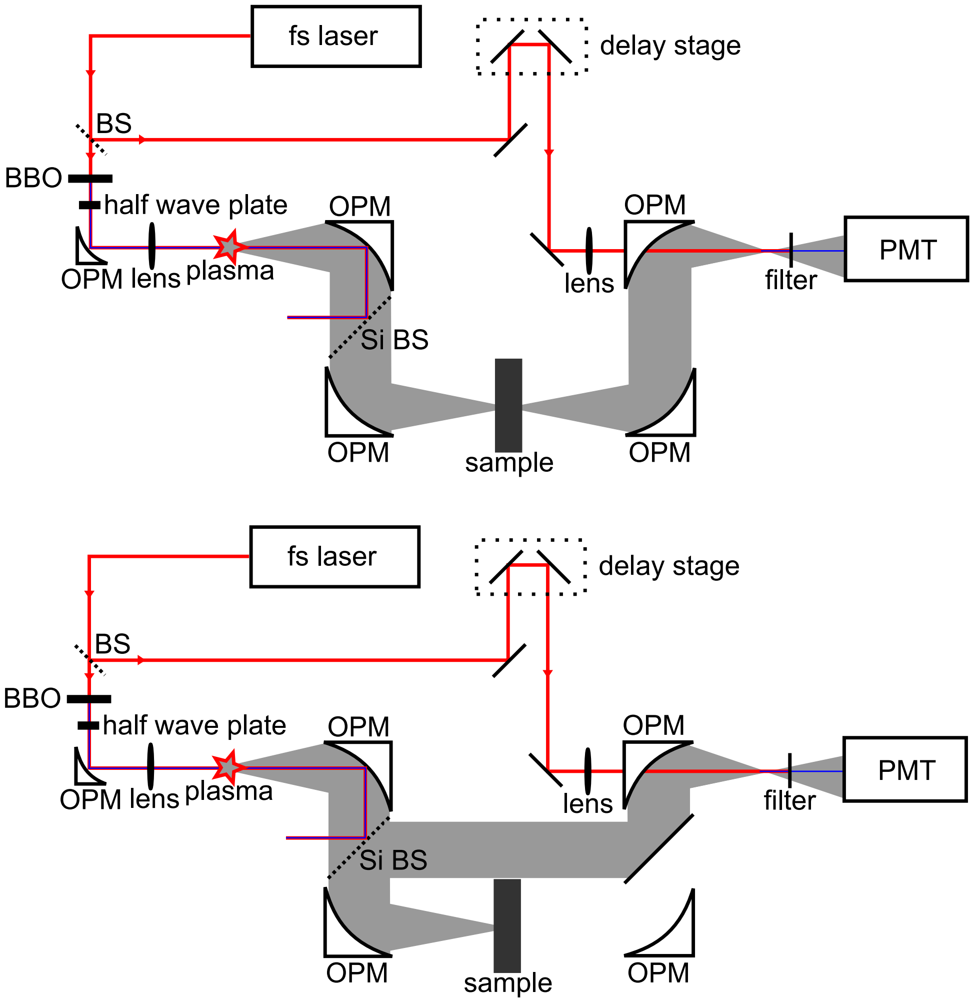

Figure 4.2: Setup of the ABCD experiment for both transmission (top) and reflection (bottom). PMT: Photo Multiplying Tube, BS: Beam Splitter, OPM: Off-axis Parabolic Mirror.

The setup is powered by a Ti:sapphire regenerative amplifier (Spectra-Physics Spitfire) emitting 1.5mW, 35fs laser pulses with a central wavelength of 800nm at a rate of 1kHz. The pulse train is split in two, one for THz generation, the other half for THz detection. The beam for THz generation is propagated through a β-Barium Borate (β-BBO) crystal, creating 400nm pulses in a Type 1 Second Harmonic Generation (SHG) process. The half wave plate is used to collinearize the 400 and 800nm light before being focused into an air plasma by an off-axis paraboloidal mirror. The air plasma is created inside a N_2 purged chamber, to reduce the level of water in the sample chamber. The THz pulse is generated in the air plasma through a Four Wave Mixing (FWM) rectification process that makes use of the spectral broadening of the pulses [82, 83]. The third order polarization created by in air plasma is

$$P^{(3)}(t) = \chi^3_{xxxx} E_{800nm}(t) E_{800nm}(t) E_{400nm}(t), \tag{4.1.12}$$

from which the THz wave is formed as, in the far field,

$$E_{THz}(t) \propto \partial_t^2 P^{(3)}(t). \tag{4.1.13}$$

The detection of the pulse is based on the before mentioned ABCD scheme. The THz pulse is focused in air with an AC bias and a detection pulse. The THz pulse enables a frequency doubling of the detection pulse in a third order nonlinear process,

$$E^{THz}_{400nm} \propto \chi^{(3)}_{xxxx} I_{800nm} E_{THz}, \tag{4.1.14}$$

thus the frequency doubled field is proportional to the THz field, however, if measured without the Ac bias, the phase information of the THz field would be lost, as $I_{measured} = I^{THz}_{400nm} \propto (\chi^{(3)}_{xxxx} I_{800nm})^2 I_{THz}$. The AC bias also stimulates frequency doubling of the detection pulse similar to the THz pulse does. Thus the electric field created is

$$E_{400nm} \propto \chi^{(3)}_{xxxx} I_{800nm} E_{THz} + \chi^{(3)}_{xxxx} I_{800nm} E_{bias}. \tag{4.1.15}$$

The measured intensity is

$$I_{measured} \propto E^2_{400nm} \propto (\chi^{(3)}_{xxxx} I_{800nm})^2 \left[(E_{THz})^2 + (E_{bias})^2 + 2E_{THz}E_{bias} \right], \tag{4.1.16}$$

which consists of three elements, where the third term on the RHS contains the desired information. Because the third term is dependent on the AC bias, this term will oscillate with the AC bias frequency, thus by measuring the intensity with a lock-in amplifier, locked in at the AC frequency, it is possible to average away all terms but the desired third term, and thus

$$I_{lock-in} \propto (\chi^{(3)}_{xxxx} I_{800nm})^2 E_{THz} E_{bias}. \tag{4.1.17}$$

As the detection pulse is much shorter than the THz pulse, the detection pulse is scanned in time over the THz pulse with the delay stage, resulting in the THz field being measured as a function of the delay time, τ.

FTIR

To give a more complete picture of the low loss abilities of the samples, a FTIR spectroscopy [84] measurement was also performed on the samples. A Vortex 70 from Bruker Optics was used for these FTIR measurements. As FTIR spectroscopy measures the reduction in intensity when the light is passed through the sample, it is not possible to use this measurement to obtain the complex refractive index, however the results still show if the samples have low loss areas. FTIR spectroscopy is based on a Michelson interferometer, where a white light source is divided in two by a beam splitter, each arm is reflected off a mirror to be sent straight back to the beam splitter. From there, what is now reduced to half of the intensity is sent from the beam splitter through the sample and then to a detector. The key element is that the difference in path length between the mirrors, will cause those wavelengths that have an even number of half wavelengths in path difference wavelengths to constructively interfere, and those where the difference in path length is an odd number of half wavelengths to destructive interfere. By moving the mirror, the spectral content of the intensity sent through the sample is changed. Measuring the intensity as a function of mirror position results in a spectrogram that can be Fourier transformed to give the information in wavenumber. By comparing this to a measurement performed without the sample, it is possible to obtain the intensity transmission.

The intensity transmission is the absolute square of the electric field transmission,

$$\frac{I_{sample}}{I_{ref}} = T_{intensity} = |T_{E-field}|^2. \tag{4.1.18}$$

The phase information that we obtain in the THz-TDS is not possible to obtain with this experiment, and it is thus not possible to derive the complex refractive index.

4.2 Refractive Index of Selenide Based Chalcogenides

A series of chalcogenide glass samples were prepared by our collaborators at the Laser Physics Centre at Australian National University in Canberra, Australia. The chemical compositions of the glasses all belong to the GeAsSe group, with various concentrations of the components and also of various sample thickness. The details of the samples can be seen in Table 4.1.

As the samples all have various thickness, it is not possible to directly compare any measured reflection or transmission, but instead the complex refractive index has to be retrieved in order to compare the samples. First a single sample, arsenic

Table 4.1: Chalcogenide Bulk Samples

Composition	Thickness [mm]
As_2Se_3	1.355
$Ge_{11}As_{22}Se_{67}$	1.35
$Ge_{15}As_{20}Se_{65}$	1.706
$Ge_{15}As_{25}Se_{60}$	1.07
$Ge_{33}As_{22}Se_{55}$	1.43

selenide, is investigated with a detailed explanation of the data retrieval after which the results from all the samples are compared.

4.2.1 Analysis of As_2Se_3 Measurement Data

Picometrix Results

For lower frequencies, the Picometrix system is used to obtain data of the transmission. An aperture was used to avoid any light might bypass the sample and cause an inaccurate measurement. The measured electric field can be seen in Fig. 4.3 where both the reference field and the transmitted field is shown.

As the Picometrix system have a very fast scan rate of 100 Hz, it is possible to average over a large number of scans to limit the noise. The sample measurement is a result of averaging over 100.000 scans, with the reference field being an average of 20.000 scans performed before the sample measurement and 20.000 performed after.

Looking at the transmitted field, a clear echo of the transmitted pulse is seen at roughly 560–570 ps with a second echo just visible at around 590 ps. To avoid accounting for these echoes in the refractive index retrieval, the part of the data used are limited to 510–550 ps as marked on the figure. The advantage of this is a great simplification of data treatment, with this limited data range, there is a risk that part of the initial transmitted pulse might be cut away in this process, and thus the data has to be studied to make sure this is not the case. However as the sample is thick, the risk of this is limited.

To retrieve the refractive index, first a Fast Fourier Transform (FFT) is performed on both electric fields, Fig. 4.4, in order to obtain $\tilde{T}(\omega)$, which can be seen in Fig. 4.5 for the absolute value and the phase respectively.

As it shows from Fig. 4.4, the noise at higher frequencies limits the data to a 0.1–1.2 THz range. With these it is possible to numerically retrieve the complex refractive index using Eq. (4.1.6). This has been done using a built-in function, `fsolve`, in Matlab. This function requires an initial guess, and for this, Eq. (4.1.8) was used to find the approximate index. The resulting real refractive index can be seen in Fig. 4.24 along the retrieved indexes from the other samples or in Fig. 4.19

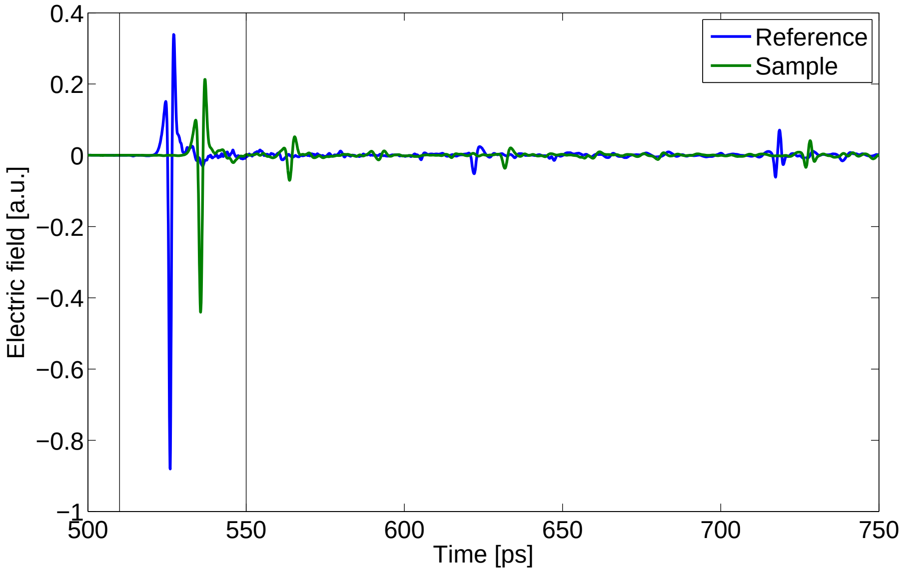

Figure 4.3: Raw data from the Picometrix system. The sampling time is 78.125 fs giving the measurement a bandwidth of 6.4 THz. The sample data is an average of 100.000 scans, with the reference data being an average over 40.000 scans, half performed before the sample measurement, the other half after. The vertical lines mark the part of the measured field that is used in retrieving the refractive index.

where all results for the index of arsenic selenide is shown. Similarly the loss can be seen in Fig. 4.25 or Fig. 4.20.

ABCD - Reflection Results

The reflection measurements performed in the ABCD setup was performed twice, to ensure that the obtained data was consistent and to see the variation that would happen as the sample and mirror was replaced with each other repeatedly.

To show that the aperture used to hold the mirror and the sample, a measurement was performed with neither the mirror nor a sample mounted. The resulting measurement, shown in Fig. 4.7, shows only noise. It can thus be safely assumed that the electric field measured is reflection only from either the mirror or the sample.

The data shown in Fig. 4.6 has a sampling rate of 10 fs, and each data set is a result of a 5 scan average. The limited number of averages is due to a time consuming scan rate and to avoid temperature drift of the laser to distort the data. As it shows, the reflected field appears to be slightly ahead of the corresponding reference fields. This is caused by the slight chance in position of the sample relative to the mirror.

The corresponding absolute reflection coefficient and the phase of the reflection

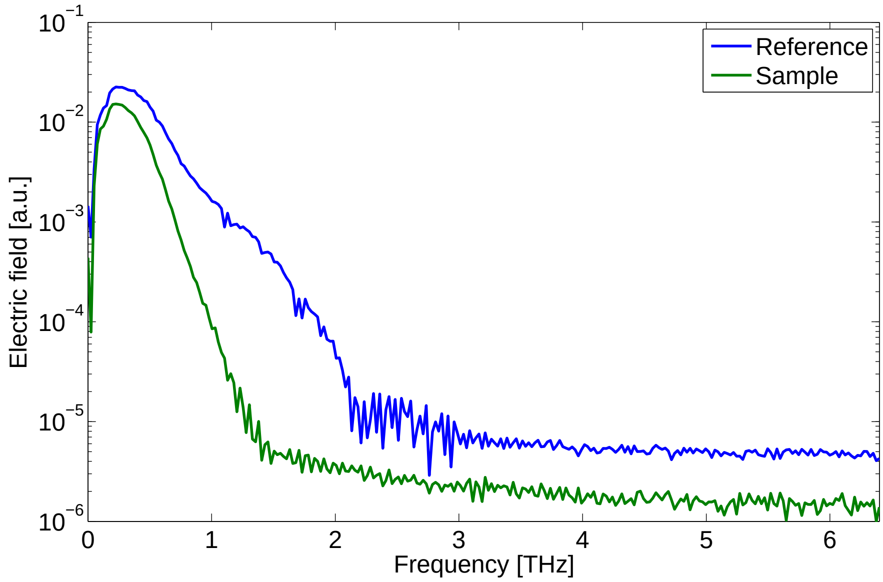

Figure 4.4: The Fourier transformed electric fields. It shows clearly that the sample have an increasing loss with frequency and that the sample noise on the sample measurement prevents any data above 1.2 THz to be used.

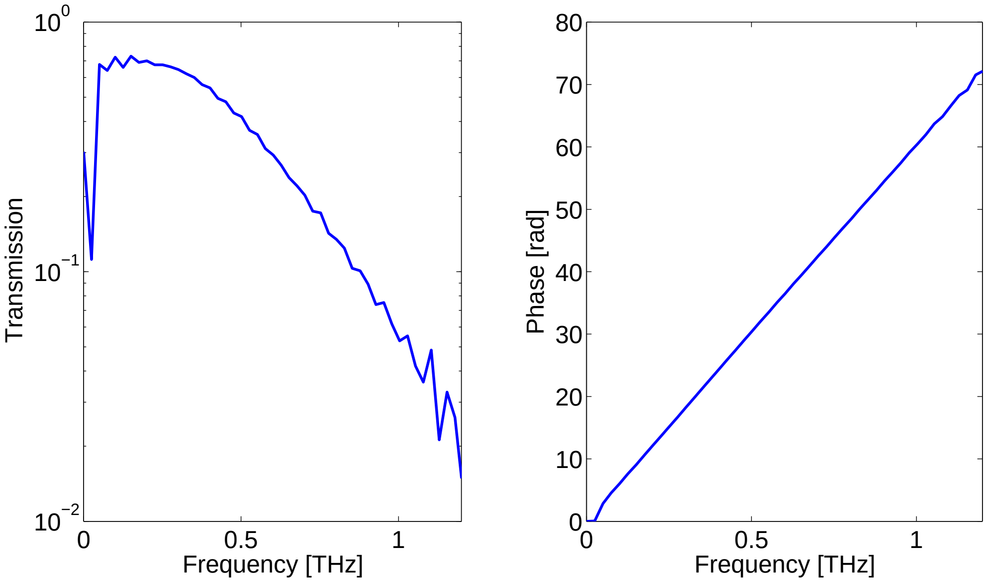

Figure 4.5: The absolute value (left) and phase (right) of the measured transmission.

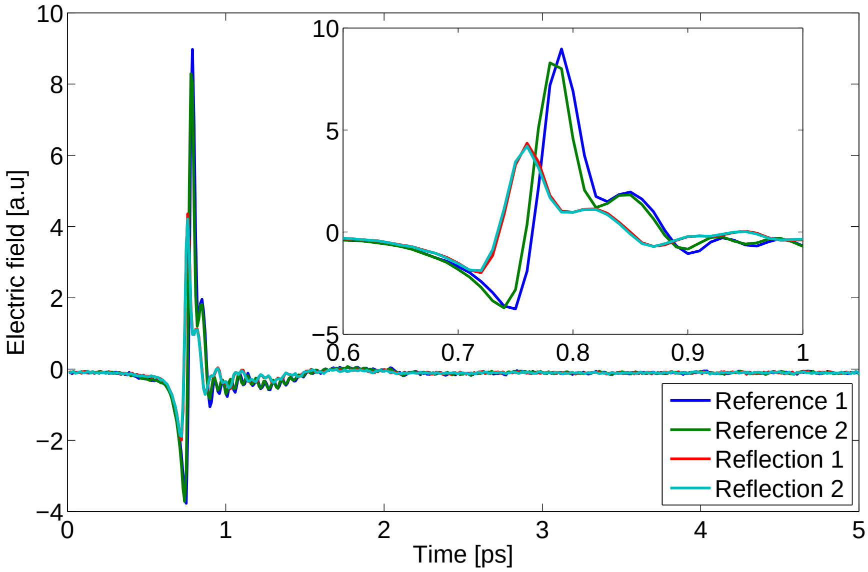

Figure 4.6: The measured electric field for the reflection measurement. The insert show a zoom of the data. The data was obtained in two different measurements simple labeled 1 and 2.

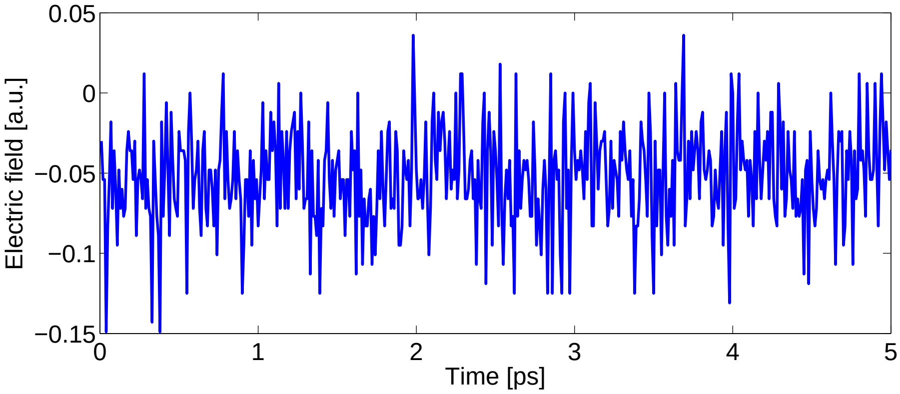

Figure 4.7: Measurement without either sample or mirror to show that the sample aperture is not having an effect on the reflection measurements, as nothing is reflected by the aperture itself. The measurement also shows that the measured data has a small offset.

can be seen in Fig. 4.9 and Fig. 4.10 respectively found by using a FFT of the electric fields. In Fig. 4.10, the initial uncorrected phase of each measurement is shown. From these phases, it is estimated how much the displacement, δx, the sample have to be corrected relative to the mirror. This estimate is performed by

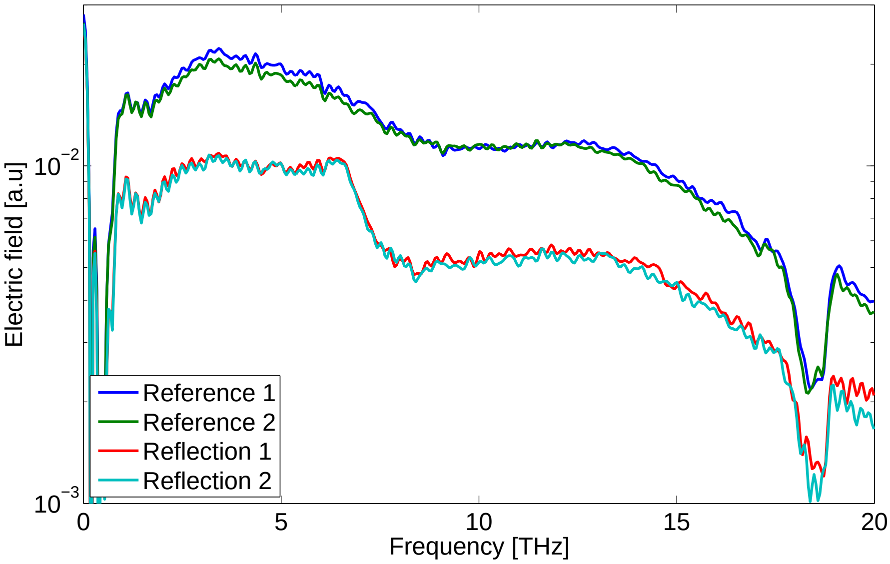

Figure 4.8: The Fourier transforms of the measured electric fields shown in Fig. 4.6. The data clearly show a dip at 18 THz caused by the silicon wafer used as a beam splitter in the setup. It is also seen that the amplitude decreases at about 15 THz causing the relative noise to increase. The frequency limit for this measurement has thus been set to 15 THz.

assuming that the phase of the reflection coefficient should approximately have a zero phase derivative. A negative phase derivative would mean that a negative phase would occur, which is not physical as the material is not a gain medium. A positive phase derivative on the other hand would cause the loss to be too great in the transmission window that can be seen in the transmission measurements. With this, it is estimated that measurement 1 should be shifted 4.43 μm and measurement 2 shifted 3.93 μm. The effect of this shift can be seen in Fig. 4.11 for the electric field. The reflection coefficient used to retrieve the complex refractive index is an average of the reflection found for the two measurements.

Because the phase correction of the reflection coefficient is an assessment, there is a degree of uncertainty to what the exact phase correction should be. The real and imaginary index,

$$n = \frac{1-|\Gamma|^2}{1+|\Gamma|^2-2|\Gamma|\cos\left(\Phi_\Gamma\right)} \tag{4.2.1}$$

$$\kappa = \frac{|\Gamma|\sin\left(\Phi_\Gamma\right)}{1+|\Gamma|^2-2|\Gamma|\cos\left(\Phi_\Gamma\right)}, \tag{4.2.2}$$

are both a function of the phase of the reflection coefficient. However as the real

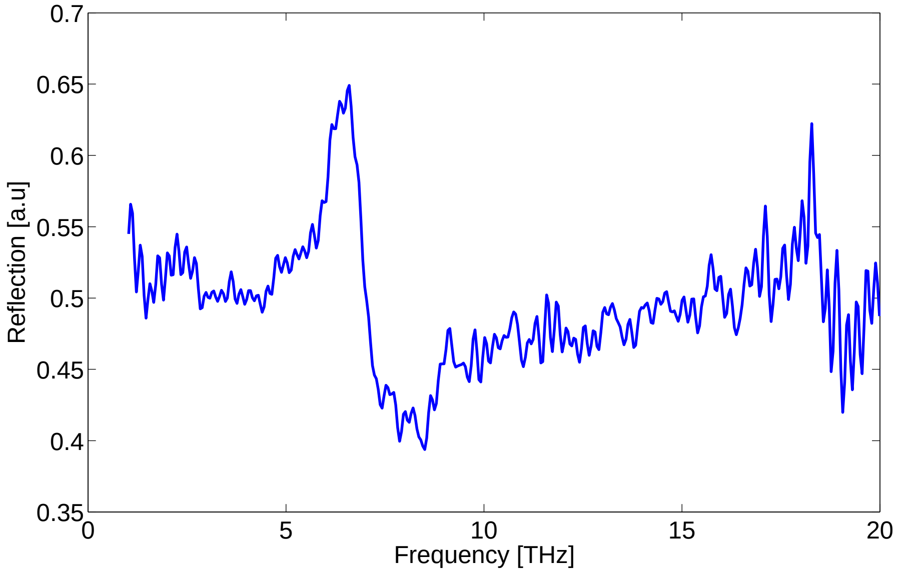

Figure 4.9: The absolute value of the reflection measured.

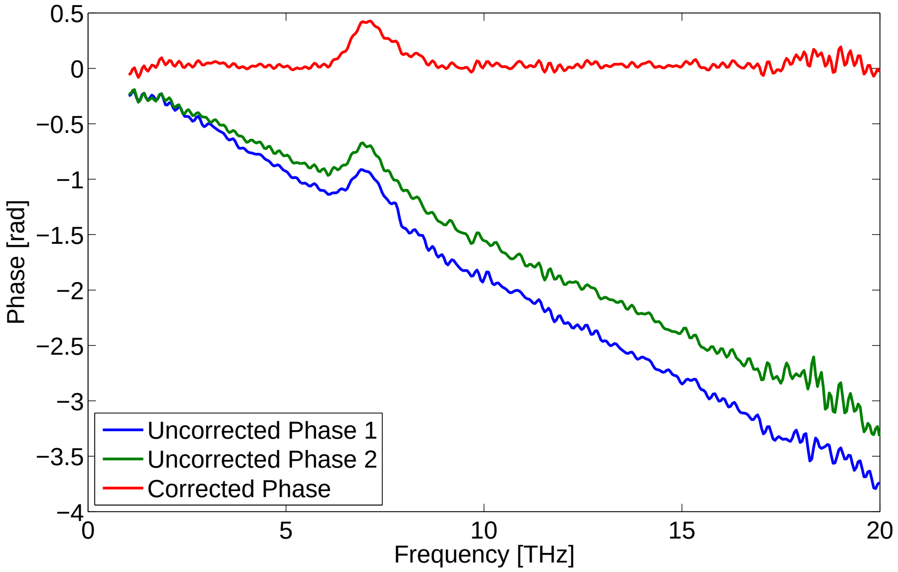

Figure 4.10: The uncorrected and corrected phase of the reflection measured.

index is dependent on the phase as $\cos(\Phi_\Gamma)$ and the phase change is very small, the uncertainty on the phase has only a small impact on the uncertainty of the refractive index. The imaginary index on the other hand is dependent also on the

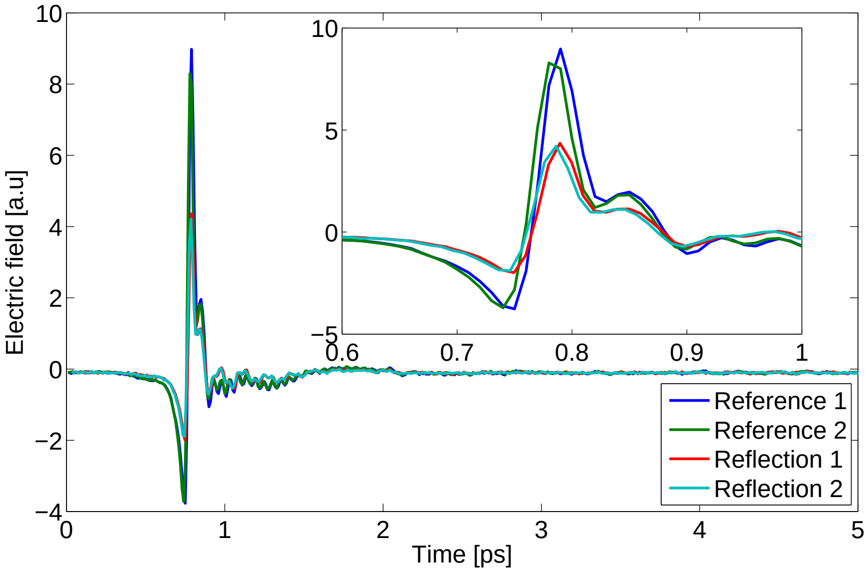

Figure 4.11: The phase adjusted electric fields for the reflection measurement. The insert show a zoom of the data. Sample 1 has been shifted what corresponds to a distance 4.43 μm and 3.93 μm for sample 2. In time this correspond to 29.5 fs and 26.2 fs respectively.

phase change as $\cos(\Phi_\Gamma)$ but more importantly as $\sin(\Phi_\Gamma)$ in the nominator. Thus a change in the assessment of the phase correction, will greatly change the retrieved imaginary index. This effect is clearly seen in Fig. 4.12, where the phase correction as described by Δx has been changed ± 0.1 μm.

The small phase change will in one instance even cause κ to be negative, which would mean that the signal would experience a gain in the sample.

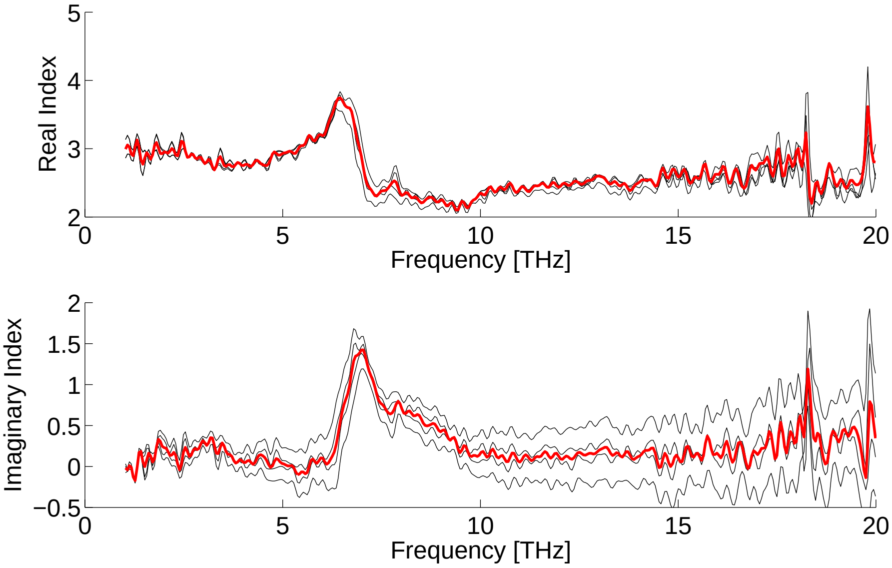

Figure 4.12: The index as retrieved with the assessed phase correction (red) and the corresponding index if the phase correction, Δx has been changed ±0.1 μm in both measurements.

ABCD - Transmission Results

The measured electric fields from the transmission measurements performed on the ABCD setup is shown in Fig. 4.13 with the corresponding Fourier transform in Fig. 4.14. From the Fourier transform it is clearly seen from the transmitted pulse that no light is transmitted in from about 1 THz to around 10 THz. This makes it very challenging using this measurement to retrieve the refractive index as it will be difficult to determine the correct phase in the transmission window.

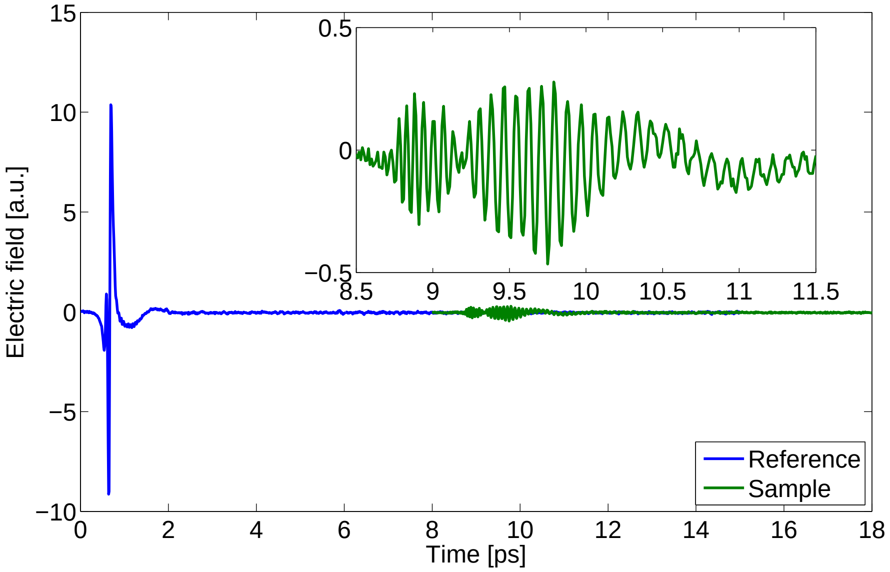

Figure 4.13: The measured electric field in the transmission measurement. The insert shows a zoom of the transmitted pulse.

The absolute transmission of the sample and the phase of the transmission is shown in Figs. 4.15 and 4.16 respectively.

With the retrieved index from the reflection measurements, it is possible to determine what the phase of the transmission would be based on this index. Having calculated that, it is possible to approximate the phase offset of the transmission measured, which is what is shown in Fig. 4.16. Having approximated the phase, the index can then be determined with Eq. (4.1.6) as was done with the Picometrix data. The corresponding index and loss is shown in Figs. 4.19 and 4.20 respectively.

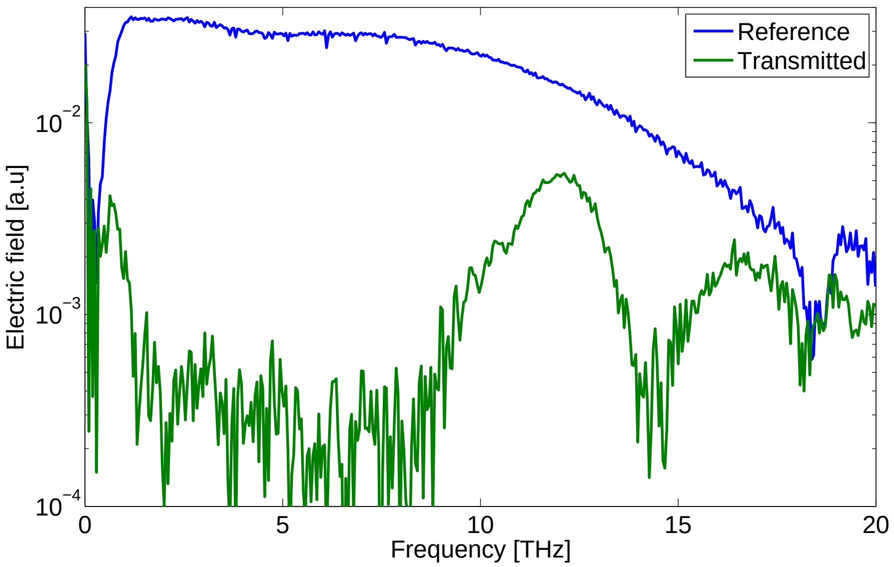

Figure 4.14: The Fourier transform of the measured electric fields as shown in Fig. 4.13. A transmission window at 10–14 THz is clearly seen as well as second window around 16–17 THz.

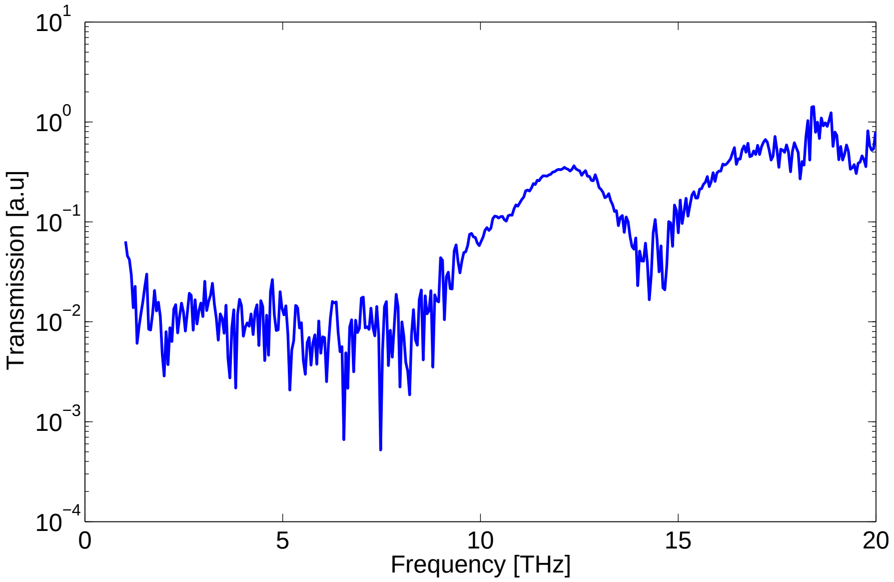

Figure 4.15: The absolute value of the transmission measured.

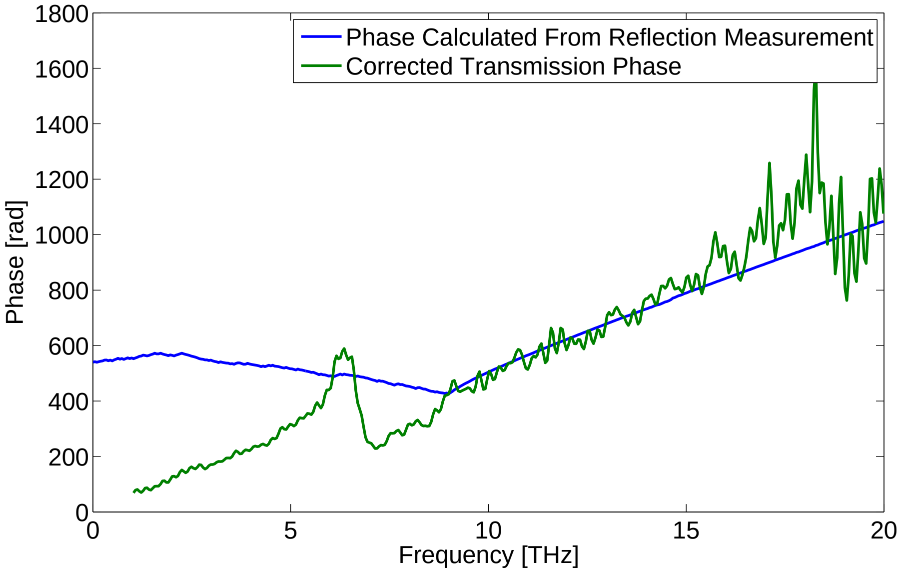

Figure 4.16: The uncorrected and corrected phase of the transmission measured.

FTIR data

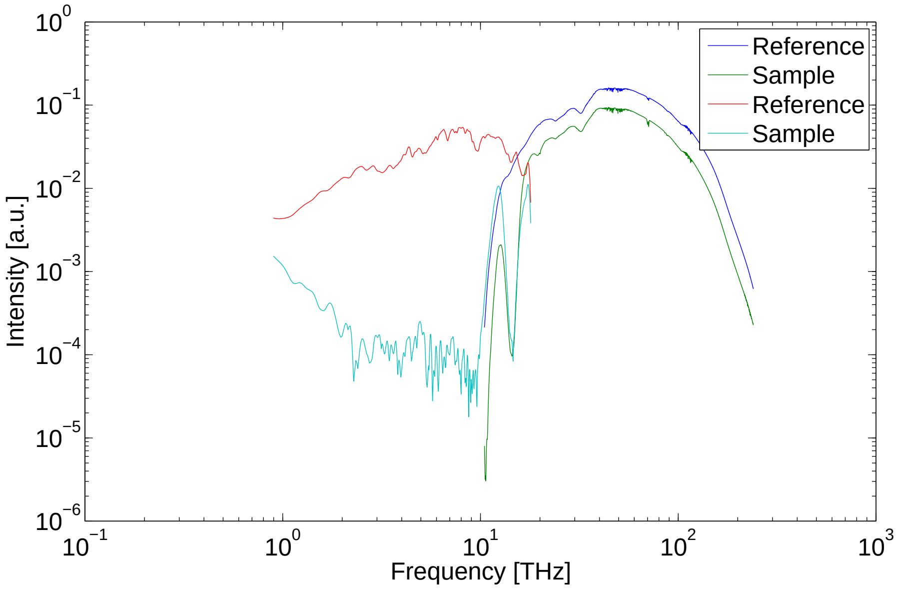

Figure 4.17: The measured intensity by the FTIR spectroscope. The bandwidth is divided in two as the beam splitter in the spectroscope has to be manually changed.

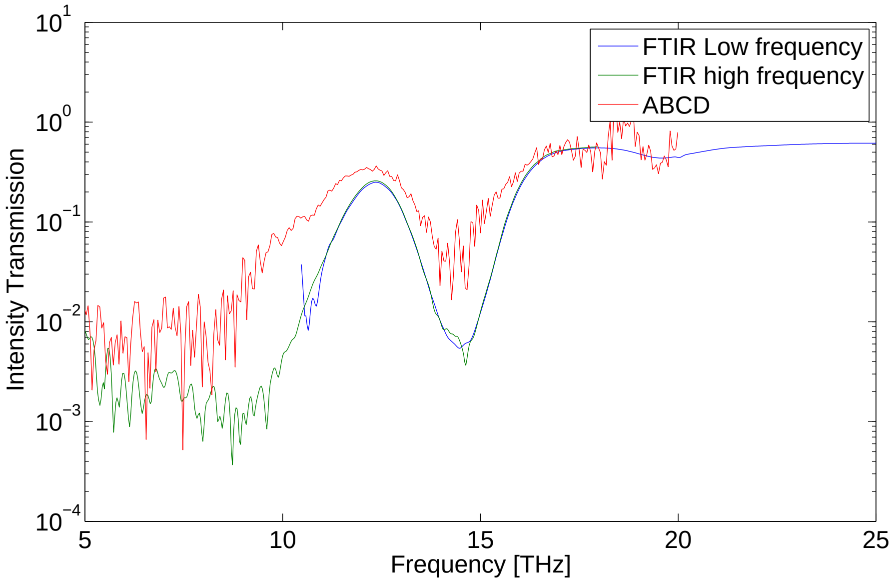

Figure 4.18: The transmission as measured with the FTIR and the ABCD setup.

The measured FTIR transmision show the same characteristics as the ABCD transmission measurement, Fig. 4.18 with a transmission window at 11–14 THz. Furthermore it the FTIR measurement shows more clearly that it is a resonance causing loss at 15 THz before there is a new transmission region starting at 16 THz.

4.2.2 Retrieved Refractive Index

The retrieved refractive index and loss for As_2Se_3 and $Ge_{11}As_{22}Se_{67}$ is shown in Figs. 4.19 and 4.20 where data from the 3 measurements, Picometrix, ABCD reflection and transmission are combined. All raw data, Fourier transforms and corresponding reflection or transmission coefficients are shown in App. B.

Of the two glasses, the $Ge_{11}As_{22}Se_{67}$ glass generally has a lower index than As_2Se_3. The only exception is around a strong resonance that is apparent in both glasses. For As_2Se_3 it is 6.7 THz where it for $Ge_{11}As_{22}Se_{67}$ is at 7 THz. As the reflection measurement data have a high relative noise level, it is not possible to determine if there are any smaller resonances in the glass, as it is indeterminable from the noise. The noise of the reflection measurement is clearly seen at 11–14 THz where the transmission measurement yielded data as well. There is a good overlap in the index determined from the two measurements, with the transmission data being less noisy. The As_2Se_3 glass has an index around 3.1 before the resonance with a dip to 3 at 3–4.5 THz. The $Ge_{11}As_{22}Se_{67}$ glass shows the same dip from 2.85 to 2.75. At the resonance, the index As_2Se_3 rises to about 4.25 and dips to 2.15

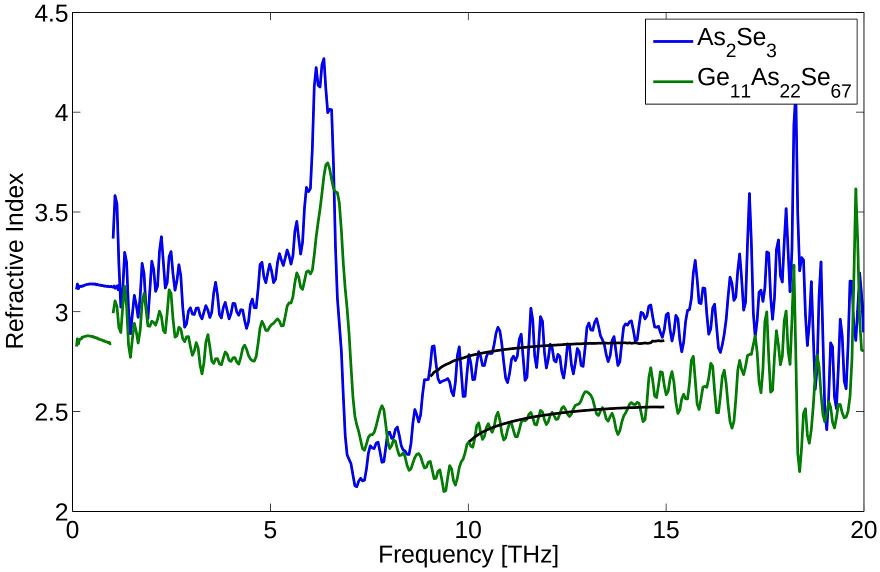

Figure 4.19: Refractive index as comprised of three measurements. For low frequencies, the index has been determined with the Picometrix data with the reflection measurements being the base for the rest of the frequency range. Around 10–15 THz the transmitted electric field through the glasses was used to supplement the reflection measurement (shown in black for both samples).

before settling at an index around 2.8 as shown by the transmission measurement. The $Ge_{11}As_{22}Se_{67}$ glass peaks at the resonance at 3.75 with a straight dip to 2.3 and slow decrease to 2.1 at 10 THz with a quick increase to 2.5 as shown by the transmission measurement.

The corresponding loss of the glasses are shown in Fig. 4.20, as found by $\alpha(\omega) = 2\omega\kappa/c$. At low frequencies, the loss of all materials follow a universal power law scaling [85]. When the wavelength get sufficiently small, the mean free path in the material get comparable to the wavelength of the plane wave, which changes the loss dynamics. This transition is called the Ioffe-Regel transition [86]. However, due to the noise of the reference measurements, it is not possible to see when this transition occurs, other than it occurs above 1 THz, as is seen later from Fig. 4.25 where the loss found with the Picometrix system is shown in more detail.

The strong resonance seen in the refractive index is also clearly visible in the loss, with As_2Se_3 having a strong resonance at 6.7 THz and for $Ge_{11}As_{22}Se_{67}$ at 7 THz. $Ge_{11}As_{22}Se_{67}$ also have smaller resonances at 8–9 THz. From the reflection measurements, any transmission windows are not visible due to the noise in the measurement and the uncertainty of the phase correction. However, looking at the results from the transmission it is clear that both glasses have a transmission

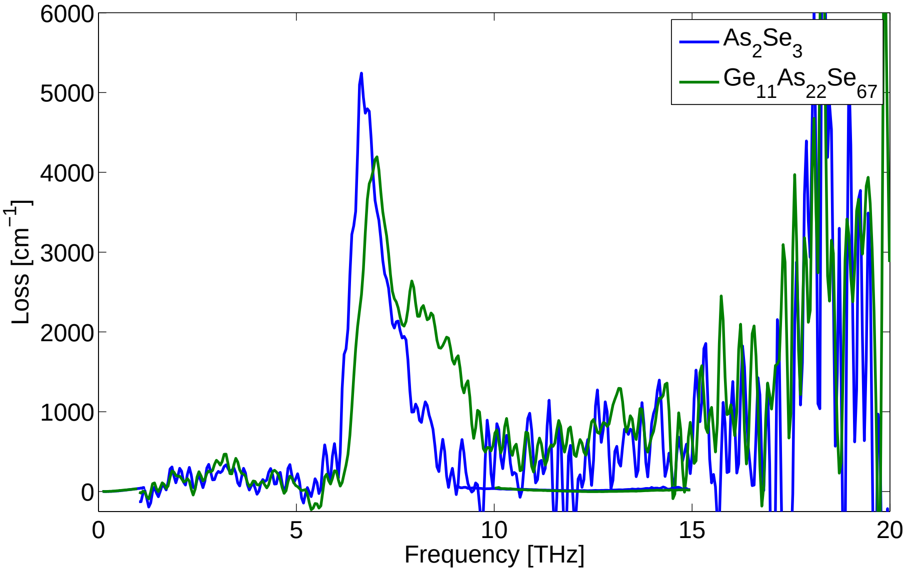

Figure 4.20: The loss as comprised of three measurements. For low frequencies the Picometrix data was used and for the 10–15 THz region the ABCD transmission measurement was used. The reflection measurements is the base for the estimated loss in the range above 1 THz.

window around 11–14 THz where the loss is estimated to be 15 cm^{-1} for As$_2$Se$_3$ and 10 cm^{-1} for Ge$_{11}$As$_{22}$Se$_{67}$. As discussed later with Fig. 4.26, it also appears from the transmission coefficient that Ge$_{11}$As$_{22}$Se$_{67}$ have a narrow transmission window at 5 THz.

Arsenic sulfide glass, As$_2$S$_3$, shows a similar strong resonances at 10 and 11.5 THz [78]. The shift in frequency between the resonances for As$_2$S$_3$ and As$_2$Se$_3$ can be due to the smaller mass of the sulfide ions as the phonon frequency is determined as $\omega = (k/m)^{1/2}$ where k is the spring constant determined by the strength of the As-S or As-Se bond.

The two glasses, Ge$_{15}$As$_{20}$Se$_{65}$ and Ge$_{15}$As$_{25}$Se$_{60}$, have a refractive index behavior, shown in Fig. 4.21, very similar to that of Ge$_{11}$As$_{22}$Se$_{67}$. This is expected as the chemical compositions are relatively similar as well. Both Ge$_{15}$As$_{20}$Se$_{65}$ and Ge$_{15}$As$_{25}$Se$_{60}$ have a strong resonance at 7 THz, seen in Fig. 4.22, with an index that peaks at 3.7 at 6.6 THz before dropping to 2.5 at 7.3 THz with a continuous small decline to an index of 2.1 at 9.5 THz before increasing to a value of 2.65 and 2.6 for Ge$_{15}$As$_{20}$Se$_{65}$ and Ge$_{15}$As$_{25}$Se$_{60}$ respectively at 13 THz. Ge$_{15}$As$_{20}$Se$_{65}$ has an index at 2.9 for low frequencies increasing to 3.1 at 2.5 THz before dropping again to 2.9 around 3–4.5 THz. Ge$_{15}$As$_{25}$Se$_{60}$ show the same characteristic with the only significant difference being a lower index at 2.8 for frequencies under 1 THz.

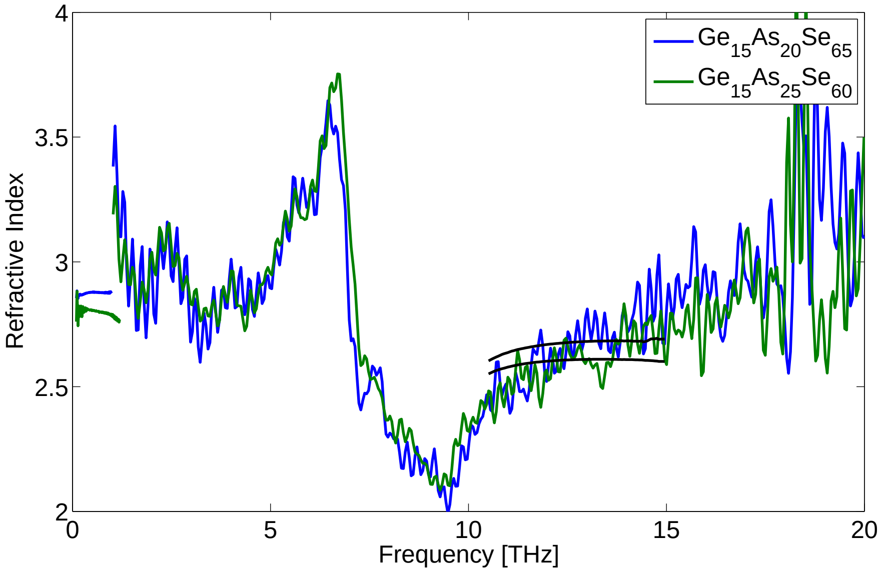

Figure 4.21: Refractive index for two GeAsSe glasses as in Fig. 4.19.

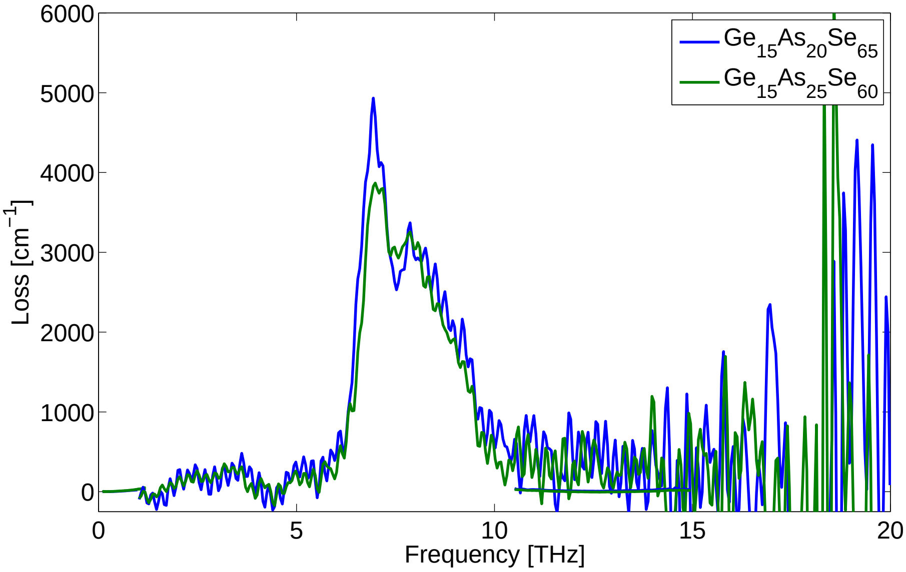

Figure 4.22: Loss for two GeAsSe glasses as in Fig. 4.20.

In the plot of the loss for these two glasses, Fig. 4.22, it shows that they have the same resonances around 8–9 THz as $Ge_{11}As_{22}Se_{67}$ which is what causes the index decline of these glasses in the same frequency region. To show how the index of

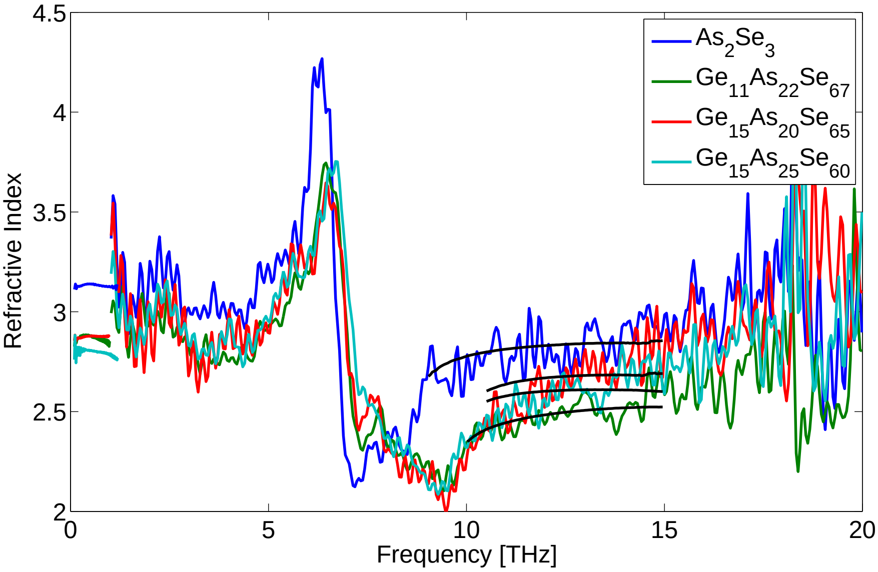

Figure 4.23: Combined plot of the index for the four GeAsSe glasses shown in Figs. 4.19 and 4.21.

the glasses all compare to each other, the index for all the four glasses tested in the reflection measurement are shown in Fig. 4.23.

With the Picometrix data, the real part of the refractive index is shown in Fig. 4.24 for all 5 samples in the 0.1–1 or 1.2 THz range. The glasses have indexes at 3.1, 2.85, 2.85, 2.8 and 2.65 for As_2Se_3, $Ge_{11}As_{22}Se_{67}$, $Ge_{15}As_{20}Se_{65}$, $Ge_{15}As_{25}Se_{60}$ and $Ge_{33}As_{22}Se_{55}$ respectively over the measurement range. As the compositions of $Ge_{11}As_{22}Se_{67}$ and $Ge_{15}As_{20}Se_{65}$ are similar, it is, as we also see in the figure, expected that the refractive index is very similar, however as we see in Fig. 4.25, the loss of the two compositions differ. As mentioned, the loss of the glasses will at long wavelengths follow a power law scaling which appears to hold true for the entire Picometrix frequency range, as also seen in the loglog plot of the loss. As the power law holds for the Picometrix range shows that the Ioffe-Regel transition will be outside this range.

The absolute transmission of each chalcogenide glass is shown in Fig. 4.26 for the measurements with the ABCD setup. As the glass samples have varying thickness, it is not possible to directly compare the transmission. However, it is clearly seen that the germanium based glasses all have an apparent transmission window at 5 THz, indicating a shift in phonon resonances away from 5 THz at either side compared to As_2Se_3. The loss transmission at 5 THz has a very narrow bandwidth and is lower in absolute value than the transmission window at 12.5 THz. Even though the index is greater on the right side of the strong resonance that is seen for As_2Se_3

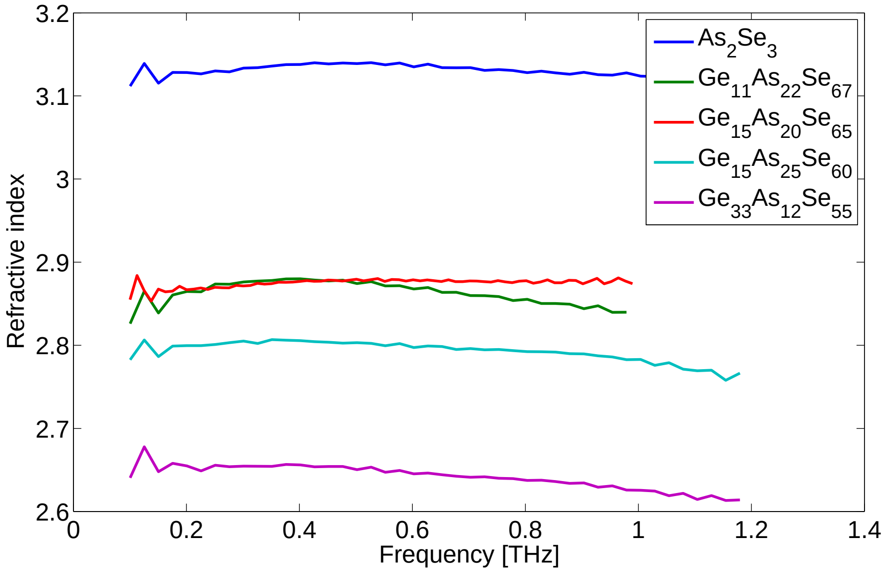

Figure 4.24: The refractive index n for 5 GeAsSe glasses retrieved from measurements with a Picometrix system.

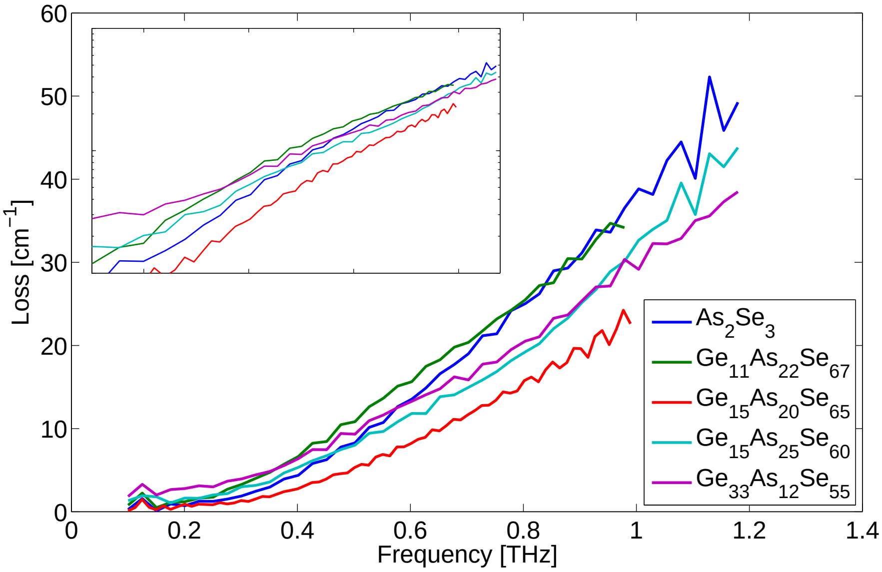

Figure 4.25: The loss of 5 GeAsSe glasses. The insert show the loss plotted on a loglog scale.

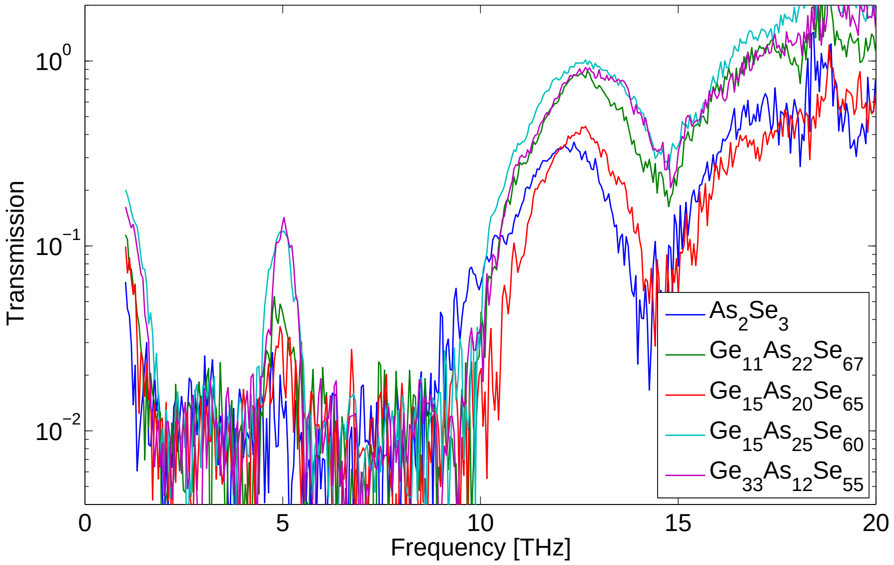

Figure 4.26: The transmission of the five GeAsSe glasses as measured with the ABCD setup.

and $Ge_{11}As_{22}Se_{67}$ and is expected to be present for the other glasses as well, the loss will be significantly greater than at 12.5 THz. Assuming no loss and an index for $Ge_{11}As_{22}Se_{67}$ of 2.8 at 5 THz and 2.5 at 12.5 THz, the difference in transmission only from Fresnel refraction is 78% at 5 THz and 81%.

To complement the transmission measurements at high frequencies and going into the mid-infrared, the measured absolute transmission with the FTIR spectroscope is shown in Figs. 4.27 and 4.28. The FTIR measurements show the same characteristics in the THz region as those seen with the ABCD setup. All samples display a resonance at 14.7 THz with a transmission window at 11–14 THz. The glasses with germanium furthermore show a resonance at 23.8 THz which is also clearly seen in Fig. 4.28 at 12.6 μm. Althought the FTIR measurements show the same characteristics, as seen in Fig. 4.29, the two measurements does not find the same absolute value of the transmission.

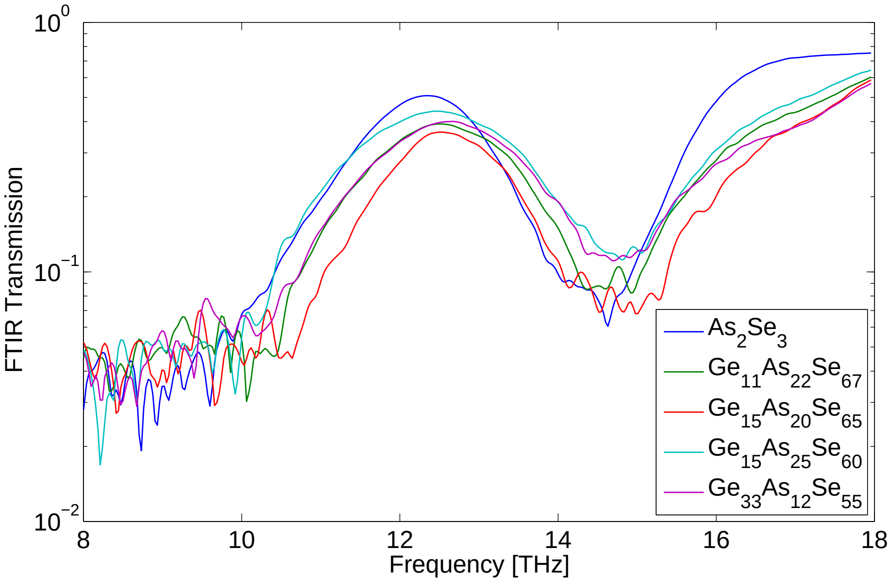

Figure 4.27: FTIR Transmission shown in the THz regime.

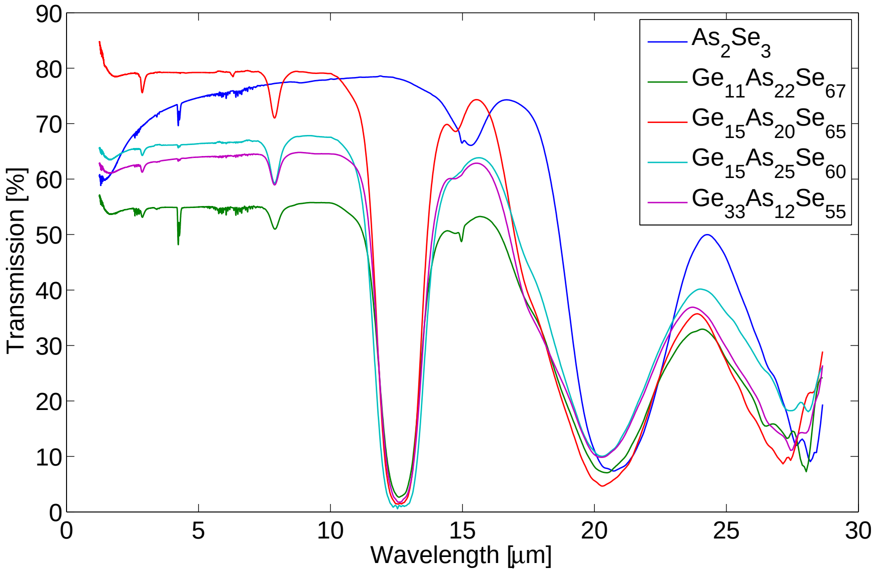

Figure 4.28: FTIR Transmission shown in the mid-infrared. The samples have varying thickness, so no direct comparison can be made, but it clearly shows that the germanium causes a strong resonance at 12.6 μm that limits the mid-infrared transmission window as well as a smaller resonance at 7.8 μm.

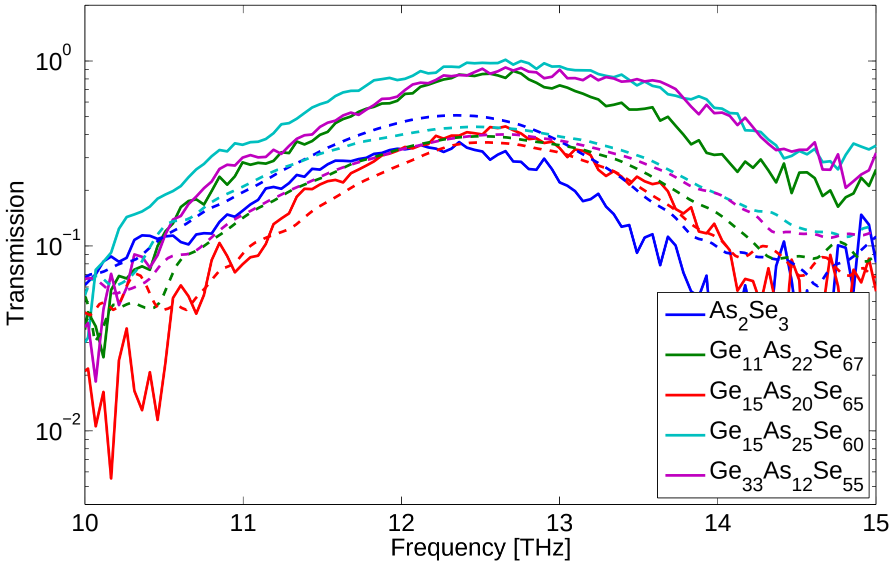

Figure 4.29: The transmission measured by the FTIR spectroscope (dashed) and the ABCD setup (solid).

4.3 Time Resolved THz Spectroscopy

THz-TDS is not a time-resolved measurement, the measured index is the static index. However it is also possible to make TRTS in a pump-probe configuration where it is possible to measure the transient conductivity dynamics in the samples [87, 88, 89]. The premise for this is to use a pump pulse to photoexcite carriers into a nonequilibrium state, creating free carriers, whose dynamic can be measured with the THz probe pulse. The following subsection describes the theory behind this experiment with the experiment setup being described in Sec. 4.3.2.

4.3.1 Photoconductive Effect

Measuring the photoconductive effect is divided in two measurements, a 1D scan and a 2D scan. The scans are named such as the experiment require either 1 or 2 delay stages to be used, respectively. The 1D scan gives information on the carrier mobility and the 2D scan is used to determine the complex conductivity. The 1D scan is also used ahead of a 2D scan to determine at what delay time the pump pulse coincides with the probe pulse, to determine the scan limits of the 2D scan.

1D scan

The 1D scan is based on ignoring the phase information and only look at the peak of the probe THz pulse as it has propagated through the sample. The pump pulse is then scanned in time relative to the peak of the probe pulse. At the peak of the probe pulse, it can be assumed that all frequency components are in phase. At negative delay times, where the pump pulse arrives after the probe pulse, there will be no effect on the measured peak value, as there will be no free carriers to attenuate the probe pulse, the unattenuated value will be called E_0. As the pump pulse is scanned in time to arrive before the probe pulse, the peak of the probe pulse will decrease due to the attenuation of free carriers in the sample, called $V_{pump}(\tau)$. As the pump pulse is scanned further ahead of the probe pulse, the attenuation of the peak value of the probe pulse, will decrease, as the free carriers recombine and the sample return to equilibrium state, thus $E_{pumped}(\tau) \rightarrow E_0$. An example of a 1D scan is shown in Fig. 4.30.

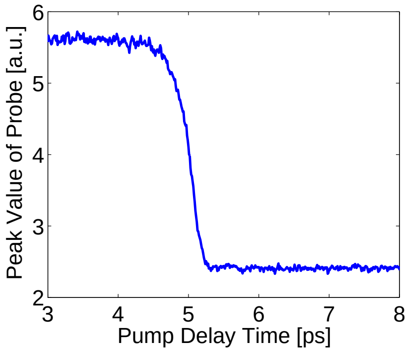

Figure 4.30: Example of a short 1D scan of bulk GaAs used to calibrate the probe delay for testing GeAsSe. The change in peak value of the probe is clear around 5 ps, where in times before that, the pump pulse arrives after the probe pulse and no attenuation is seen to after 5 ps where the pump pulse arrives before the probe pulse and a great attenuation is seen. The relaxation of the carriers happen on a timescale of several 100 ps, which is why the effect is not seen in this figure.

If the material tested is a thin conducting layer, thickness $d \ll \lambda$, on a substrate, and the reduction in peak value of the probe pulse is low, the carrier mobility can be estimated with [88]

$$\mu = \frac{n_{substrate} + 1}{Z_0 e d n_{max}} \left(\frac{E_0 - [E_{pumped}(\tau)]_{min}}{E_0} \right), \tag{4.3.1}$$

where Z_0 is the impedance of vacuum, e is the electron charge and n_{max} is the maximum number of injected carriers determined by

$$n_{max} = \frac{\eta F \lambda (1 - R)}{hc\delta}, \tag{4.3.2}$$

where η is the quantum efficiency, F is the energy per area of the pump pulse, R is the reflection coefficient of the pump pulse off the sample and δ is the pump penetration depth.

When performing this experiment, it should be noted that the induced carriers might change the index of the sample, which in turn change the propagation time through the sample, thus the peak of the probe pulse might not be located at the same delay time as without the pump pulse being present.

2D scan

A 2D scan is differs from a 1D scan by measuring the entire THz pulse and not just the peak of the pulse. With this, you obtain a data set, $E_{sample}(t, \tau_{pump})$ that can be used to determine the complex conductivity. Introducing the pump-prope delay time $u = t - \tau_{pump}$, the complex conductivity can be found by determining the complex dielectric function, similar to Sec. 4.1.1, as a function of the pump-probe delay time by [88]

$$\tilde{T}(\omega, u) = \frac{\tilde{E}_{sample}(\omega, u)}{\tilde{E}_{ref}(\omega)}, \tag{4.3.3}$$

and the relation between the complex dielectric function and the conductivity as [87]

$$\varepsilon(\omega) = \varepsilon_{non-excited}(\omega) - \frac{\mathrm{i}\sigma(\omega)}{\varepsilon_0 \omega}. \tag{4.3.4}$$

4.3.2 Experimental Setup

The experimental setup for a TRTS experiment is based on the ABCD setup explained in Sec. 4.1.3 with the inclusion of a pump pulse incident on the sample. The schematics of the setup is shown in Fig. 4.31. This pulse pump is obtained by inserting a beam splitter to separate part of the source laser. This beam is then directed through a delay stage to control the timing of the pump pulse. The chalcogenide samples have band gap energy above 800 nm, it is thus necessary to use a β-BBO crystal to frequency double the light to have enough photon energy to excite carriers in the sample. Lastly a lens is used to focus the light down on the sample. It is highly important that the pump spot on the sample is well aligned with the probe spot, as otherwise the carriers will recombine without being detected by the THz probe pulse.

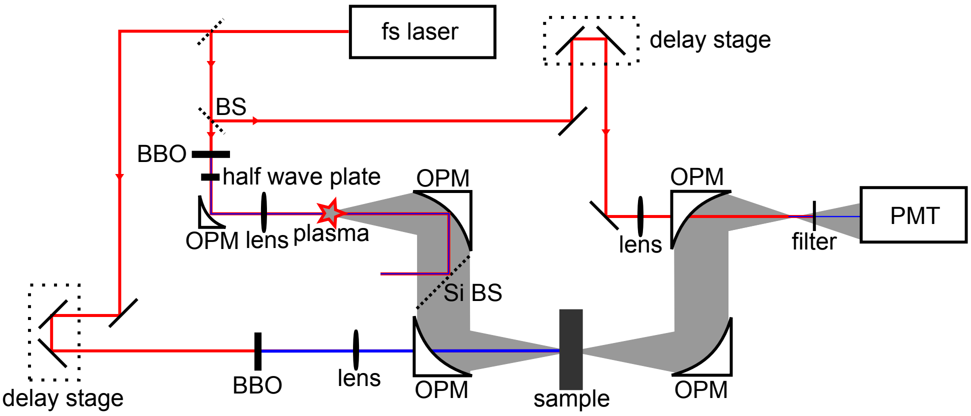

Figure 4.31: Setup of the TRTS experiment. It is based on the ABCD (transmission) experiment, described earlier with Fig. 4.2, with a part of the 800 nm laser light used to excite carriers in the sample. In this specific experiment, a β-BBO crystal was used to frequency double the light to 400 nm in order to be above the band gap energy of the sample.

4.3.3 Measurement Results

Two different sets of samples were available for testing. A set of bulk samples, as described in Sec. 4.2 and a set of thinfilm samples. The thinfilm samples (1–2 μm thickness) is a range of GeAsSe chalcogenide deposited on quartz glass. Normally, for THz measurements, the preferred substrate is high resistivity silicon [78], as this is transparent in the THz range up to 18 THz, where there is a resonance. However as silicon is also a semiconductor it is not feasible for this type of measurements, which is why the non-conducting quarts glass was chosen. The limits for this material however is that it is black above roughly 5 THz.

Thinfilm Sample

As described earlier, the first measurement to perform is the 1D scan which was initially done on the thinfilm sample. First a known GaAs sample was tested, as shown in Fig. 4.30, to determine when the pump pulse arrives compared to the probe pulse, thus indicating the search perimeters when testing the unknown GeAsSe sample. When testing the thinfilm, no measurable difference was observed in the peak value. This could be because the number of excited carriers was too small, either from insufficient pump power or because the penetration depth in the sample was too great. The pump power was therefore increased, even to an extent where the sample took physical damage, still without experiencing any difference in probe peak value. To overcome the issue of penetration depth, the thinfilm sample was replaced with a bulk sample.

Bulk Sample

The bulk sample used was the As_2Se_3 composition which have a well known band gap. Similarly to the thinfilm sample however, no difference in probe peak value was observed. This observance, together with the research showing that only free holes are excited, leads to the conclusion that the mobility of the free holes are too low to be observed with this experimental setup. The investigation into the carrier dynamics of the chalcogenide GeAsSe glasses where therefore not continued.

4.4 Future Ideas

As the complex refractive index now has been determined for these GeAsSe chalcogenide glasses, it could be interesting to attempt to determine their nonlinearity in the infrared regime. This is possible as new THz radiation techniques using lithium niabate crystals have made it possible to obtain electric field strengths strong enough to perform z-scans of materials in the THz regime.

THz Generation by Optical Rectification in Lithium Niobate

The generation of THz radiation in a second order nonlinear crystal like ZnTe or $LiNbO_3$ is possible by utilizing the difference frequency mixing of the spectral components in ultra short laser pulses [8]. The optimum coupling between pump pulse and THz pulse occurs when there is phase velocity matching, however in lithium niobate, the index at THz frequencies exceeds the group index for the usual 800 nm pump pulses. This problem is overcome by tilting the intensity front of the pump pulse. Using this technique, THz pulses with several μJ pulse energy has been demonstrated for THz pulse with a bandwidth of 0.1–3 THz [8]. These pulse have sufficient peak power to be used to investigate the nonlinearity of materials in a z-scan experiment.

Z-Scan

The closed z-scan technique is based on sending a focused probe beam through the sample under test and measuring the propagated intensity through an aperture at the detector. By moving the sample back and forth in the focused beam, the nonlinear focusing or defocusing changes the measured intensity [90]. This technique has previously been used to study doped semiconductors with THz pulses [91]. Another study used the second harmonics generated in a lithium niobate crystal to determine the second order nonlinearity of the crystal at THz frequencies [70].

5

Conclusion

The use of soft glass materials will play an increasing role as more interest is gathered at optical technologies in the mid- and far-infrared. In this paper, work has been presented that will further the use of these materials as we have outlined some of the material properties of these glasses.

A brief introduction to the glasses has been given, showing that there is a broad range of possible glasses within this category. As many of these glasses are relative unknown, work has been done to outline if certain specific glasses are of interest in using for mid-infrared and THz applications.

The dispersion of commercially available fluoride fibers were measured to determine if they would be good candidates as a medium for mid-infrared supercontinuum generation while also providing details necessary when modeling the supercontinuum generation in these fibers. In order to expand on the knowledge of the effect of two photon absorption on supercontinuum generation in chalcogenide fibers, an analytical model was derived to show the effect of this nonlinear loss on soliton self frequency shift, an essential part of obtaining a broad supercontinuum spectrum.

A range of chalcogenide glasses comprised of GeAsSe has been studied in the THz regime, with both transmission and reflection measurements allowing to determine the complex refractive index. These measurements show that these glasses have interesting transmission windows at high THz frequencies centered around 12.5 THz as well as having transmission at THz frequencies below 1 THz.

As these chalcogenides are amorphous semiconductors, it was also studied whether it was possible to determine the complex conductivity of these materials, as it should be possible to excite carriers. However it was discovered in experiments, that the mobility of these free carriers, consisting only of free holes, has a mobility that is too high to measure with the experimental setup available.

In conclusion, it has been shown that the soft glasses tested here has potential for use in nonlinear optical applications. A model was presented to describe the effect of two photon absorption on soliton self frequency shift, giving a useful tool in determining the potential use of chalcogenide fibers as a medium for supercontinuum generation. It has been showed that GeAsSe chalcogenide glasses show transmission in the THz regime and the next logical step would be, now that the complex refractive index is known, to attempt to determine the nonlinear index at THz frequencies using high power lithium niobate THz radiation setups.

Appendix A

Derivations

A.1 Dispersion

The measured power spectrum is from the field that consist of a sum of the field that propagated through the SMF, denoted f, and the field that propagated through air, denoted r. The field can be expressed as

$$E = \frac{1}{2}\left[E_f \exp\left(\mathrm{i}\beta(\omega)L\right) + E_r \exp\left(\mathrm{i}k_0(\omega)d\right)\right]\exp\left(-\mathrm{i}\omega t\right) + c.c., \tag{A.1.1}$$

where L is the length of the fiber with the propagation constant β, d is the difference in length in free air the fields travel, where it is assumed that air has the propagation constant, k_0, of vacuum. This field leads to a power spectrum, $P(\lambda)$, proportional to

$$P(\lambda) \propto |E|^2 \propto |E_f|^2 + |E_r|^2 + 2E_f E_r \cos\left(k_0 d - \beta L\right). \tag{A.1.2}$$

The oscillating term with the phase

$$\phi(\omega) = k_0(\omega)d - \beta(\omega)L \tag{A.1.3}$$

gives rise to periodically constructive and destructive interference. It is this periodicity that is used to determine the dispersion, D.

If the phase term is differentiated twice with respect to ω you obtain

$$\frac{d^2\phi}{d\omega^2} = -\frac{d^2\beta(\omega)}{d\omega^2}L = -\beta_2 L \tag{A.1.4}$$

where it is used that the wave number k_0 is linear in frequency. The second derivative of the propagation constant is related to the dispersion constant by

$$D = -\frac{2\pi c}{\lambda^2}\beta_2. \tag{A.1.5}$$

As the measured power spectrum is done in wavelength, the phase derivative is rewritten to be differentiated by wavelength using this derivate rule

$$\frac{d^2 f\left(y(x)\right)}{dx^2} = \frac{d^2 f(y)}{dy^2}\left(\frac{dy}{dx}\right)^2 + \frac{df(y)}{dy}\frac{d^2 y}{dx^2} \tag{A.1.6}$$

leading to

$$\frac{d^2\phi}{d\omega^2} = \left(\frac{d\lambda}{d\omega}\right)^2 \frac{d}{d\lambda}\left(\frac{d\phi}{d\lambda}\right) + \frac{d^2\lambda}{d\omega^2}\frac{d\phi}{d\lambda}. \tag{A.1.7}$$

As there is 2π between each constructive interference peak, it can be approximated that

$$\frac{d\phi}{d\lambda} \approx \frac{2\pi}{\Delta\lambda(\lambda)} \tag{A.1.8}$$

where $\Delta\lambda$ is the distance in between each peak. This leads to

$$D(\lambda) = \frac{1}{Lc}\left[\frac{1}{\Delta\lambda^2}\left(2\lambda\cdot\Delta\lambda - \lambda^2\frac{d\Delta\lambda}{d\lambda}\right)\right]. \tag{A.1.9}$$

Data treatment

The data treatment for the measured power spectrum is done in a few simple steps.

- Fit each peak to the peak of a sine function and record the peak position called λ_n.
- Determine $\Delta\lambda_p = \lambda_{n+1} - \lambda_n$ and $\lambda_p = (\lambda_{n+1} + \lambda_n)/2$.
- Fit the data points $(\lambda_p, \Delta\lambda_p)$ to a 3rd or 4th order polynomial.
- Use the determined $\Delta\lambda(\lambda)$ function to determine the dispersion.

A.2 Coupled Differential Equations for Soliton Self-Frequency Shift Model

The method (MoM) for deriving the coupled equations for the SSFS model is outlined in Sec. 3.3 and the derivation is here presented with more detail. The ansatz is chosen as

$$u(z,t) = \sqrt{P_0(z)}\mathrm{sech}\left(\frac{t - t_c(z)}{T_0(z)}\right)\exp\left[\mathrm{i}\Phi(z) - \mathrm{i}b(z)(t - t_c(z)) - \mathrm{i}\mu(z)(t - t_c(z))^2\right], \tag{A.2.1}$$

with the 5 required moments

$$Q(z) = \int |u(z,t)|^2 \mathrm{d}t, \tag{A.2.2a}$$

$$P_M(z) = \frac{1}{2} \int (u(z,t)\partial_t u^*(z,t) - u^*(z,t)\partial_t u(z,t))\mathrm{d}t, \tag{A.2.2b}$$

$$I_1(z) = \int t|u(z,t)|^2 \mathrm{d}t, \tag{A.2.2c}$$

$$I_2(z) = \int (t-t_c)^2 |u(z,t)|^2 \mathrm{d}t, \tag{A.2.2d}$$

$$I_3(z) = \int (t-t_c)(u^*(z,t)\partial_t u(z,t) - u(z,t)\partial_t u^*(z,t))\mathrm{d}t, \tag{A.2.2e}$$

and the GNLS

$$\begin{aligned}\partial_z u(z,t) = &-\frac{\alpha}{2}u(z,t) + \mathrm{i}\sum_{m\geq 2} \frac{\mathrm{i}^m \beta_m}{m!}\partial_t^m u(z,t) \\ &+ \mathrm{i}\sum_{n\geq 0} \frac{\mathrm{i}^n \gamma_n}{n!}\partial_t^n \left\{ u(z,t) \int R(t')|u(z,t-t')|^2 \mathrm{d}t' \right\}.\end{aligned} \tag{A.2.3}$$

In our model, only the first two dispersion terms, GVD and TOD, as well as the first two nonlinear terms, containing the Kerr nonlinearity, Raman scattering, self-steepening and TPA, is included. However, the first part of the derivation will include all terms.

Using the ansatz, the 5 moments can be evaluated as

$$Q = 2P_0T_0, \tag{A.2.4a}$$

$$P_M = i2bP_0T_0 = ibQ, \tag{A.2.4b}$$

$$I_1 = 2t_cP_0T_0 = t_cQ, \tag{A.2.4c}$$

$$I_2 = \frac{\pi^2}{6}P_0T_0^3 = \frac{\pi^2}{12}QT_0^2, \tag{A.2.4d}$$

$$I_3 = -i\frac{2\pi^2}{3}\mu P_0T_0^3 = -i4\mu I_2. \tag{A.2.4e}$$

By differentiating these 5 equations, we get a set of differential equations for the pulse parameters.

$$\partial_z b = -\frac{1}{2P_0T_0}\left(i\partial_z P_M + b\partial_z Q\right), \tag{A.2.5a}$$

$$\partial_z P_0 = \frac{3}{4T_0}\left(\partial_z Q - \frac{4}{\pi^2}\frac{1}{T_0^2}\partial_z I_2\right), \tag{A.2.5b}$$

$$\partial_z T_0 = \frac{1}{2P_0T_0^2}\left(\frac{6}{\pi^2}\partial_z I_2 - \frac{1}{2}T_0^2\partial_z Q\right), \tag{A.2.5c}$$

$$\partial_z \mu = \frac{3}{2\pi^2 P_0 T_0^3}\left(i\partial_z I_3 - 4\mu\partial_z I_2\right), \tag{A.2.5d}$$

$$\partial_z t_c = \frac{1}{2P_0T_0}\left(\partial_z I_1 - t_c\partial_z Q\right). \tag{A.2.5e}$$

These equations are all dependent on the derivatives of the moments.

In the derivation, these eight $A_n(x)$ functions,

$$A_1(x) = \frac{15}{8}\mathrm{csch}^4(x)\left[4x + 2x\cosh(2x) - 3\sinh(2x)\right] \tag{A.2.6a}$$

$$A_2(x) = 3x\,\mathrm{csch}^3(x)\left[x\cosh(x) - \sinh(x)\right] \tag{A.2.6b}$$

$$A_3(x) = \frac{1}{4}\mathrm{csch}^4(x)\left[-\left(2x^3+6x\right)\cosh(2x) + 9x^2\sinh(2x) - 4x^3 + 6x\right] \tag{A.2.6c}$$

$$A_4(x) = \frac{3}{\pi^2-9}x\,\mathrm{csch}^3(x)\left[\left(3x^3+\pi^2 x\right)\cosh(x) - \left(6x^2+\pi^2\right)\sinh(x)\right] \tag{A.2.6d}$$

$$\begin{aligned} A_5(x) = \frac{15}{8\pi^2+120}\mathrm{csch}^4(x)\Big[&\left(18x^2-3\pi^2\right)\sinh(2x) - \left(4x^3+12x-2\pi^2 x\right)\cosh(2x) \\ &-8x^3 + 12x + 4\pi^2 x\Big] \end{aligned} \tag{A.2.6e}$$

$$\begin{aligned} A_6(x) = \frac{1}{304}\mathrm{csch}^5(x)\Big[&\left(68\pi^2x^2 - 180x^2 + 75\pi^2 - 450\right)\cosh(3x) - \left(158\pi^2 x - 720x\right)\sinh(3x) \\ &+\left(412\pi^2x^2 - 2700x^2 - 75\pi^2 + 450\right)\cosh(x) - \left(306\pi^2 x - 2520x\right)\sinh(x)\Big] \end{aligned} \tag{A.2.6f}$$

$$\begin{aligned} A_7(x) = \frac{15}{8\pi^2-60}\mathrm{csch}^4(x)\Big[&16x^3 + 4\pi^2 x - 6x + \left(8x^3 + 2\pi^2 x + 6x\right)\cosh(2x) \\ &-\left(18x^2+3\pi^2\right)\sinh(2x)\Big] \end{aligned} \tag{A.2.6g}$$

$$A_8(x) = \frac{45}{152}\mathrm{csch}^5(x)\left[8x\sinh(3x) + 28x\sinh(x) - \left(2x^2+5\right)\cosh(3x) - \left(30x^2-5\right)\cosh(x)\right] \tag{A.2.6h}$$

which are normalized such that $A_n(x \to 0) = x$, and the seven $B_n(x)$ functions

$$B_1(x) = \frac{3}{2}\operatorname{csch}^4(x)\left[\left(6x^2-1\right)\cosh(2x) - 8x\sinh(2x) + 12x^2 + 1\right] \tag{A.2.7a}$$

$$B_2(x) = \frac{5}{12}\operatorname{csch}^5(x)\left[7\sinh(3x) + 27\sinh(x) - 3x\cosh(3x) - 45x\cosh(x)\right] \tag{A.2.7b}$$

$$B_3(x) = \frac{3}{\pi^2-6}\operatorname{csch}^3(x)\left[\left(4x^3+\pi^2 x\right)\cosh(x) - \left(6x^2+\pi^2\right)\sinh(x)\right] \tag{A.2.7c}$$

$$\begin{aligned}B_4(x) = \frac{1}{36}\operatorname{csch}^5(x)&\left[\left(18x^2+61\right)\sinh(3x) + \left(54x^2+297\right)\sinh(x)\right.\\ &\left.-48x\cosh(3x) - 432x\cosh(x)\right]\end{aligned} \tag{A.2.7d}$$

$$B_5(x) = \operatorname{csch}^3(x)\left[3x^2\sinh(x) - 2x^3\cosh(x)\right] \tag{A.2.7e}$$

$$B_6(x) = \frac{3}{\pi^2+3}\operatorname{csch}^3(x)\left[\left(3x^2-\pi^2\right)\sinh(x) - \left(2x^3-\pi^2 x\right)\cosh(x)\right] \tag{A.2.7f}$$

$$B_7(x) = \frac{3}{2}\operatorname{csch}^4(x)\left[4x\sinh(2x) - \left(2x^2+1\right)\cosh(2x) - 4x^2 + 1\right], \tag{A.2.7g}$$

normalized such that $B_n(x \to 0) = 1$, are needed to derive the final set of differential equations.

The derivative of Q can be found by differentiating Eq. (A.2.2a) and inserting Eq. (A.2.3). With that we have

$$\begin{aligned}\partial_z Q &= \int u^*\partial_z u + u\partial_z u^* \mathrm{d}t\\ &= 2\Re\int u^*\partial_z u\,\mathrm{d}t\\ &= 2\Re\int u^*\left[-\frac{\alpha}{2}u + \mathrm{i}\sum_{m\geq 2}\frac{\mathrm{i}^m\beta_m}{m!}\partial_t^m u + \mathrm{i}\sum_{n\geq 0}\frac{\mathrm{i}^n\gamma_n}{n!}\partial_t^n\left\{u\int R(t')|u(t-t')|^2\mathrm{d}t'\right\}\right]\mathrm{d}t\\ &= -\alpha Q + \sum_{m\geq 2}\Re\left[2\frac{\mathrm{i}^{m+1}\beta_m}{m!}\int u^*\partial_t^m u\ \mathrm{d}t\right]\\ &\quad+\sum_{n\geq 0}\Re\left[2\frac{\mathrm{i}^{n+1}\gamma_n}{n!}\int u^*\partial_t^n\left\{u\int R(t')|u(t-t')|^2\mathrm{d}t'\right\}\mathrm{d}t\right].\end{aligned} \tag{A.2.8}$$

As the pulse is bounded in time, it shows that

$$\Re\left[\mathrm{i}^{m+1}\int u^*\partial_t^m u\ \mathrm{d}t\right] = 0, \tag{A.2.9}$$

and with only the first two nonlinear terms are included, we get

$$\begin{aligned}\partial_z Q = {}& -\alpha Q + \Re\left[\mathrm{i}\gamma_0\right] \int |u|^2 \int R(t')|u(t-t')|^2 \mathrm{d}t'\, \mathrm{d}t \\ & - \Re\left[\gamma_1 \int u^* \partial_t \left\{ u \int R(t')|u(t-t')|^2 \mathrm{d}t' \right\} \mathrm{d}t \right]. \end{aligned} \tag{A.2.10}$$

In this the ansatz is inserted. All integrals in t can be analytically solved, getting

$$\begin{aligned}\partial_z Q = & -2\alpha P_0 T_0 - \frac{16}{15} f_R \gamma_1^r P_0^2 \int h_R(t) A_1\left(\frac{t}{T_0}\right) \mathrm{d}t - \frac{8}{3} f_R \mu \gamma_1^i P_0^2 T_0^2 \int h_R(t) A_2\left(\frac{t}{T_0}\right) \mathrm{d}t \\ & - \frac{8}{3}(\gamma_0^i + b\gamma_1^i) P_0^2 T_0 \left[1 - f_R + f_R \int h_R(t) f_1\left(\frac{t}{T_0}\right) \mathrm{d}t\right], \end{aligned} \tag{A.2.11}$$

where

$$\begin{aligned} f_1(x) &= \frac{1}{\pi^2}\left[\left(\pi^2 - 3\right) B_3(x) + 3B_5(x)\right] \\ &= \frac{1}{3\pi^2}\left[\left(\pi^2 - 6\right) B_3(x) + \left(2\pi^2 + 6\right) B_6(x)\right] \end{aligned}$$

Similarly it is done for the other derivatives,

$$\begin{aligned} \partial_z P_M &= \frac{1}{2} \int \left[(\partial_z u)(\partial_t u^*) + u(\partial_t \partial_z u^*) - (\partial_z u^*)(\partial_t u) - u^*(\partial_t \partial_z u)\right] \mathrm{d}t, \\ &= \mathrm{i}2\Im \int (\partial_z u)(\partial_t u^*) \mathrm{d}t, \end{aligned} \tag{A.2.12}$$

where, in the rewriting, it has been used that u goes to zero at infinity. Inserting the GNLS

$$\begin{aligned} \partial_z P_M &= \mathrm{i}2\Im \int \partial_t u^* \left[-\frac{\alpha}{2} u + \mathrm{i} \sum_{m\geq 2} \frac{\mathrm{i}^m \beta_m}{m!} \partial_t^m u + \mathrm{i} \sum_{n \geq 0} \frac{\mathrm{i}^n \gamma_n}{n!} \partial_t^n \left\{ u \int R(t')|u(t-t')|^2 \mathrm{d}t' \right\} \right] \mathrm{d}t \\ &= -\mathrm{i}\alpha \Im \int u(\partial_t u^*) \mathrm{d}t + \mathrm{i} \sum_{m\geq 2} \Im \left[2 \frac{\mathrm{i}^{m+1}\beta_m}{m!} \int (\partial_t u^*)(\partial_t^m u) \mathrm{d}t \right] \\ &\quad + \mathrm{i} \sum_{n\geq 0} \Im \left[2 \frac{\mathrm{i}^{n+1}\gamma_n}{n!} \int (\partial_t u^*) \partial_t^n \left\{ u \int R(t')|u(t-t')|^2 \mathrm{d}t' \right\} \right] \mathrm{d}t \\ &= -\mathrm{i}\alpha \int \Im\left[u \partial_t u^*\right] \mathrm{d}t + \sum_{n\geq 0} \mathrm{i}\Im \left[2 \frac{\mathrm{i}^{n+1}\gamma_n}{n!} \int (\partial_t u^*) \partial_t^n \left\{ u \int R(t')|u(t-t')|^2 \mathrm{d}t' \right\} \mathrm{d}t \right], \end{aligned} \tag{A.2.13}$$

where it has been used, similar to Eq. (A.2.9), that

$$\Im \left[\mathrm{i}^{m+1} \int (\partial_t u^*)(\partial_t^m u) \mathrm{d}t \right] = 0. \tag{A.2.14}$$

$$
\begin{aligned}
\partial_z P_M = -\mathrm{i}\alpha \int \Im\left[u \partial_t u^*\right] \mathrm{d}t + \mathrm{i}\Im\left[\mathrm{i}2\gamma_0 \int (\partial_t u^*) u \int R(t') |u(t-t')|^2 \mathrm{d}t' \mathrm{d}t\right] \\
- \mathrm{i}\Im\left[2\gamma_1 \int (\partial_t u^*) \partial_t \left\{ u \int R(t') |u(t-t')|^2 \mathrm{d}t' \right\} \mathrm{d}t\right],
\end{aligned}
\tag{A.2.15}
$$

With the ansatz inserted it results in

$$
\begin{aligned}
\partial_z P_M = &- \mathrm{i}2b\alpha P_0 T_0 + \mathrm{i}\frac{8}{3}\mu\gamma_1^r P_0^2 T_0 \left[1 - f_R + f_R \int h_R(t) B_1\left(\frac{t}{T_0}\right) \mathrm{d}t\right] \\
&- \mathrm{i}\frac{16}{15} f_R(\gamma_0^r + b\gamma_1^r) P_0^2 \int h_R(t) A_1\left(\frac{t}{T_0}\right) \mathrm{d}t - \mathrm{i}\frac{16}{15} f_R b\gamma_1^r P_0^2 \int h_R(t) A_1\left(\frac{t}{T_0}\right) \mathrm{d}t \\
&- \mathrm{i}\frac{8}{3} b(\gamma_0^i + b\gamma_1^i) P_0^2 T_0 \left[1 - f_R + f_R \int h_R(t) f_1\left(\frac{t}{T_0}\right) \mathrm{d}t\right] \\
&- \mathrm{i}\frac{8}{3} f_R \mu(\gamma_0^i + b\gamma_1^i) P_0^2 T_0^2 \int h_R(t) A_2\left(\frac{t}{T_0}\right) \mathrm{d}t \\
&- \mathrm{i}\frac{8}{3} f_R b\mu\gamma_1^i P_0^2 T_0^2 \int h_R(t) A_2\left(\frac{t}{T_0}\right) \mathrm{d}t \\
&- \mathrm{i}\frac{8}{5}\frac{\gamma_1^i P_0^2}{T_0} \left[1 - f_R + f_R \int h_R(t) B_2\left(\frac{t}{T_0}\right) \mathrm{d}t\right] \\
&- \mathrm{i}8\left(\frac{\pi^2}{9} - \frac{2}{3}\right) \mu^2 \gamma_1^i P_0^2 T_0^3 \left[1 - f_R + f_R \int h_R(t) B_3\left(\frac{t}{T_0}\right) \mathrm{d}t\right].
\end{aligned}
\tag{A.2.16}
$$

Similarly for I_1,

$$
\begin{aligned}
\partial_z I_1 &= \int t\left[u^*(\partial_z u) + u(\partial_z u^*)\right] \mathrm{d}t \\
&= t_c \int \left[u^*(\partial_z u) + u(\partial_z u^*)\right] \mathrm{d}t + T_0 \int \frac{t - t_c}{T_0}\left[u^*(\partial_z u) + u(\partial_z u^*)\right] \mathrm{d}t \\
&= t_c \partial_z Q + 2T_0 \Re \int \frac{t - t_c}{T_0} u^* \partial_z u \ \mathrm{d}t
\end{aligned}
\tag{A.2.17}
$$

which can also be written as

$$
\begin{aligned}
&\partial_z I_1 - t_c \partial_z Q \\
&\quad = 2T_0 \Re \int \frac{t-t_c}{T_0} u^* \left[-\frac{\alpha}{2} u + \mathrm{i} \sum_{m \geq 2} \frac{\mathrm{i}^m \beta_m}{m!} \partial_t^m u + \mathrm{i} \sum_{n \geq 0} \frac{\mathrm{i}^n \gamma_n}{n!} \partial_t^n \left\{ u \int R(t') |u(t-t')|^2 \mathrm{d}t' \right\} \right] \mathrm{d}t \\
&\quad = \sum_{m \geq 2} \frac{2\beta_m T_0}{m!} \int \frac{t-t_c}{T_0} \Re \left[\mathrm{i}^{m+1} u^* \partial_t^m u \right] \mathrm{d}t \\
&\qquad + \sum_{n \geq 0} \frac{2T_0}{n!} \int \frac{t-t_c}{T_0} \Re \left[\mathrm{i}^{n+1} \gamma_n u^* \partial_t^n \left\{ u \int R(t') |u(t-t')|^2 \mathrm{d}t' \right\} \right] \mathrm{d}t, \\
&\quad = -\beta_2 T_0 \int \frac{t-t_c}{T_0} \Re \left[\mathrm{i} u^* \partial_t^2 u \right] \mathrm{d}t + \frac{1}{3} \beta_3 T_0 \int \frac{t-t_c}{T_0} \Re \left[u^* \partial_t^3 u \right] \mathrm{d}t \\
&\qquad + 2T_0 \int \frac{t-t_c}{T_0} \Re \left[\mathrm{i} \gamma_0 \right] |u|^2 \int R(t') |u(t-t')|^2 \mathrm{d}t' \mathrm{d}t, \\
&\qquad - 2T_0 \int \frac{t-t_c}{T_0} \Re \left[\gamma_1 u^* \partial_t \left\{ u \int R(t') |u(t-t')|^2 \mathrm{d}t' \right\} \right] \mathrm{d}t, \qquad \text{(A.2.18)}
\end{aligned}
$$

where the loss term disappears since it is an odd function, and ultimately

$$
\begin{aligned}
\partial_z I_1 - t_c \partial_z Q = & 2b(\beta_2 + b\beta_3) P_0 T_0 + \beta_3 P_0 T_0 \left[\frac{\pi^2}{3} \mu^2 T_0^2 + \frac{1}{3T_0^2} - b^2 \right] \\
& + 2\gamma_1^r P_0^2 T_0 \left[1 - f_R + f_R \int h_R(t) B_4 \left(\frac{t}{T_0} \right) \mathrm{d}t \right] \\
& - \frac{4}{3} f_R (\gamma_0^i + b\gamma_1^i) P_0^2 T_0^2 \int h_R(t) A_2 \left(\frac{t}{T_0} \right) \mathrm{d}t \\
& - 4 \left(\frac{\pi^2}{9} - \frac{2}{3} \right) \mu \gamma_1^i P_0^2 T_0^3 \left[1 - f_R + f_R \int h_R(t) B_3 \left(\frac{t}{T_0} \right) \mathrm{d}t \right].
\end{aligned}
\tag{A.2.19}
$$

For I_2 we get

$$
\begin{aligned}
\partial_z I_2 &= \int (t-t_c)^2 (u^*\partial_z u + u\partial_z u^*)\mathrm{d}t - 2(\partial_z t_c)\int (t-t_c)|u|^2\mathrm{d}t \\
&= \Re\left[2T_0^2 \int \left(\frac{t-t_c}{T_0}\right)^2 u^*\partial_z u \ \mathrm{d}t\right] \\
&= \Re\left[2T_0^2 \int \left(\frac{t-t_c}{T_0}\right)^2 u^* \left[-\frac{\alpha}{2}u + \mathrm{i}\sum_{m\geq 2}\frac{\mathrm{i}^m\beta_m}{m!}\partial_t^m u\right.\right. \\
&\quad \left.\left. + \ \mathrm{i}\sum_{n\geq 0}\frac{\mathrm{i}^n\gamma_n}{n!}\partial_t^n\left\{u\int R(t')|u(t-t')|^2\mathrm{d}t'\right\}\right]\mathrm{d}t\right] \\
&= -\alpha T_0^2\int\left(\frac{t-t_c}{T_0}\right)^2|u|^2\mathrm{d}t + \sum_{m\geq 2}\frac{2T_0^2\beta_m}{m!}\int\left(\frac{t-t_c}{T_0}\right)^2\Re\left[\mathrm{i}^{m+1}u^*\partial_t^m u\right]\mathrm{d}t \\
&\quad + \sum_{n\geq 0}\frac{2T_0^2}{n!}\int\left(\frac{t-t_c}{T_0}\right)^2\Re\left[\mathrm{i}^{n+1}\gamma_n u^*\partial_t^n\left\{u\int R(t')|u(t-t')|^2\mathrm{d}t'\right\}\right]\mathrm{d}t \\
&= -\alpha T_0^2\int\left(\frac{t-t_c}{T_0}\right)^2|u|^2\mathrm{d}t - T_0^2\beta_2\int\left(\frac{t-t_c}{T_0}\right)^2\Re\left[\mathrm{i}u^*\partial_t^2 u\right]\mathrm{d}t \\
&\quad + \frac{1}{3}T_0^2\beta_3\int\left(\frac{t-t_c}{T_0}\right)^2\Re\left[u^*\partial_t^3 u\right]\mathrm{d}t \\
&\quad + 2T_0^2\int\left(\frac{t-t_c}{T_0}\right)^2\Re\left[\mathrm{i}\gamma_0\right]|u|^2\int R(t')|u(t-t')|^2\mathrm{d}t'\mathrm{d}t \\
&\quad - 2T_0^2\int\left(\frac{t-t_c}{T_0}\right)^2\Re\left[\gamma_1 u^*\partial_t\left\{u\int R(t')|u(t-t')|^2\mathrm{d}t'\right\}\right]\mathrm{d}t. \qquad \text{(A.2.20)}
\end{aligned}
$$

$$
\begin{aligned}
\partial_z I_2 = &-\frac{\pi^2}{6}\alpha P_0 T_0^3 + \frac{2\pi^2}{3}\mu P_0 T_0^3(\beta_2 + b\beta_3) \\
&+ 2\left(\frac{4}{3} - \frac{2\pi^2}{45}\right) f_R\gamma_1^r P_0^2 T_0^2 \int h_R(t) f_2\left(\frac{t}{T_0}\right)\mathrm{d}t \\
&- 2\left(\frac{\pi^2}{9} - \frac{2}{3}\right)(\gamma_0^i + b\gamma_1^i)P_0^2T_0^3\left[1 - f_R + f_R\int h_R(t)B_3\left(\frac{t}{T_0}\right)\mathrm{d}t\right] \\
&- 4\left(\frac{\pi^2}{6} - 1\right) f_R\mu\gamma_1^i P_0^2 T_0^4 \int h_R(t) f_3\left(\frac{t}{T_0}\right)\mathrm{d}t, \qquad \text{(A.2.21)}
\end{aligned}
$$

where

$$
\begin{aligned}
f_2(x) &= \frac{1}{30-\pi^2}\left[30A_3(x) - \pi^2 A_1(x)\right] \\
&= \frac{1}{30-\pi^2}\left[\left(30+2\pi^2\right)A_5(x) - 3\pi^2 A_1(x)\right] \\
f_3(x) &= \frac{1}{\pi^2-6}\left[\pi^2 A_2(x) - 6A_6(x)\right] \\
&= \frac{1}{3\pi^2-18}\left[\left(2\pi^2-18\right)A_4(x) + \pi^2 A_2(x)\right], \qquad \text{(A.2.22)}
\end{aligned}
$$

and finally for I_3,

$$
\begin{aligned}
\partial_z I_3 = &-\partial_z t_c \int (u^*\partial_t u - u\partial_t u^*)\mathrm{d}t \\
&- \int (t-t_c)\left[(\partial_z u)(\partial_t u^*) + u(\partial_t\partial_z u^*) - (\partial_z u^*)(\partial_t u) - u^*(\partial_t\partial_z u)\right]\mathrm{d}t \\
= &\,2P\partial_z t_c - \mathrm{i}\Im\left[4T_0\int \frac{t-t_c}{T_0}(\partial_t u^*)(\partial_z u)\mathrm{d}t\right] - \mathrm{i}\Im\left[2\int u^*\partial_z u\mathrm{d}t\right] \\
= &\,2P\partial_z t_c - \mathrm{i}\Im\left[4T_0\int \frac{t-t_c}{T_0}(\partial_t u^*)\left[-\frac{\alpha}{2}u + \mathrm{i}\sum_{m\geq 2}\frac{\mathrm{i}^m\beta_m}{m!}\partial_t^m u\right.\right. \\
&\qquad \left.\left. + \mathrm{i}\sum_{n\geq 0}\frac{\mathrm{i}^n\gamma_n}{n!}\partial_t^n\left\{u\int R(t')|u(t-t')|^2\mathrm{d}t'\right\}\right]\mathrm{d}t\right] \\
&- \mathrm{i}\Im\left[2\int u^*\left[-\frac{\alpha}{2}u + \mathrm{i}\sum_{m\geq 2}\frac{\mathrm{i}^m\beta_m}{m!}\partial_t^m u\right.\right. \\
&\qquad \left.\left. + \mathrm{i}\sum_{n\geq 0}\frac{\mathrm{i}^n\gamma_n}{n!}\partial_t^n\left\{u\int R(t')|u(t-t')|^2\mathrm{d}t'\right\}\right]\mathrm{d}t\right] \\
= &\,2P\partial_z t_c + \mathrm{i}2\alpha T_0\int \frac{t-t_c}{T_0}\Im\left[(\partial_t u^*)u\right]\mathrm{d}t \\
&+ \sum_{m\geq 2} -\mathrm{i}\frac{2\beta_m}{m!}\int \Re\left[\mathrm{i}^m 2T_0\frac{t-t_c}{T_0}(\partial_t u^*)\partial_t^m u + \mathrm{i}^m u^*\partial_t^m u\right]\mathrm{d}t \\
&+ \sum_{n\geq 0} -\mathrm{i}\frac{2}{n!}\int \Re\left[\left(\mathrm{i}^n 2\gamma_n T_0\frac{t-t_c}{T_0}\partial_t u^* + \mathrm{i}^n\gamma_n u^*\right)\partial_t^n\left\{u\int R(t')|u(t-t')|^2\mathrm{d}t'\right\}\right]\mathrm{d}t
\end{aligned}
$$

(A.2.23)

$$
\begin{aligned}
\partial_z I_3 = {} & 2P\partial_z t_c + \mathrm{i}2\alpha T_0 \int \frac{t-t_c}{T_0} \Im\left[(\partial_t u^*)u\right] \mathrm{d}t \\
& + \mathrm{i}\beta_2 \int \Re\left[2T_0 \frac{t-t_c}{T_0}(\partial_t u^*)\partial_t^2 u + u^*\partial_t^2 u\right] \mathrm{d}t \\
& + \mathrm{i}\frac{\beta_3}{3} \int \Re\left[\mathrm{i}2T_0 \frac{t-t_c}{T_0}(\partial_t u^*)\partial_t^3 u + \mathrm{i}u^*\partial_t^3 u\right] \mathrm{d}t \\
& - \mathrm{i}2 \int \Re\left[\left(2\gamma_0 T_0 \frac{t-t_c}{T_0}\left(\partial_t u^*\right) u + \gamma_0 |u|^2\right) \int R(t')|u(t-t')|^2 \mathrm{d}t'\right] \mathrm{d}t \\
& - \mathrm{i}2 \int \Re\left[\mathrm{i}\left(2\gamma_1 T_0 \frac{t-t_c}{T_0}\partial_t u^* + \gamma_1 u^*\right) \partial_t \left\{u \int R(t')|u(t-t')|^2 \mathrm{d}t'\right\}\right] \mathrm{d}t,
\end{aligned}
\tag{A.2.24}
$$

resulting in

$$
\begin{aligned}
\partial_z I_3 = {} & \mathrm{i}\frac{2\pi^2}{3}\alpha\mu P_0 T_0^3 - \mathrm{i}\frac{4}{3}\pi^2\mu^2(\beta_2 + b\beta_3)P_0 T_0^3 - \mathrm{i}\frac{4}{3}\frac{(\beta_2 + b\beta_3)P_0}{T_0} \\
& - \mathrm{i}\frac{4}{3}(\gamma_0^r + b\gamma_1^r)P_0^2 T_0 \left[1 - f_R + f_R \int h_R(t) B_7\left(\frac{t}{T_0}\right) \mathrm{d}t\right] \\
& - \mathrm{i}\frac{8}{45} f_R \mu \gamma_1^r P_0^2 T_0^2 \int h_R(t) \left[\left(60 - 2\pi^2\right) f_2\left(\frac{t}{T_0}\right) - \left(2\pi^2 - 15\right) A_7\left(\frac{t}{T_0}\right)\right] \mathrm{d}t \\
& + \mathrm{i}\frac{152}{45} f_R \gamma_1^i P_0^2 \int h_R(t) A_8\left(\frac{t}{T_0}\right) \mathrm{d}t \\
& + \mathrm{i}8\left(\frac{\pi^2}{9} - \frac{2}{3}\right)\mu(\gamma_0^i + b\gamma_1^i)P_0^2 T_0^3 \left[1 - f_R + f_R \int h_R(t) B_3\left(\frac{t}{T_0}\right) \mathrm{d}t\right] \\
& + \mathrm{i}16\left(\frac{\pi^2}{6} - 1\right) f_R \mu^2 \gamma_1^i P_0^2 T_0^4 \int h_R(t) f_3\left(\frac{t}{T_0}\right) \mathrm{d}t.
\end{aligned}
\tag{A.2.25}
$$

With the derivative of the moments, the five coupled differential equations become

$$
\begin{aligned}
\partial_z b = {} & -\frac{8}{15}\frac{(\gamma_0^r + b\gamma_1^r)P_0}{T_0} f_R \int h_R(t) A_1\left(\frac{t}{T_0}\right) \mathrm{d}t \\
& + \frac{4}{3}\mu\gamma_1^r P_0 \left[1 - f_R + f_R \int h_R(t) B_1\left(\frac{t}{T_0}\right) \mathrm{d}t\right] \\
& - \frac{4}{3}\mu(\gamma_0^i + b\gamma_1^i)P_0 T_0 f_R \int h_R(t) A_2\left(\frac{t}{T_0}\right) \mathrm{d}t \\
& - \frac{4}{5}\frac{\gamma_1^i P_0}{T_0^2}\left[1 - f_R + f_R \int h_R(t) B_2\left(\frac{t}{T_0}\right) \mathrm{d}t\right] \\
& - 4\left(\frac{\pi^2}{9} - \frac{2}{3}\right)\mu^2\gamma_1^i P_0 T_0^2 \left[1 - f_R + f_R \int h_R(t) B_3\left(\frac{t}{T_0}\right) \mathrm{d}t\right]
\end{aligned}
\tag{A.2.26a}
$$

$$\begin{aligned}\partial_z t_c = {} & b(\beta_2 + b\beta_3) + \frac{1}{2}\beta_3\left[\frac{\pi^2}{3}\mu^2 T_0^2 + \frac{1}{3T_0^2} - b^2\right] \\ & + \gamma_1^r P_0\left[1 - f_R + f_R\int h_R(t) B_4\left(\frac{t}{T_0}\right)\mathrm{d}t\right] \\ & - \frac{2}{3}(\gamma_0^i + b\gamma_1^i)P_0 T_0 f_R\int h_R(t) A_2\left(\frac{t}{T_0}\right)\mathrm{d}t \\ & - 2\left(\frac{\pi^2}{9} - \frac{2}{3}\right)\mu\gamma_1^i P_0 T_0^2\left[1 - f_R + f_R\int h_R(t) B_3\left(\frac{t}{T_0}\right)\mathrm{d}t\right]\end{aligned} \tag{A.2.26b}$$

$$\begin{aligned}\partial_z T_0 = {} & 2\mu T_0(\beta_2 + b\beta_3) + \frac{8}{\pi^2}\gamma_1^r P_0 f_R\int h_R(t) A_3\left(\frac{t}{T_0}\right)\mathrm{d}t \\ & + \frac{4}{\pi^2}(\gamma_0^i + b\gamma_1^i)P_0 T_0\left[1 - f_R + f_R\int h_R(t) B_5\left(\frac{t}{T_0}\right)\mathrm{d}t\right] \\ & - \left(\frac{4}{3} - \frac{12}{\pi^2}\right)\mu\gamma_1^i P_0 T_0^2 f_R\int h_R(t) A_4\left(\frac{t}{T_0}\right)\mathrm{d}t\end{aligned} \tag{A.2.26c}$$

$$\begin{aligned}\partial_z P_0 = {} & -\alpha P_0 - 2\mu P_0(\beta_2 + b\beta_3) - \left(\frac{8}{\pi^2} + \frac{8}{15}\right)\frac{\gamma_1^r P_0^2}{T_0} f_R\int h_R(t) A_5\left(\frac{t}{T_0}\right)\mathrm{d}t \\ & - \left(\frac{4}{3} + \frac{4}{\pi^2}\right)(\gamma_0^i + b\gamma_1^i)P_0^2\left[1 - f_R + f_R\int h_R(t) B_6\left(\frac{t}{T_0}\right)\mathrm{d}t\right] \\ & - \frac{12}{\pi^2}\mu\gamma_1^i P_0^2 T_0 f_R\int h_R(t) A_6\left(\frac{t}{T_0}\right)\mathrm{d}t\end{aligned} \tag{A.2.26d}$$

$$\begin{aligned}\partial_z \mu = {} & (\beta_2 + b\beta_3)\left(\frac{2}{\pi^2}\frac{1}{T_0^4} - 2\mu^2\right) + \frac{2}{\pi^2}\frac{(\gamma_0^r + b\gamma_1^r)P_0}{T_0^2}\left[1 - f_R + f_R\int h_R(t) B_7\left(\frac{t}{T_0}\right)\mathrm{d}t\right] \\ & - \left(\frac{8}{15} - \frac{4}{\pi^2}\right)\frac{\mu\gamma_1^r P_0}{T_0} f_R\int h_R(t) A_7\left(\frac{t}{T_0}\right)\mathrm{d}t - \frac{76}{15\pi^2}\frac{\gamma_1^i P_0}{T_0^3} f_R\int h_R(t) A_8\left(\frac{t}{T_0}\right)\mathrm{d}t.\end{aligned} \tag{A.2.26e}$$

Appendix B

THZ-TDS Measurement Data

B.1 Picometrix

B.1.1 $Ge_{11}As_{22}Se_{67}$

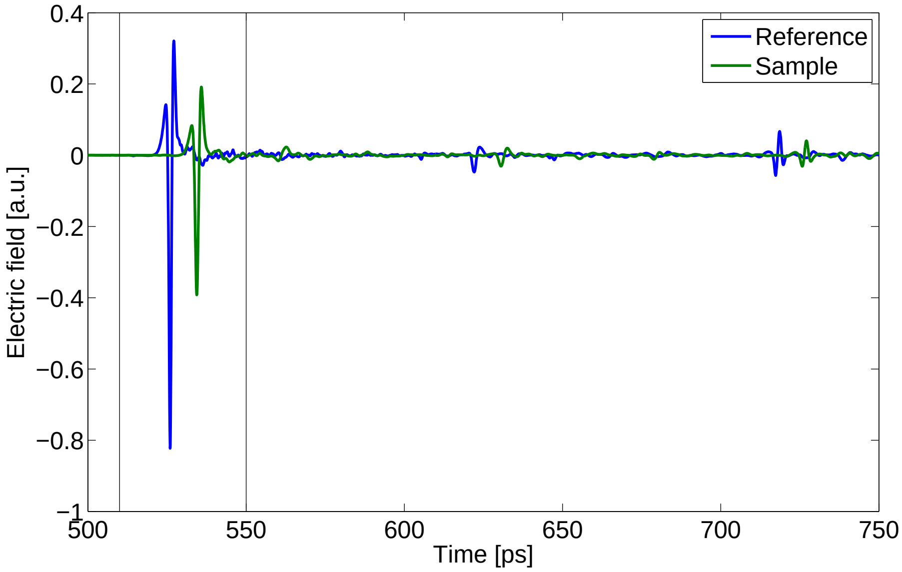

Figure B.1:

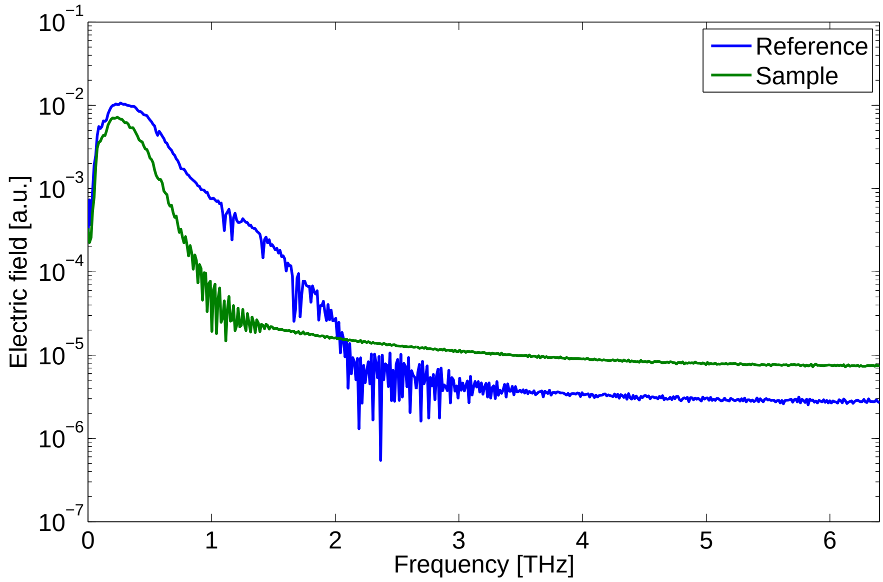

Figure B.2:

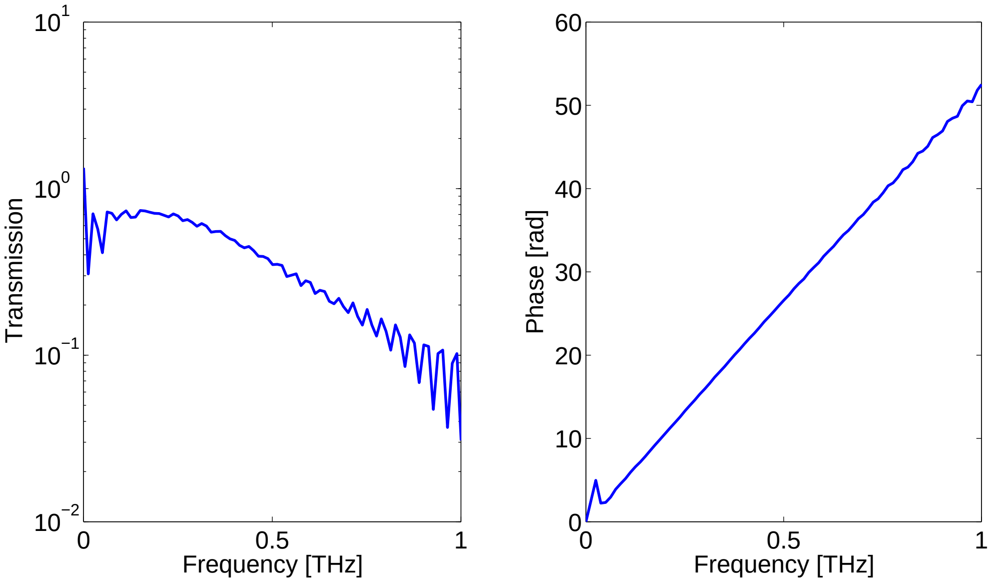

Figure B.3:

B.1.2 $Ge_{15}As_{20}Se_{65}$

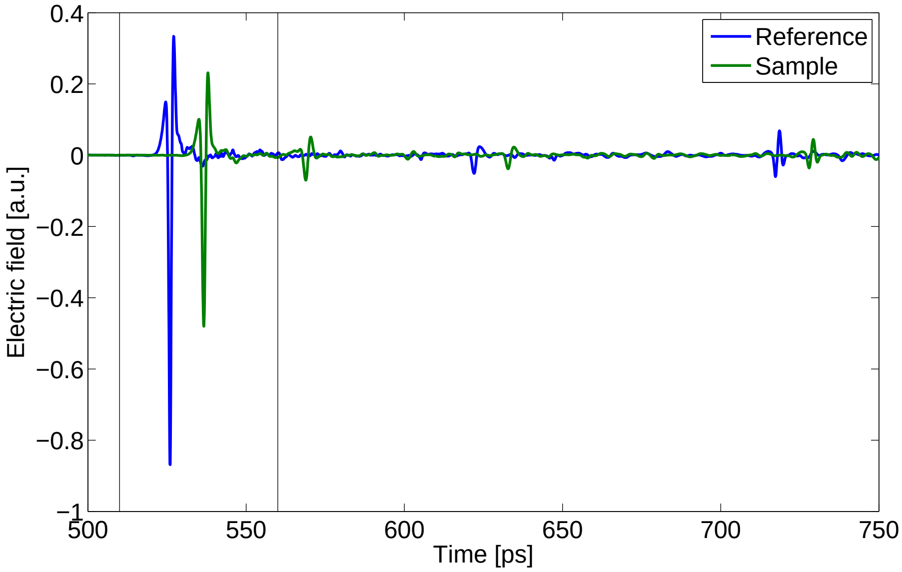

Figure B.4:

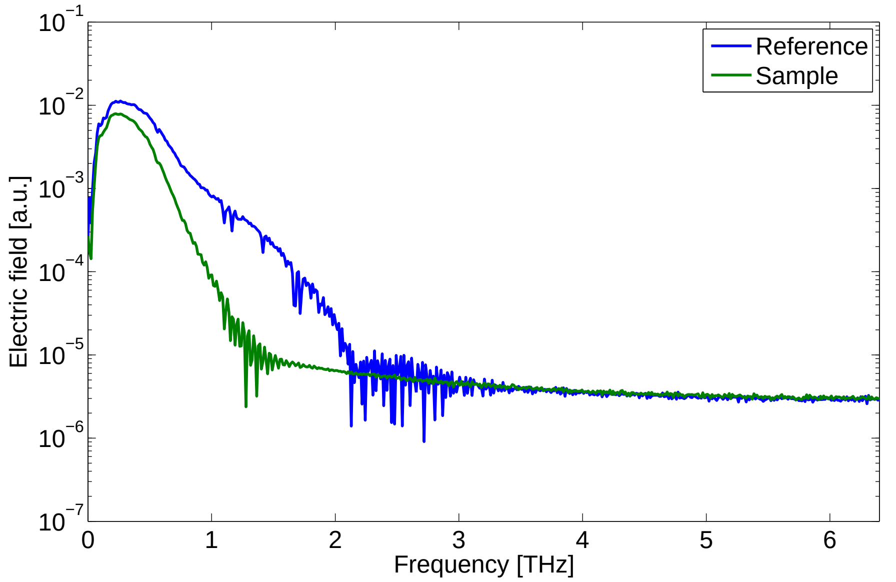

Figure B.5:

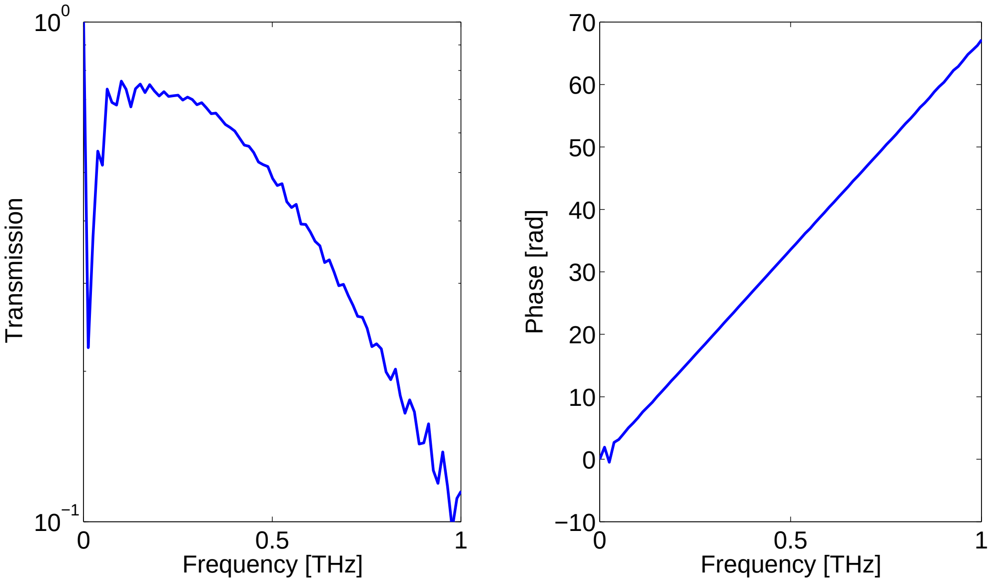
Transmission
10^0
10^{-1}
0
0.5
1
Frequency [THz]
Phase [rad]
70
60
50
40
30
20
10
0
−10
0
0.5
1
Frequency [THz]

Figure B.6:

B.1.3 $Ge_{15}As_{25}Se_{60}$

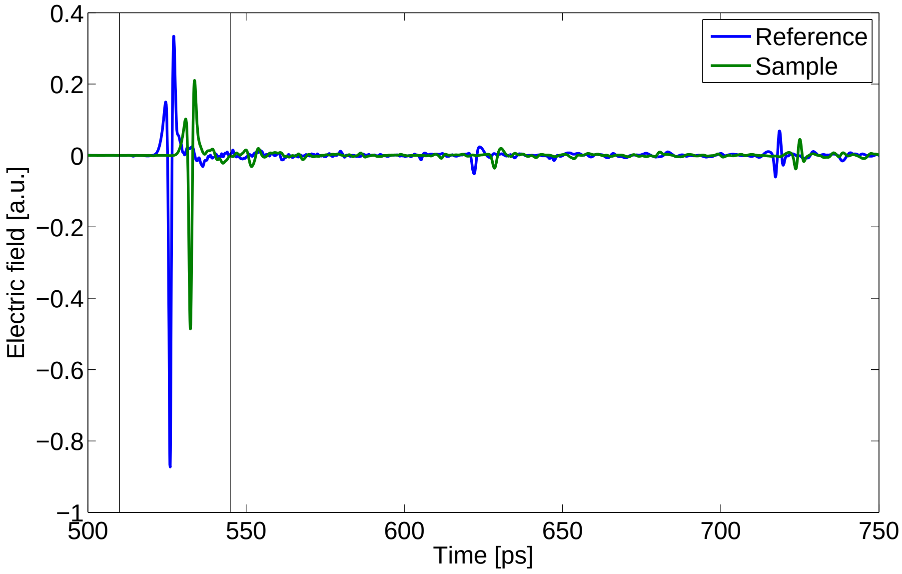

Figure B.7:

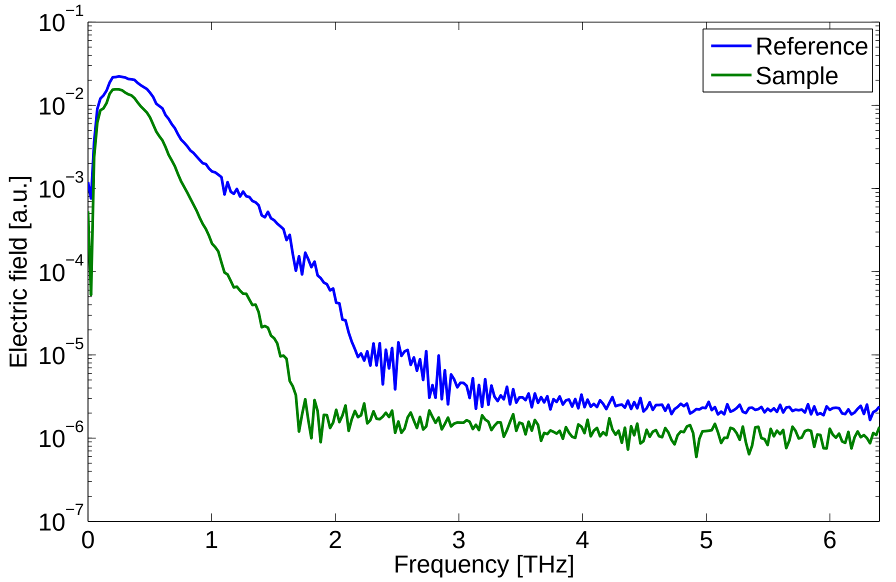

Figure B.8:

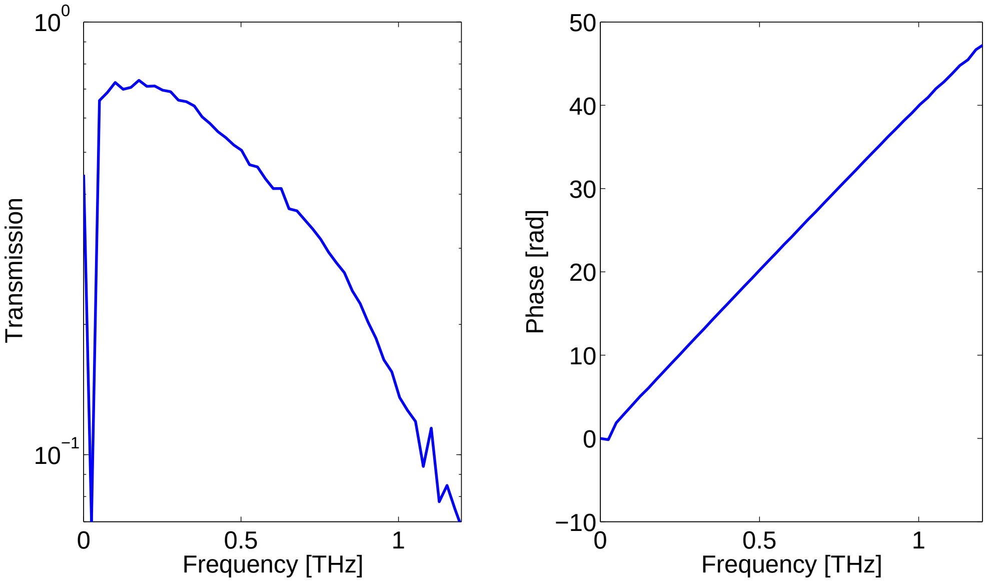

10^0
10^{-1}
Transmission
0
0.5
1
Frequency [THz]
50
40
30
20
10
0
−10
Phase [rad]
0
0.5
1
Frequency [THz]

Figure B.9:

B.1.4 $Ge_{33}As_{12}Se_{55}$

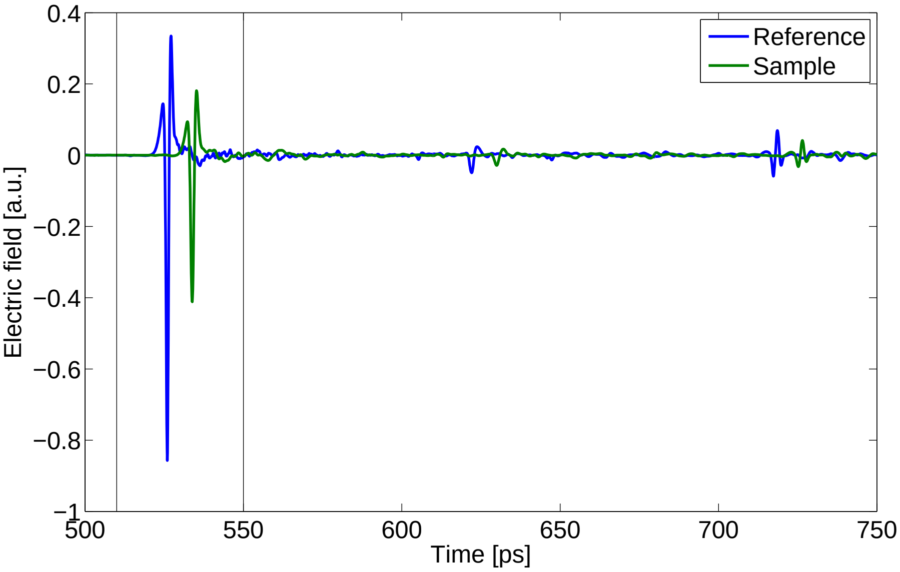

Figure B.10:

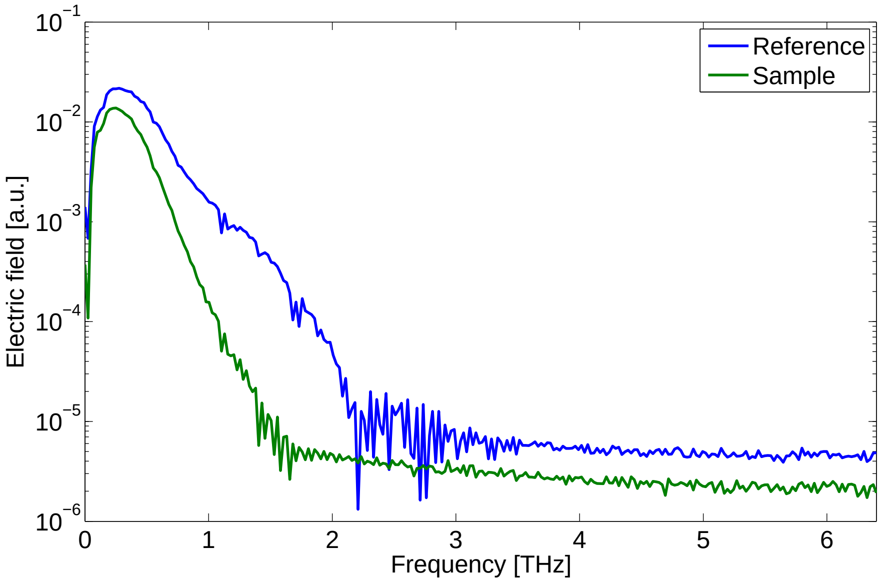

Figure B.11:

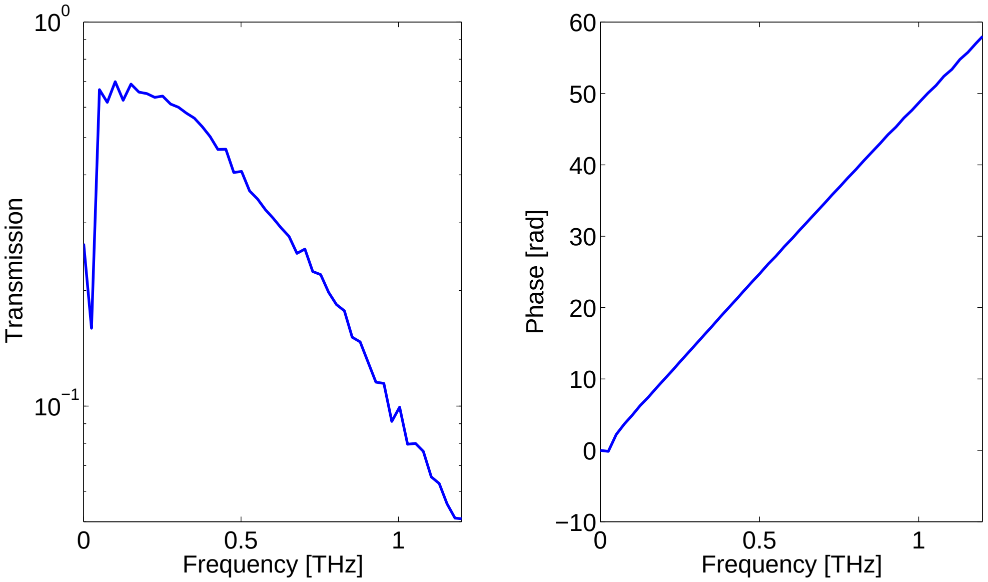
10^0
10^{-1}
Transmission
0
0.5
1
Frequency [THz]
60
50
40
30
20
10
0
−10
Phase [rad]
0
0.5
1
Frequency [THz]

Figure B.12:

B.2 ABCD Reflection

B.2.1 $Ge_{11}As_{22}Se_{67}$

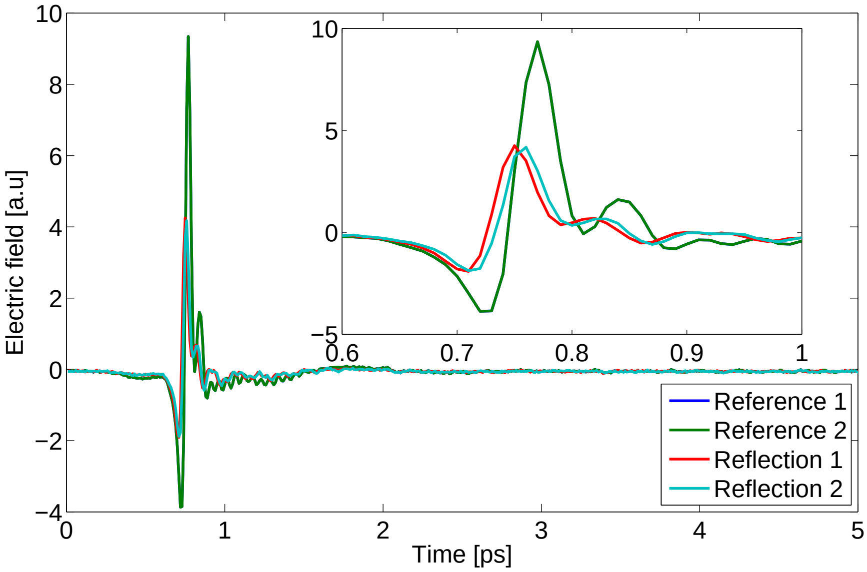

Figure B.13: Measured electric field.

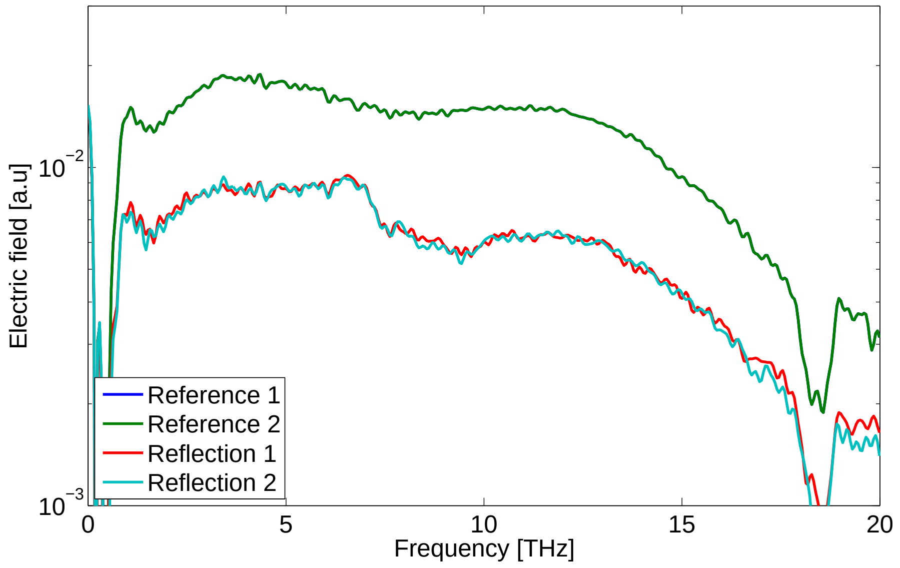

Figure B.14:

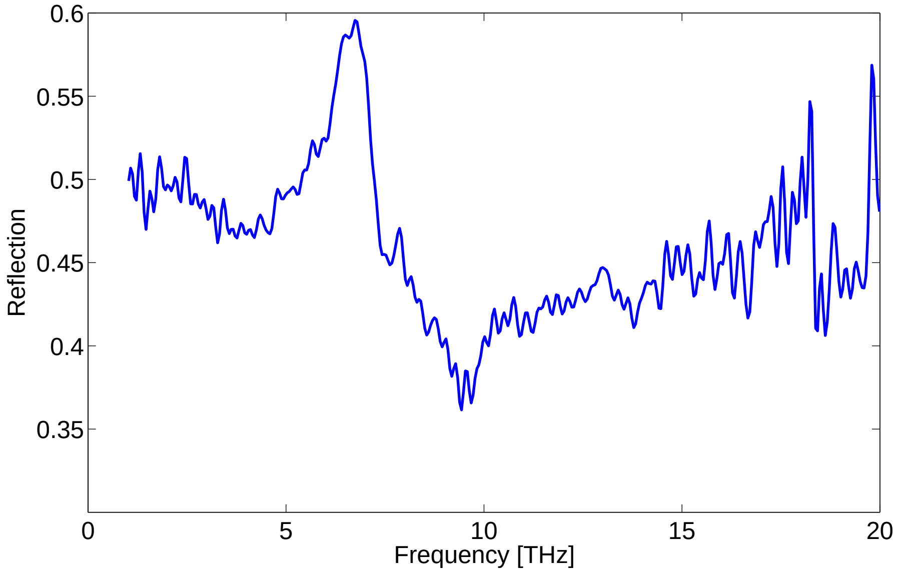

Figure B.15:

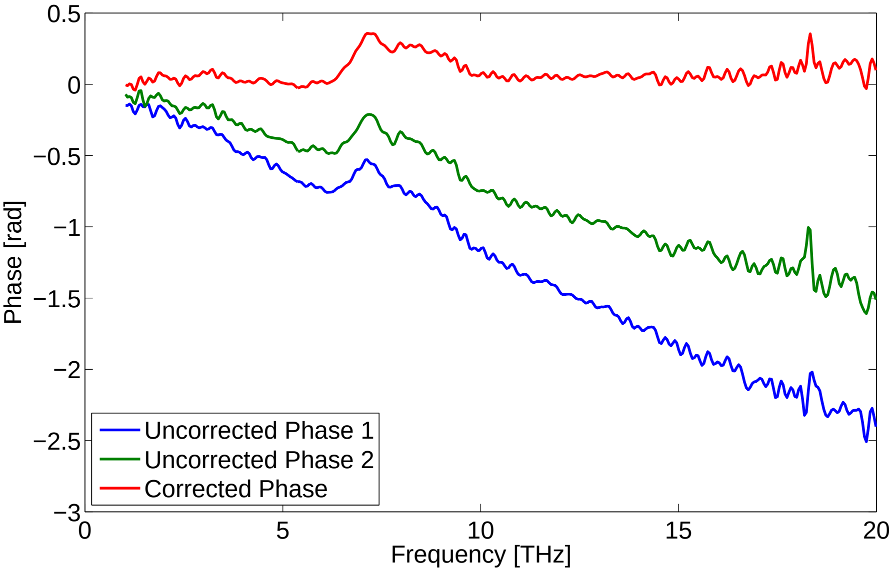

Figure B.16: The samples have been shifted 3.13 and 1.75 μm respectively.

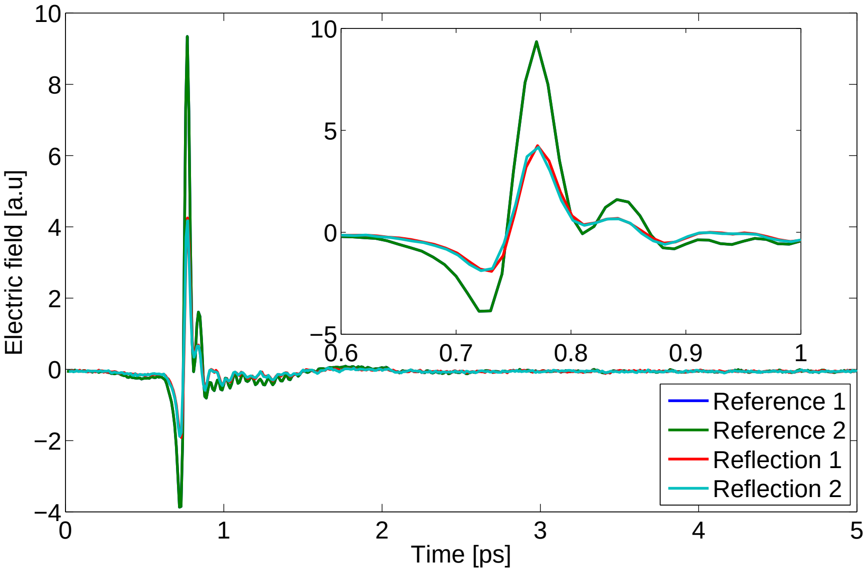

Figure B.17: Corrected electric field

B.2.2 $Ge_{15}As_{20}Se_{65}$

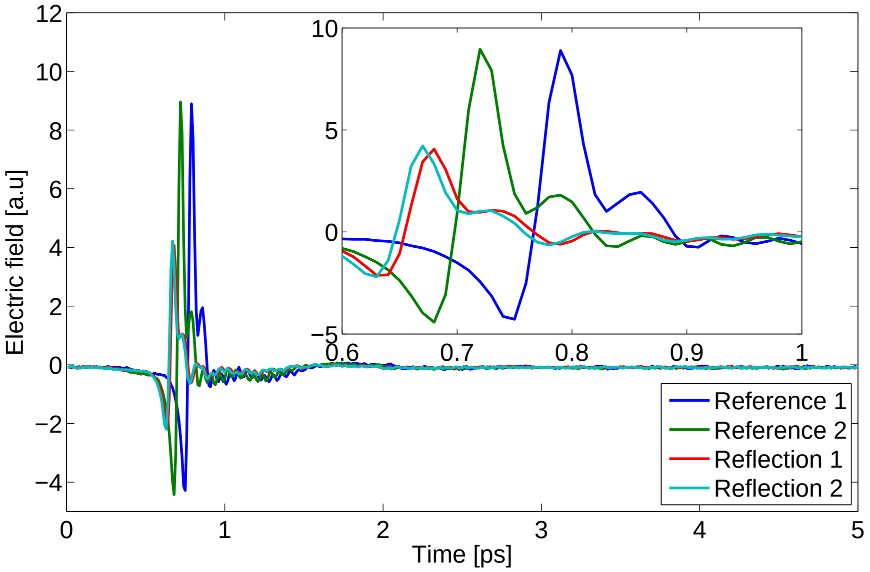

Figure B.18: Measured electric field.

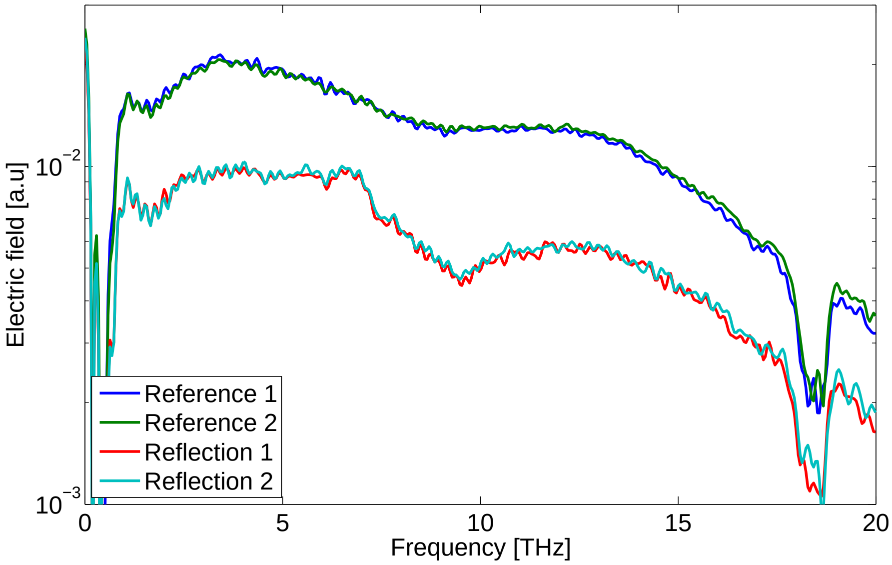

Figure B.19:

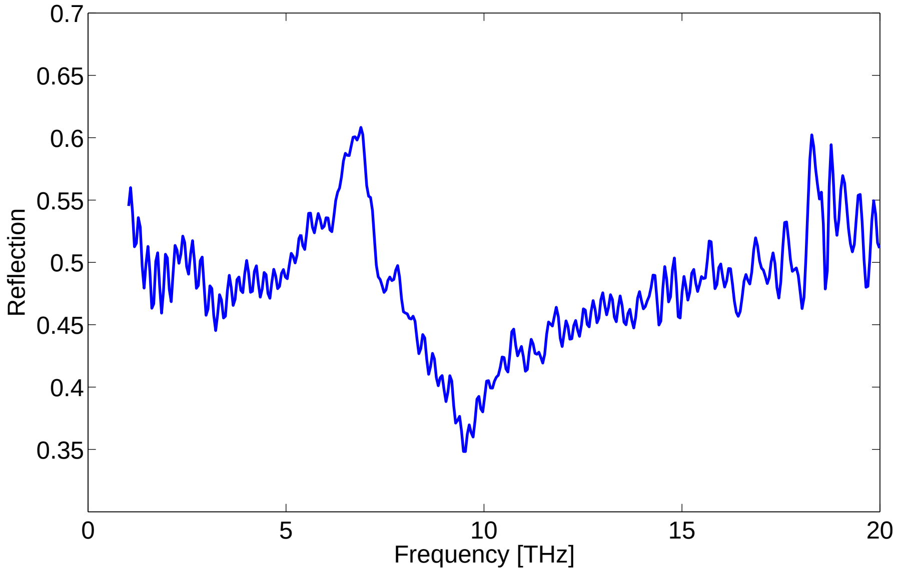

Figure B.20:

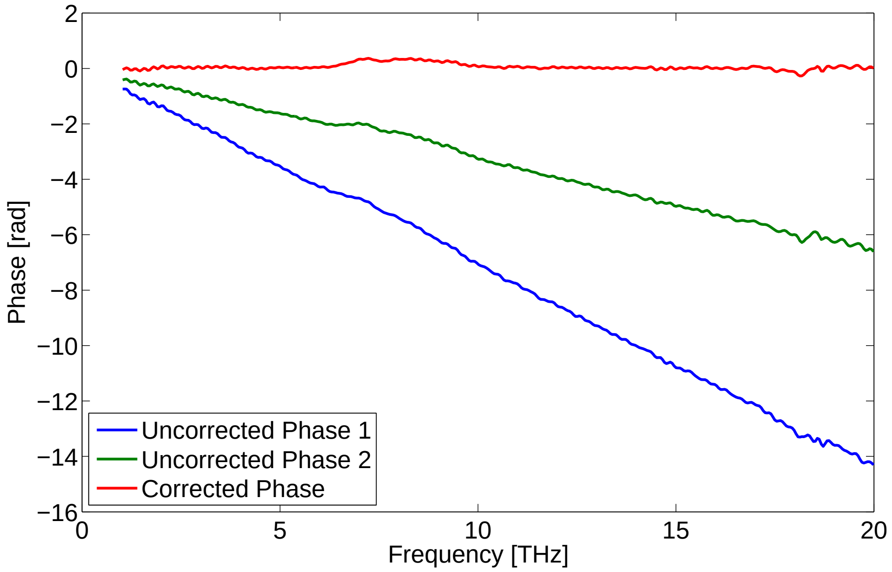

Figure B.21: The samples have been shifted 17.20 and 7.79 μm respectively.

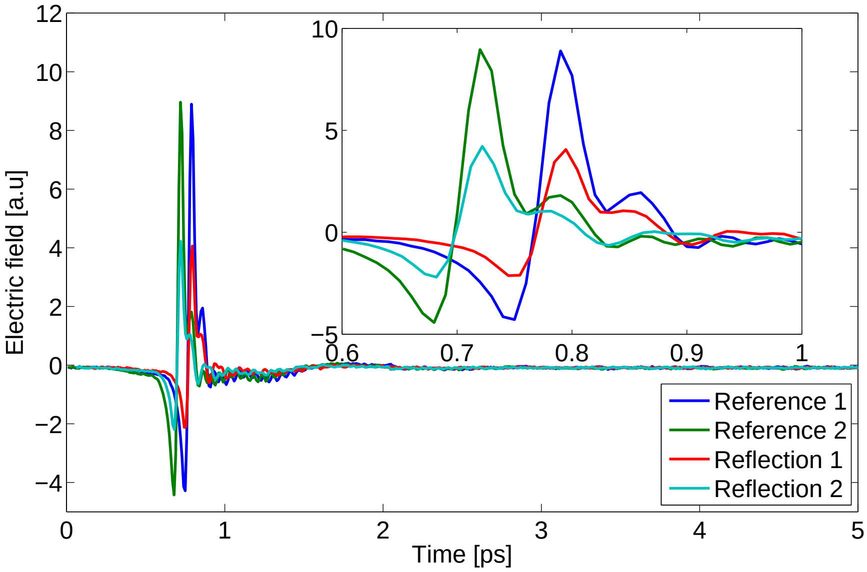

Figure B.22: Corrected electric field

B.2.3 $Ge_{15}As_{25}Se_{60}$

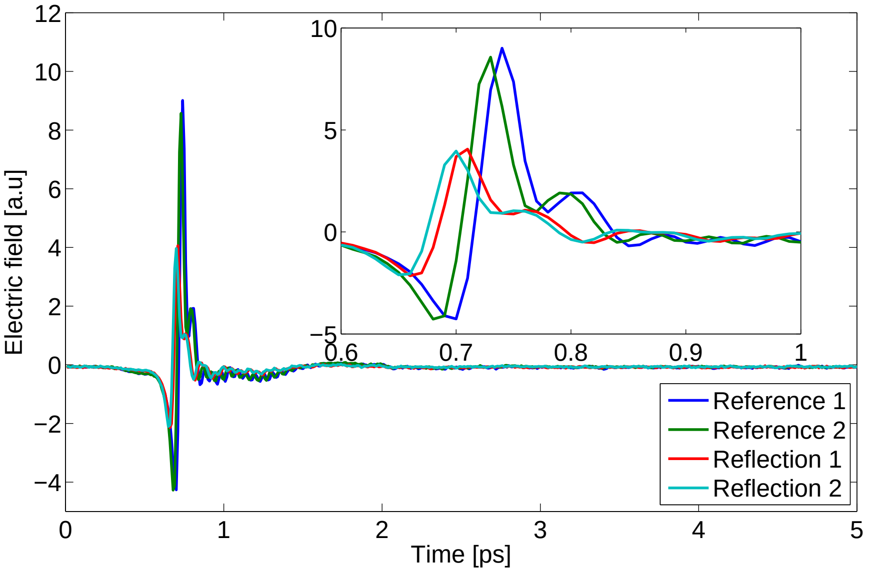

Figure B.23: Measured electric field.

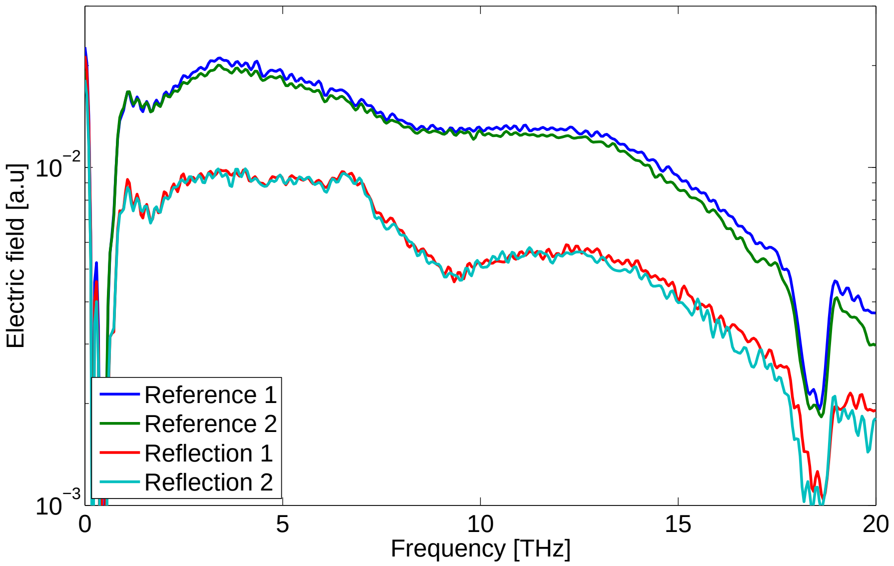

Figure B.24:

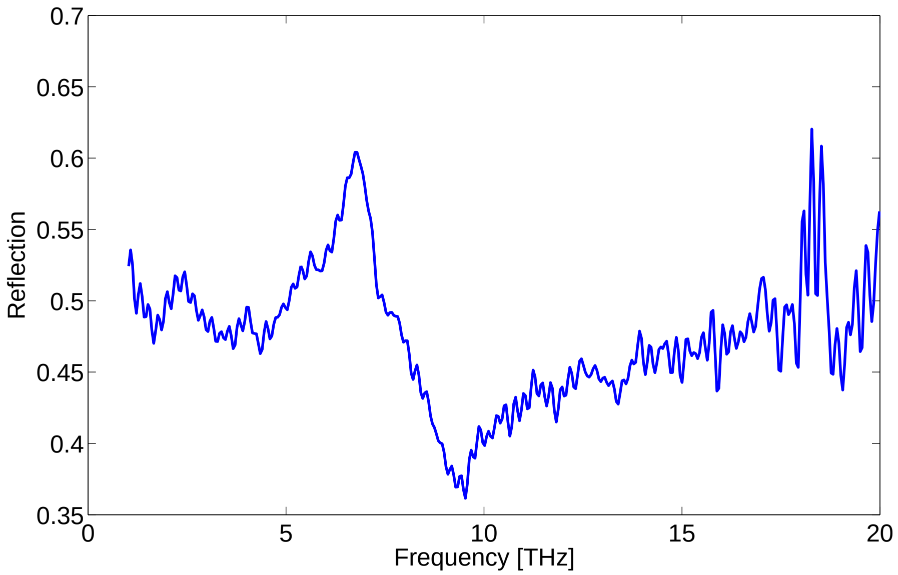

Figure B.25:

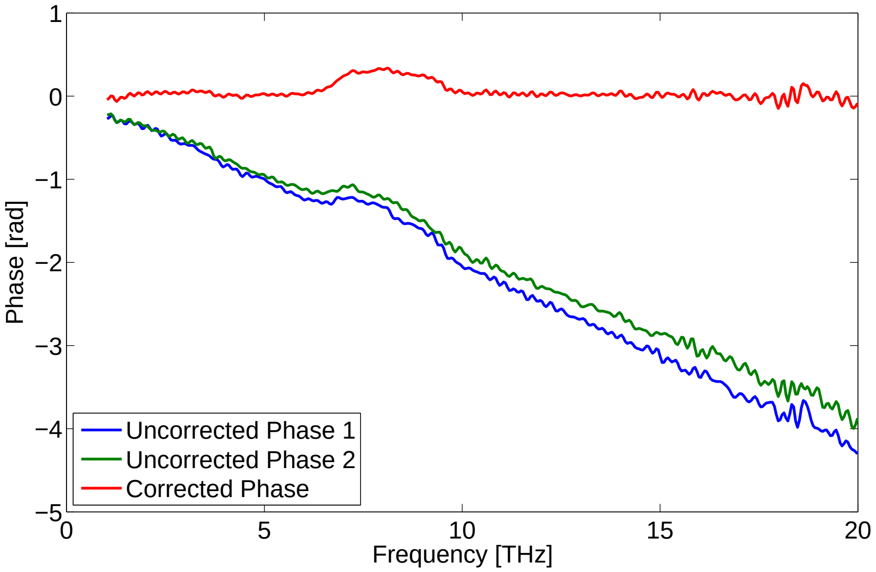

Figure B.26: The samples have been shifted 5.10 and 4.47 μm respectively.

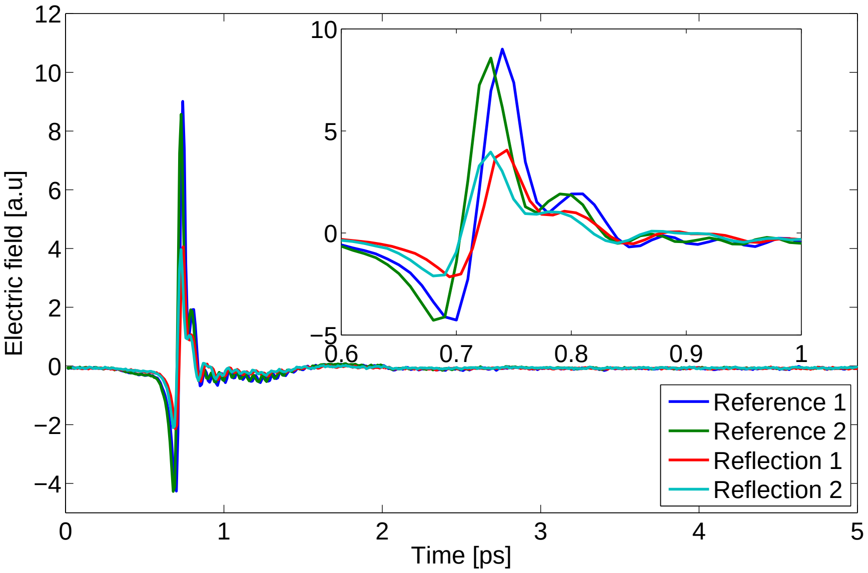

Figure B.27: Corrected electric field

B.3 ABCD Transmission

B.3.1 $Ge_{11}As_{22}Se_{67}$

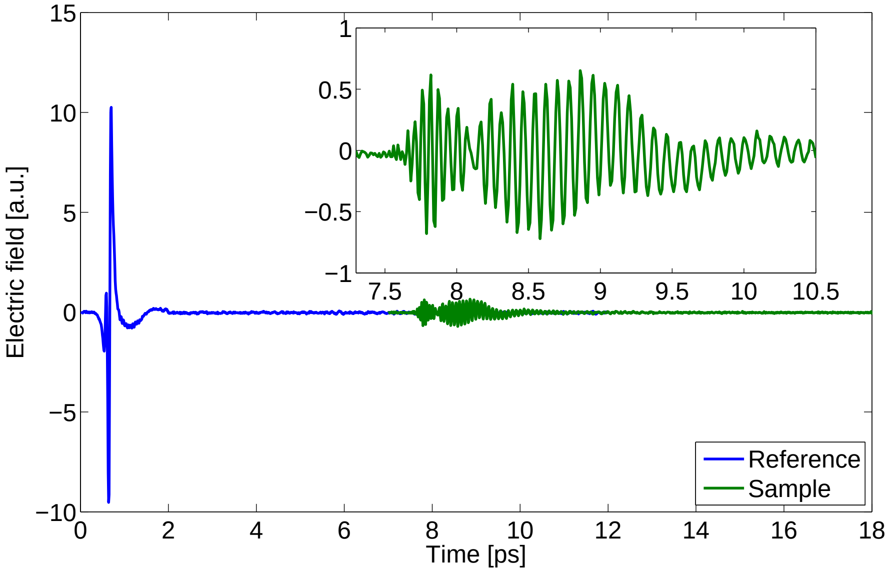

Figure B.28:

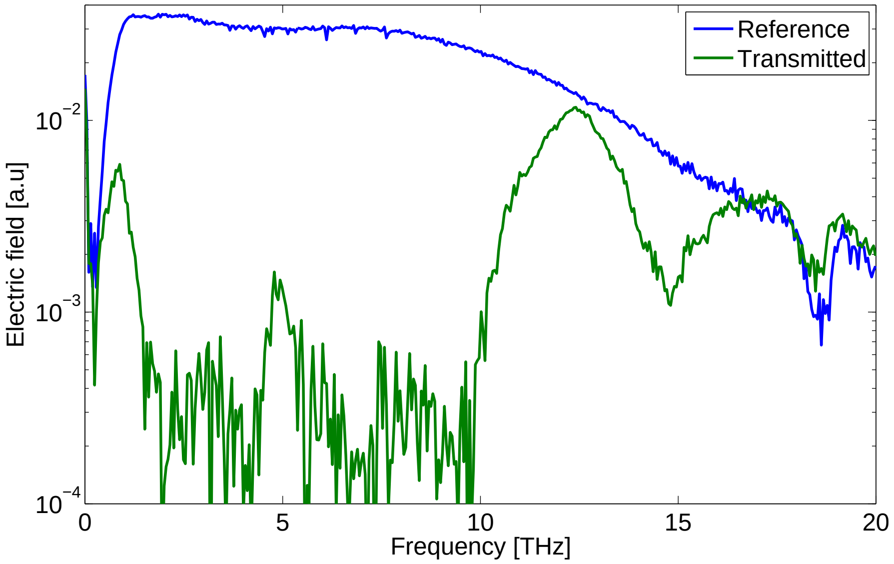

Figure B.29:

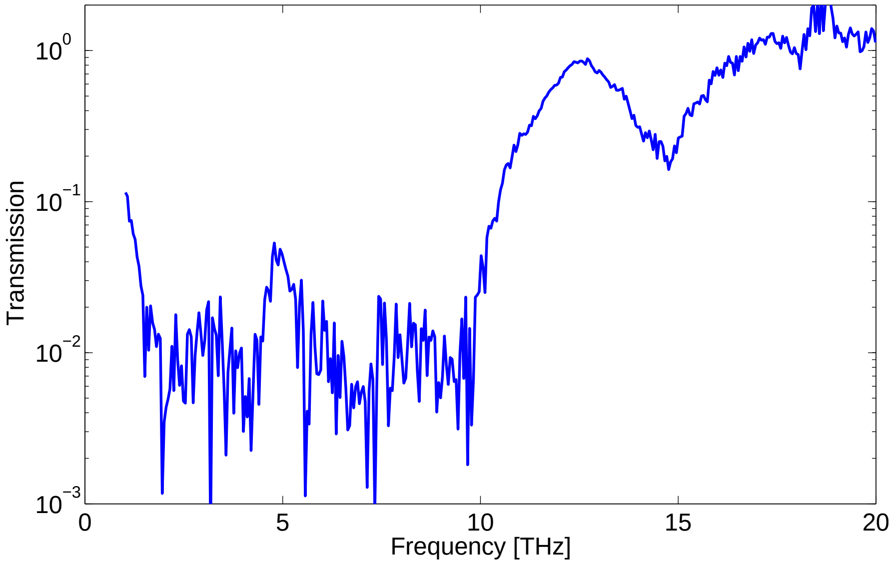

Figure B.30:

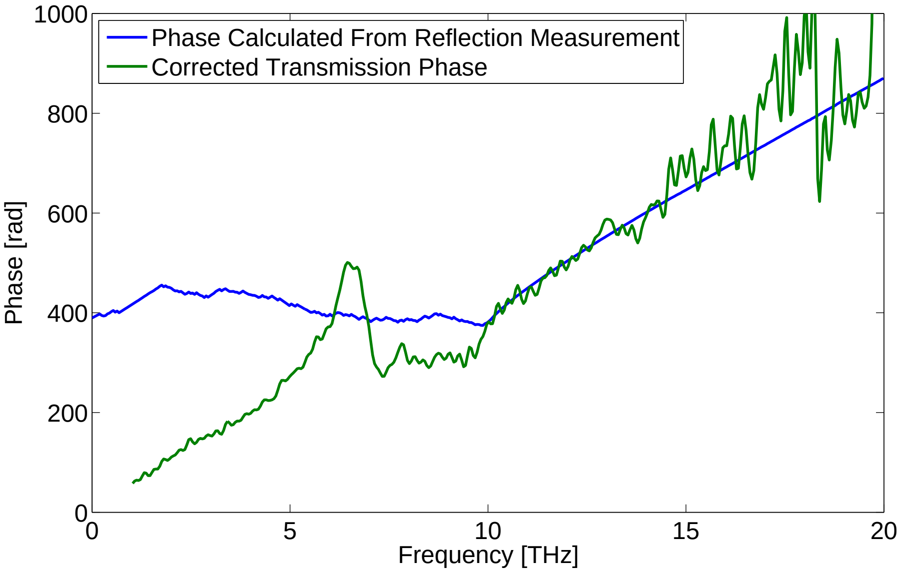
Phase Calculated From Reflection Measurement
Corrected Transmission Phase
Phase [rad]
Frequency [THz]
0
200
400
600
800
1000
0
5
10
15
20

Figure B.31:

B.3.2 $Ge_{15}As_{20}Se_{65}$

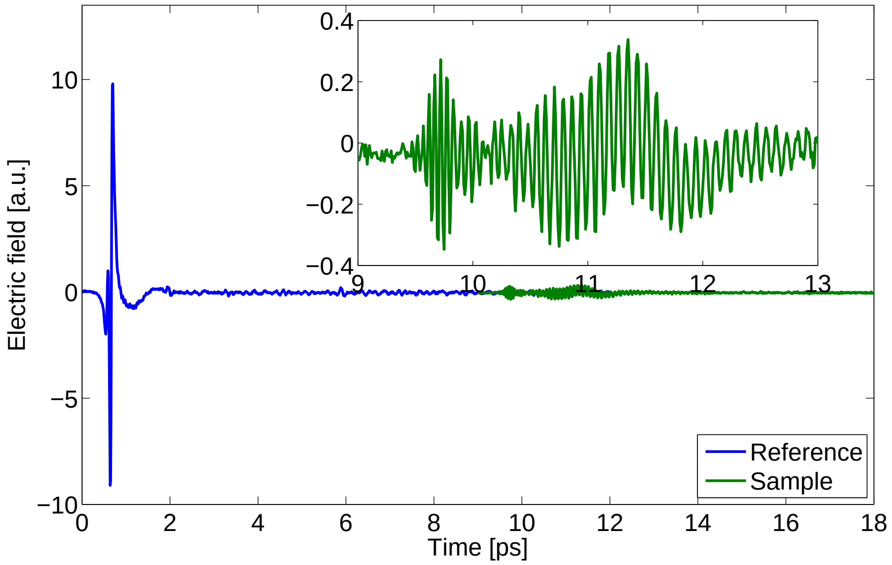

Figure B.32:

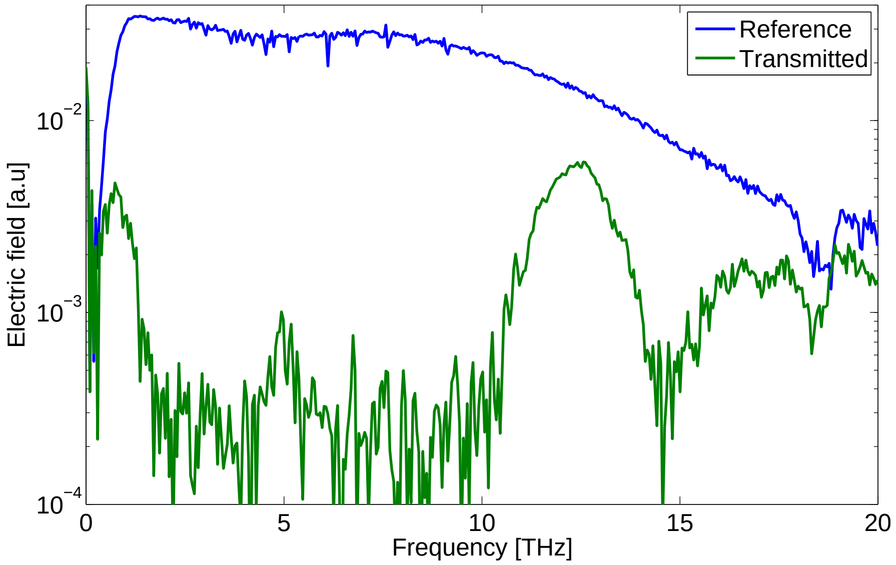

Figure B.33:

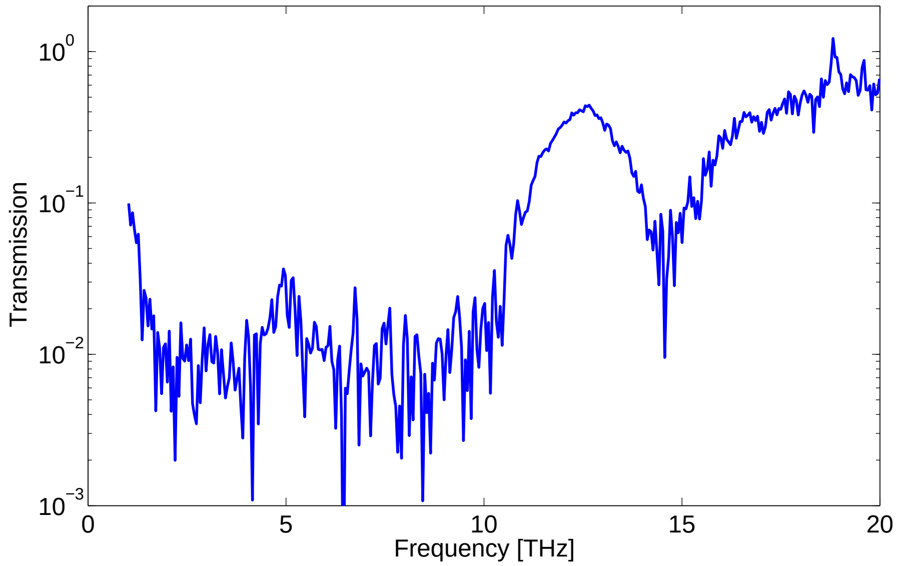

Figure B.34:

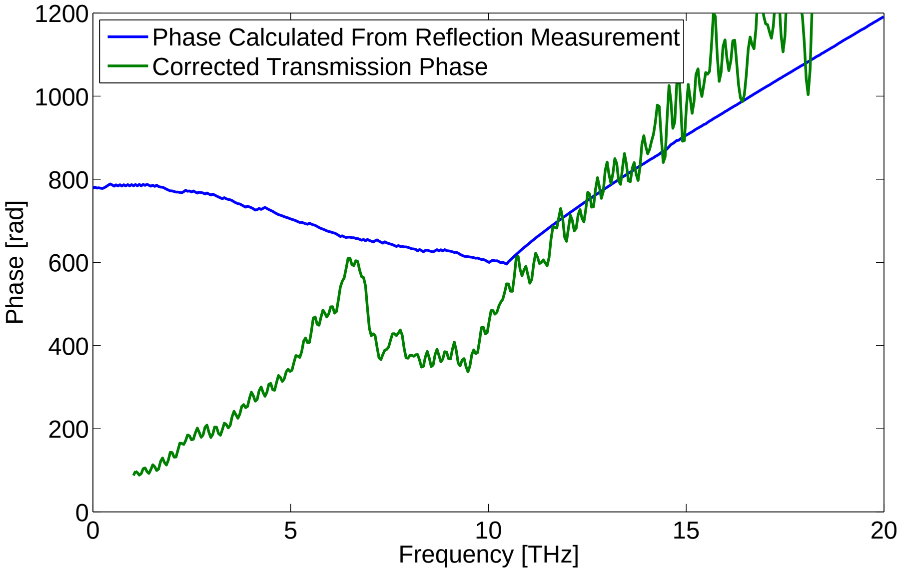

Figure B.35:

B.3.3 $Ge_{15}As_{25}Se_{60}$

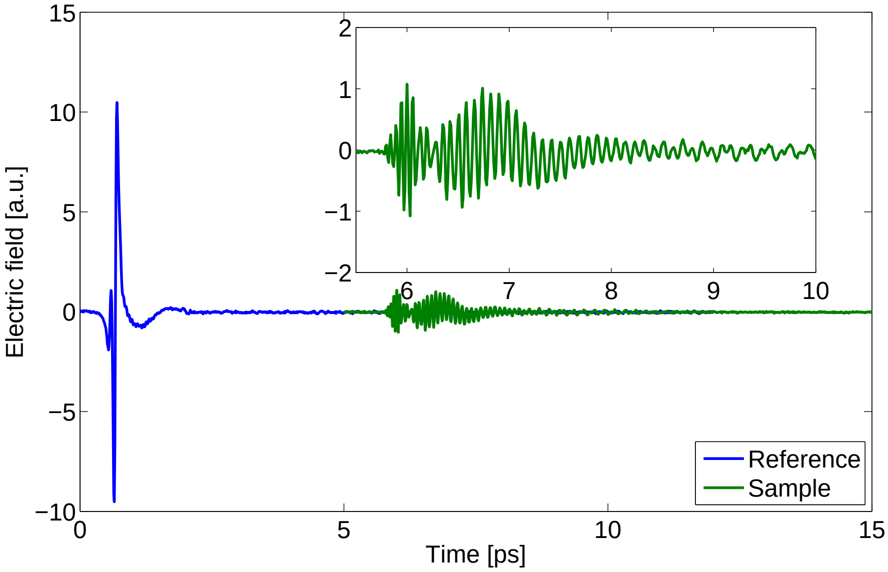

Figure B.36:

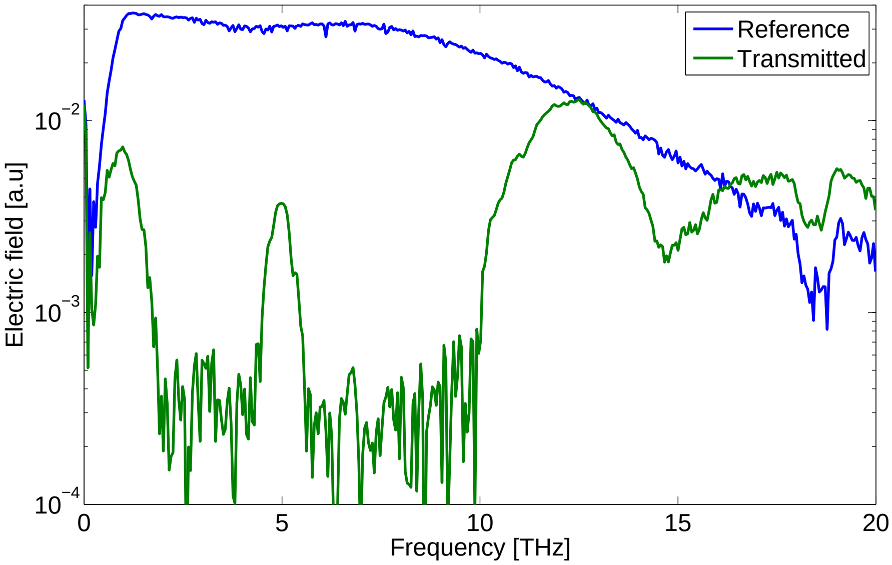

Figure B.37:

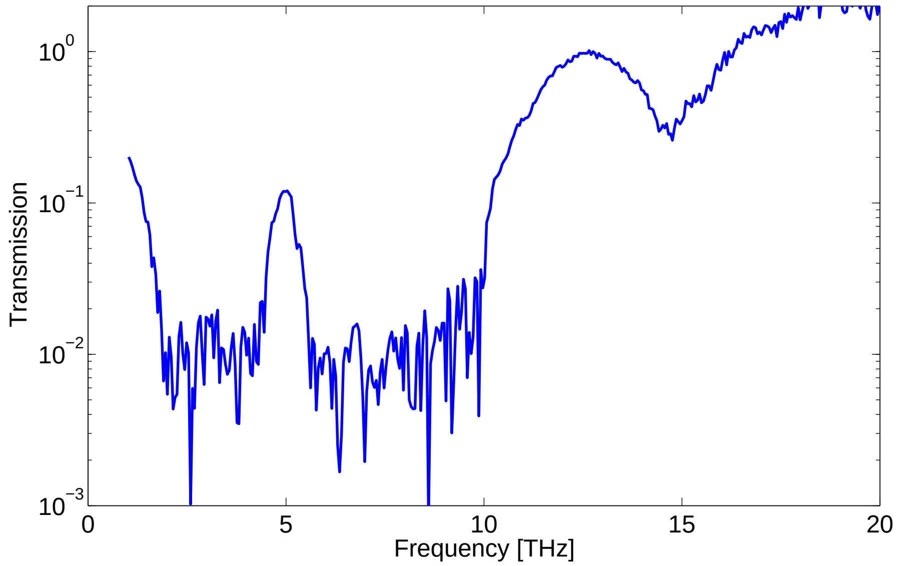

Figure B.38:

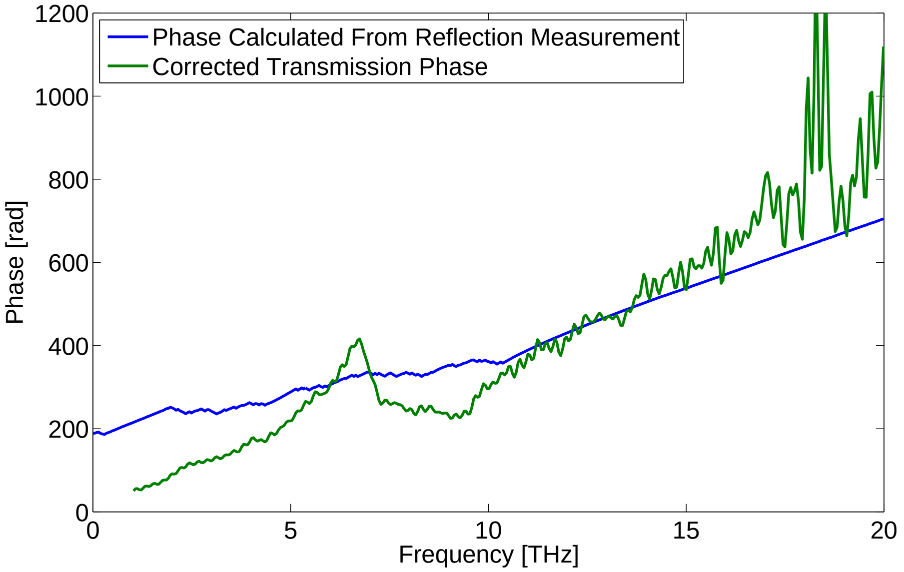

Figure B.39:

B.3.4 $Ge_{33}As_{12}Se_{55}$

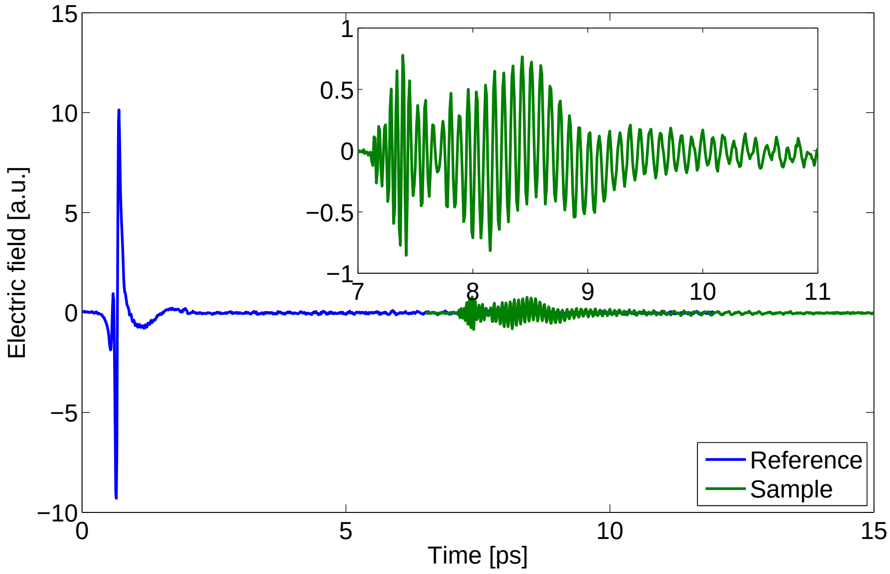

Figure B.40:

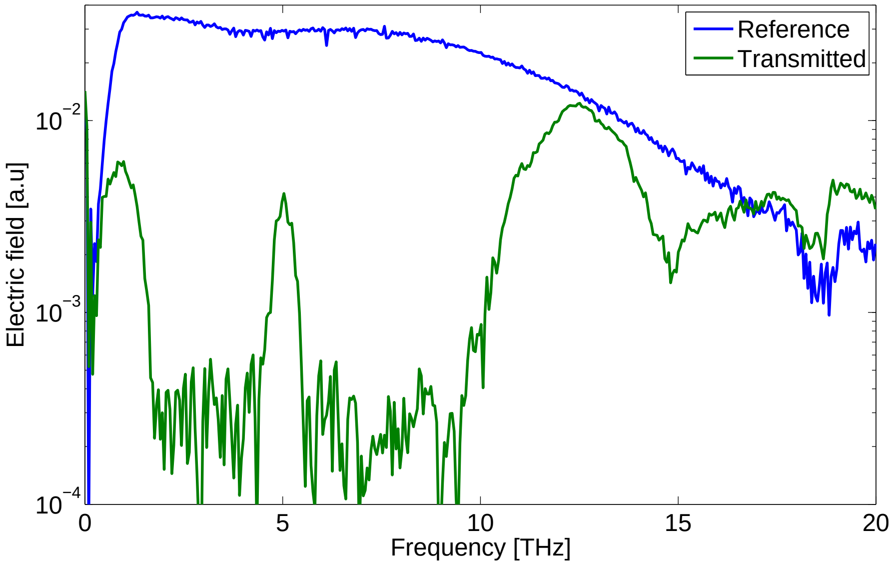

Figure B.41:

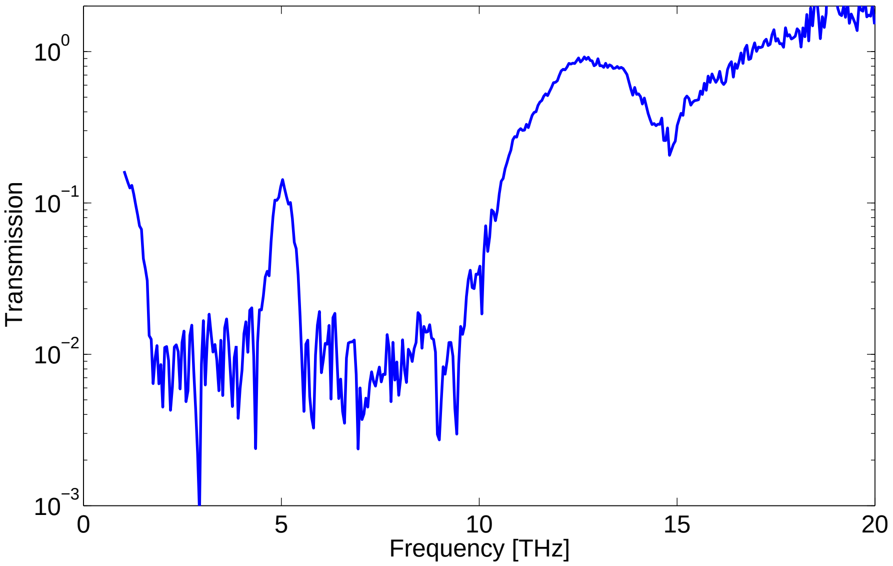

Figure B.42:

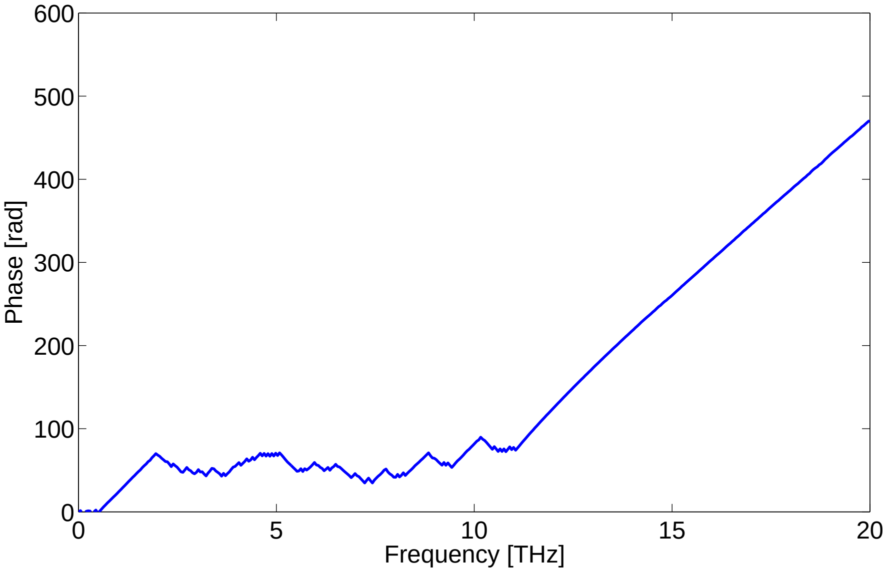

Figure B.43:

B.4 FTIR

B.4.1 $Ge_{11}As_{22}Se_{67}$

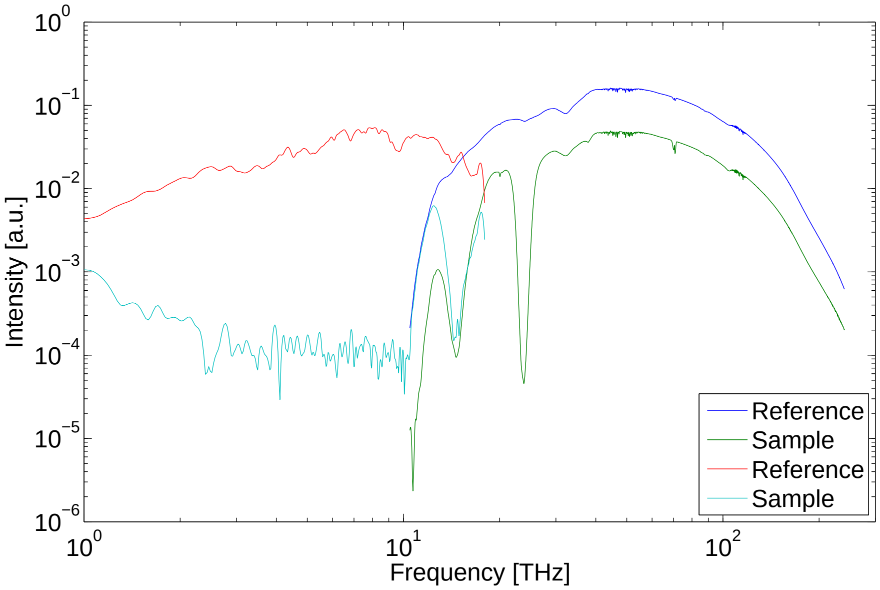

Figure B.44:

B.4.2 $\mathbf{Ge_{15}As_{20}Se_{65}}$

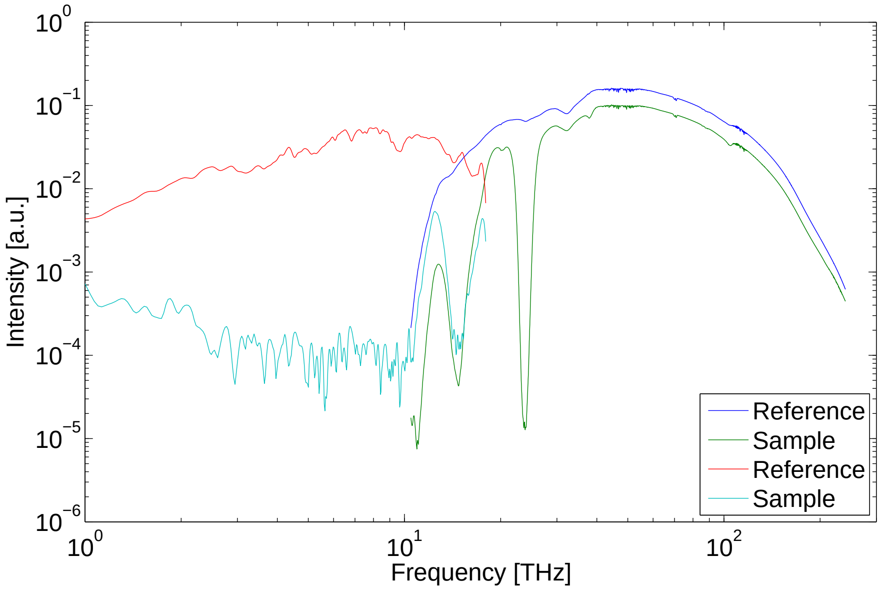

Figure B.45:

B.4.3 $Ge_{15}As_{25}Se_{60}$

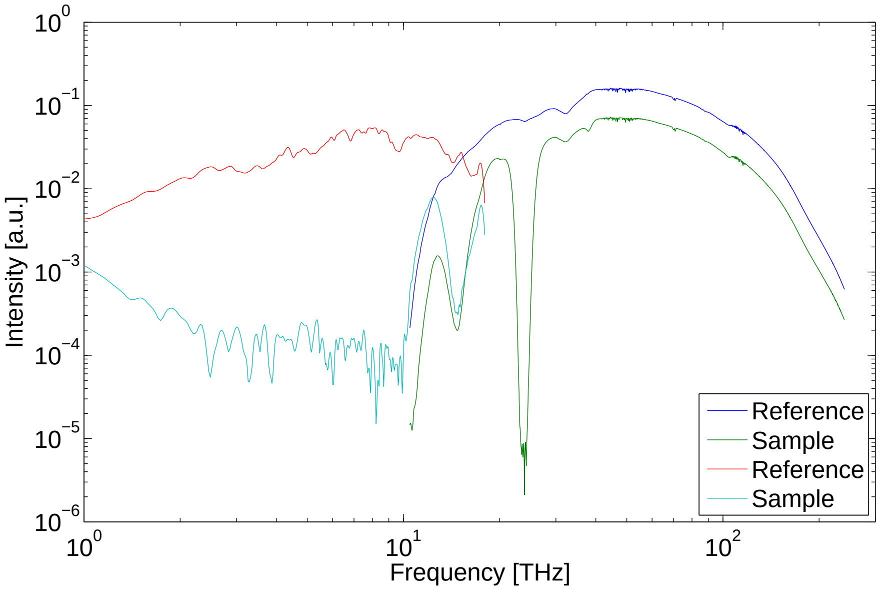

Figure B.46:

B.4.4 $\mathbf{Ge_{33}As_{12}Se_{55}}$

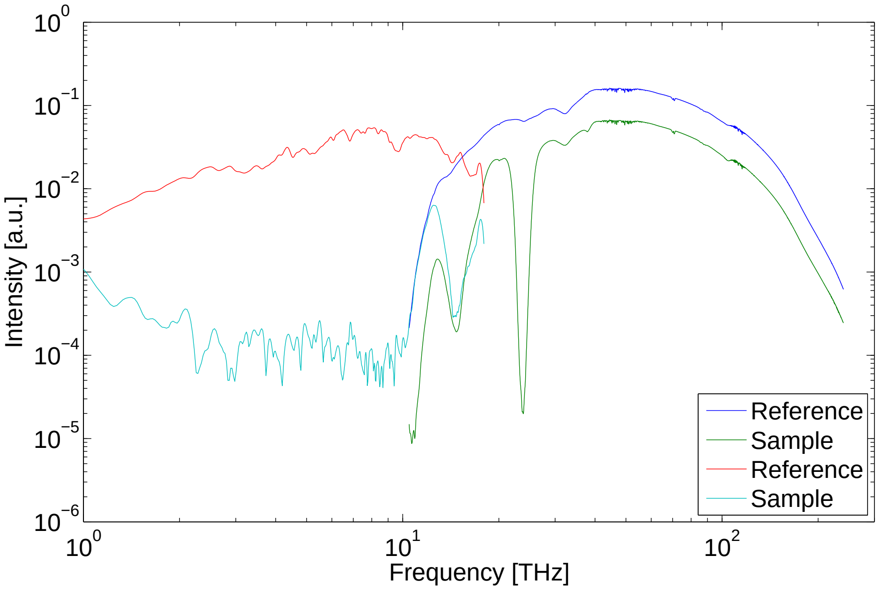

Figure B.47:

List of Symbols

α	Linear loss.
β	Propagation constant. The subscript refers to the number of derivations with respect to ω that has been performed on the constant. Noticeably, the first order derivative, β_1 is the reciprocal of the group velocity and the second order derivative, β_2 is proportional to the Group Velocity Dispersion (GVD).
β_{TPA}	The Two-Photon Absorption (TPA) constant.
γ	Nonlinear constant. The subscript refers to the number of derivations with respect to ω that has been performed on the constant. The superscripts r and i refers respectively to either the real or imaginary part of γ.
$\delta(t)$	Dirac delta function. The key property of this function is that $\int f(t)\delta(t-t_0)\mathrm{d}t = f(t_0)$.
κ	The imaginary part of the complex refractive index. Is proportional to the linear loss.
λ	Wavelength.
μ	Quadratic chirp.
Φ	Phase of the electric field.
ϕ	Phase of the electric field.
ω	Angular frequency.
Ω	Difference in angular frequency between the actual angular frequency ω and a reference angular frequency ω_0.
A_{eff}	Effective modal area.

b	Soliton angular frequency shift.
c	Speed of light.
C	Normalized quadratic chirp.
D	Dispersion.
E	Energy.
f_R	Fraction of the nonlinear response function caused by the instantaneous electronic response.
$h_R(t)$	Raman response function. The non-instantaneous part of the nonlinear response function.
i	Imaginary number.
I_1	The third of the five moments used in the Method of Moments (MoM). If normalized by the energy is equal to the center of the pulse in time.
I_2	The fourth of the five moments used in the MoM.
I_3	The fifth of the five moments used in the MoM.
L	Length.
$\tilde{n}$	The complex refractive index.
n	The real part of the refractive index.
n_2	The nonlinear refractive index.
Q	The first of the five moments used in the MoM. Equals the energy of the pulse.
P	Power. When it occurs with the subscript zero it refers specifically to peak power.
P_M	The second of the five moments used in the MoM.
$R(t)$	Nonlinear response function as a material experience when a electric field is present.
t	Time. With the subscript c it denotes the center of the pulse.
T_0	Pulse width in time.

$u(z,t)$	The complex envelope function of the electric field.
z	Propagation direction.
∂_x^n	Partial differential operator with respect to x differentiated n times.

List of Acronyms

ABCD	Air Based Coherent Detection
BS	Beam Splitter
β-**BBO**	β-Barium Borate
FFT	Fast Fourier Transform
FOM	Figure of Merit
fs	femtosecond
FTIR	Fourier Transform Infra Red
FWM	Four Wave Mixing
FWHM	Full Width Half Maximum
GNLS	Generalized Nonlinear Schrödinger
GVD	Group Velocity Dispersion
HMFG	Heavy Metal Flouride Glass
MI	Modulation Instability
MMF	Multi-Mode Fiber
MoM	Method of Moments
NLS	Nonlinear Schrödinger
OSA	Optical Spectrum Analyzer
PCF	Photonic Crystal Fiber
RHS	Right Hand Side

SC	Supercontinuum
SCG	Supercontinuum Generation
SHG	Second Harmonic Generation
SMF	Single-Mode Fiber
SNR	Signal-to-Noise Ratio
SSFS	Soliton Self Frequency Shift
THz-TDS	THz Time Domain Spectroscopy
TOD	Third Order Dispersion
TPA	Two-Photon Absorption
TRTS	Time Resolved THz Spectroscopy
ZDW	Zero Dispersion Wavelength

Bibliography

[1] H. B. Gray, *Chemical Bonds: An Introduction to Atomic and Molecular Structure.* University Science Books, 1994.

[2] P. Rolfe, "In vivo near-infrared spectroscopy," *Annu. Rev. Biomed. Eng.*, vol. 02, pp. 715–754, 2000.

[3] B. Guo, Y. Wang, C. Peng, H. L. Zhang, G. P. Luo, H. Q. Le, C. Gmachl, D. L. Sivco, M. L. Peabody, and A. Y. Cho, "Laser-based mid-infrared reflectance imaging of biological tissues," *Optics Express*, vol. 12, pp. 208–219, 2004.

[4] P. U. Jepsen, D. G. Cooke, and M. Koch, "Terahertz spectroscopy and imaging - modern techniques and applications," *Laser Photonics Rev.*, vol. 5, pp. 124–166, January 2011.

[5] S. D. Jackson, "Single-transverse-mode 2.5-w holmium-doped fluoride fiber laser operating at 2.86 μm," *Optics Letters*, vol. 29, pp. 334–336, Feb 2004.

[6] Y. Yao, A. J. Hoffman, and C. F. Gmachl, "Mid-infrared quantum cascade lasers," *Nature Photonics*, vol. 6, pp. 432–439, 2012.

[7] A. Schliesser, N. Picqué, and T. W. Hänsch, "Mid-infrared frequency combs," *Nature Photonics*, vol. 6, pp. 440–449, 2012.

[8] J. Hebling, K.-L. Yeh, M. C. Hoffmann, B. Bartal, and K. A. Nelson, "Generation of high-power terahertz pulses by tilted-pulse-front excitation and their application possibilities," *Journal of Optical Society of America B*, vol. 25, pp. B6–B19, July 2008.

[9] D. Buccoliero, H. Steffensen, O. Bang, H. Ebendorff-Heidepriem, and T. M. Monro, "Thulium pumped high power supercontinuum in loss-determined optimum lengths of tellurite photonic crystal fiber," *Applied Physics Letters*, vol. 97, p. 061106, August 2010.

[10] D. D. Hudson, S. A. Dekker, E. C. Mägi, A. C. Judge, S. D. Jackson, E. Li, J. S. Sanghera, L. B. Shaw, I. D. Aggarwal, and B. J. Eggleton, "Octave spanning

supercontinuum in an As_2S_3 taper using ultralow pump pulse energy," *Optics Letters*, vol. 36, pp. 1122–1124, April 2011.

[11] C. Agger, C. Petersen, S. Dupont, H. Steffensen, J. K. Lyngsø, C. L. Thomsen, J. Thøgersen, S. R. Keiding, and O. Bang, "Supercontinuum generation in ZBLAN fibers - detailed comparison between measurement and simulation," *Journal of Optical Society of America B*, vol. 29, pp. 635–645, April 2012.

[12] K. Nielsen, H. K. Rasmussen, A. J. Adam, P. C. Planken, O. Bang, and P. U. Jepsen, "Bendable, low-loss topas fibers for the terahertz frequency range," *Optics Express*, vol. 17, pp. 8592–8601, May 2009.

[13] S. Atakaramians, S. A. V., H. Ebendorff-Heidepriem, M. Nagel, B. M. Fischer, D. Abbott, and T. M. Monro, "Thz porous fibers: design, fabrication and experimental characterization," *Optics Express*, vol. 17, pp. 14053–15062, Aug 2009.

[14] J. S. Wang, E. M. Vogel, and E. Snitzer, "Tellurite glass: a new candidate for fiber devices," *Optical Materials*, vol. 3, pp. 187–203, August 1994.

[15] J. M. Parker, "Flouride glasses," *Annu. Rev. Mater. Sci*, vol. 19, pp. 21–41, 1989.

[16] X. Zhu and N. Peyghambarian, "High-power zblan glass fiber lasers: Review and prospect," *Advances in OptoElectronics*, vol. 2010, p. 501956, 2010.

[17] D. Szebesta, S. Davey, J. Williams, and M. Moore, "Ohabsorption in the lowlosswindow of zblan(p) glassfibre," *J. Non-Cryst. Solids*, vol. 161, pp. 18–22, 1993.

[18] X. Feng, W. H. Loh, J. C. Flanagan, A. Camerlingo, S. Dasgupta, P. Petropoulos, P. Horak, K. E. Frampton, N. M. White, J. H. Price, H. N. Rutt, and D. J. Richardson, "Single-mode tellurite glass holey fiber with extremely large mode area for infrared nonlinear applications," *œ*, vol. 16, pp. 13651–13656, September 2008.

[19] E. R. M. Taylor, L. N. Ng, J. Nilsson, R. Caponi, A. Pagano, M. Potenza, and B. Sordo, "Thulium-doped tellurite fiber amplifier," *IEEE Photonics Technology Letters*, vol. 16, no. 3, pp. 777–779, 2004.

[20] P. Domachuk, N. A. Wolchover, M. Cronin-Golomb, A. Wang, A. K. George, C. M. B. Cordeiro, J. C. Knight, and F. G. Omenetto, "Over 4000 nm bandwidth of mid-ir supercontinuum generation in sub-centimeter segments of highly nonlinear tellurite PCFs," *Optics Express*, vol. 16, pp. 7161–7168, May 2008.

[21] L. B. S. Jas S. Sanghera and and I. D. Aggarwal, "Chalcogenide glass-fiber-based mid-ir sources and applications," *IEEE J. Sel. Top. Quantum Electron.*, vol. 15, no. 1, pp. 114–119, 2009.

[22] H. Nguyen, K. Finsterbusch, D. Moss, and B. Eggleton, "Dispersion in nonlinear figure of merit of As_2Se_3 chalcogenide fibre," *Electron. Lett.*, vol. 42, p. 20060605, May 2006.

[23] A. V. Kolobov, "Ohabsorption in the lowlosswindow of zblan(p) glassfibre," *J. Non-Cryst. Solids*, vol. 198-200, pp. 728–731, 1996.

[24] J. W. Fleming, "Material dispersion in lightguide glasses," *Electronics Letters*, vol. 14, pp. 326–328, May 1978.

[25] R. N. Brown and J. J. Hutta, "Material dispersion in high optical quality heavy metal fluoride glasses," *Applied Optics*, vol. 24, no. 24, pp. 4500–4503, 1985.

[26] R. E. Slusher, G. Lenz, J. Hodelin, J. Sanghera, L. B. Shaw, and I. D. Aggerwal, "Large raman gain and nonlinear phase shifts in high-purity as_2se_3 chalcogenide fibers," *Journal of Optical Society of America B*, vol. 21, no. 6, 2004.

[27] T. M. Monro and H. Ebendorff-Heidepriem, "Progress in microstrusctured optical fibers," *Annu. Rev. Mater. Res.*, vol. 36, pp. 467–495, 2006.

[28] J. H. V. Price, T. M. Monro, H. Ebendorff-Heidepriem, F. Poletti, P. Horak, V. Finazzi, J. Y. Y. Leong, P. Petropoulos, J. C. Flanagan, G. Brambilla, X. Feng, and D. J. Richardson, "Mid-IR supercontinuum generation from non-silica microstructured optical fibers," *IEEE J. Sel. Top. Quantum Electron.*, vol. 13, pp. 738–749, May/June 2007.

[29] J. Hu, C. R. Menyuk, L. B. Shaw, J. S. Sanghera, and I. D. Aggarwal, "Maximizing the bandwidth of supercontinuum generation in As_2Se_3 chalcogenide fibers," *Optics Express*, vol. 18, pp. 6722–6739, March 2010.

[30] M. K. Halimah, W. M. Daud, H. A. A. Sidek, A. W. Zaidan, and A. S. Zainal, "Optical properties of ternary tellurite glasses," *Materials Science-Poland*, vol. 28, no. 1, pp. 173–180, 2010.

[31] D. Buccoliero, H. Steffensen, H. Ebendorff-Heidepriem, T. M. Monro, and O. Bang, "Midinfrared optical rogue waves in soft glass photonic crystal fiber," *œ*, vol. 19, pp. 17973–17978, September 2011.

[32] H. Steffensen, C. Agger, and O. Bang, "Influence of two-photon absorption on soliton self-frequency shift," *Journal of Optical Society of America B*, vol. 29, pp. 484–492, March 2012.

[33] X. Feng, T. Monro, V. Finazzi, R. Moore, K. Frampton, P. Petropoulos, and D. Richardson, “Extruded singlemode, high-nonlinearity, tellurite glass holey fibre,” *Electron. Lett.*, vol. 41, July 2005.

[34] B. T. Soifer and J. L. Pipher, “Instrumentation for infrared astronomy,” *Ann. Rev. Astron. Astrophys.*, vol. 16, pp. 335–369, 1978.

[35] J. D. Monnie, “Optical interferometry in astronomy,” *Rep. Prog. Phys.*, vol. 66, pp. 789–857, 2003.

[36] S. Dupont, C. Pedersen, J. Thøgersen, C. Agger, O. Bang, and S. R. Keiding, “IR microscopy utilizing intense supercontinuum light source,” *Optics Express*, vol. 20, pp. 4887–4892, February 2012.

[37] P. Werle, F. Slemr, K. Maurer, R. Kormann, R. Mucke, and B. Janker, “Near- and mid-infrared laser-optical sensors for gas analysis,” *Opt. Lasers Eng*, vol. 37, no. 2-3, pp. 101–114, 2002.

[38] The Federation of American Scientists, “AN/AAQ-24 Directional Infrared Countermeasures (DIRCM),” *http://www.fas.org/man/dod-101/sys/ac/equip/an-aaq-24.htm.*

[39] J. M. Dudley, G. Genty, and S. Coen, “Supercontinuum generation in photonic crystal fiber,” *Reviews of Modern Physics*, vol. 78, pp. 1135–1184, October-December 2006.

[40] N. Savage, “Supercontinuum sources,” *Nature Photon.*, vol. 3, pp. 114–115, February 2009.

[41] C. Xia, M. Kumar, O. P. Kulkarni, M. N. Islam, F. L. Terry, M. J. Freeman, M. Poulain, and G. Mazé, “Mid-infrared supercontinuum generation to 4.5 μm in zblan fluoride fibers by nanosecond diode pumping,” *Optics Letters*, vol. 31, pp. 2553–2555, September 2006.

[42] G. Qin, X. Yan, C. Kito, M. Liao, C. Chaudhari, T. Suzuki, and Y. Ohishi, “Ultrabroadband supercontinuum generation from ultraviolet to 6.28 μm in a fluoride fiber,” *Applied Physics Letters*, vol. 95, p. 161103, 2009.

[43] D.-I. Yeom, E. C. Mägi, M. R. E. Lamont, M. A. F. Roelens, L. Fu, and B. J. Eggleton, “Low-threshold supercontinuum generation in highly nonlinear chalcogenide nanowires,” *Optics Letters*, vol. 33, pp. 660–662, April 2008.

[44] Corning SMF28 Optical Fiber Data Sheet *http://www.corning.com/WorkArea/showcontent.aspx?id=41261.*

[45] P. Russell, “Photonic crystal fibers,” *Science*, vol. 299, pp. 358–362, January 2003.

[46] W. Q. Zhang, S. Afshar V., and T. M. Monro, “A genetic algorithm based approach to fiber design for high coherence and large bandwidth supercontinuum generation,” *Optics Express*, vol. 17, pp. 19311–19327, October 2009.

[47] T. A. Birks, W. J. Wadsworth, and P. S. J. Russell, “Supercontinuum generation in tapered fibers,” *Optics Letters*, vol. 25, no. 19, pp. 1415–1417, 2000.

[48] A. Kudlinski, A. K. George, J. C. Knight, J. C. Travers, A. B. Rulkov, S. V. Popov, and J. R. Taylor, “Zero-dispersion wavelength decreasing photonic crystal fibers for ultraviolet-extended supercontinuum generation,” *Optics Express*, vol. 14, no. 12, pp. 5715–5722, 2006.

[49] S. T. Sørensen, A. Judge, C. L. Thomsen, and O. Bang, “Optimum tapers for increasing the power in the blue-edge of a supercontinuum - group-acceleration matching,” *Optics Letters*, vol. 36, no. 6, pp. 816–818, 2011.

[50] C. Agger, S. T. Sørensen, C. L. Thomsen, S. R. Keiding, and O. Bang, “Nonlinear soliton matching between optical fibers,” *Optics Letters*, vol. 36, pp. 2596–2598, July 2011.

[51] IRflex Homepage *http://www.irflex.com/products/nonlinear-chalcogenide-mid-infrared-fiber.*

[52] CorActive Homepage *http://www.coractive.com/Chalco.html.*

[53] IrPhotonics Homepage *http://www.irphotonics.com/.*

[54] FiberLabs Homepage *http://www.fiberlabs-inc.com/.*

[55] L. G. Cohen, “Comparison of single-mode fiber dispersion measurement techniques,” *Journal of Lightwave Technology*, vol. LT-3, pp. 958–966, October 1985.

[56] J. Y. Lee and D. Y. Kim, “Versatile chromatic dispersion measurement of a single mode fiber usingspectral white light interferometry,” *œ*, vol. 14, pp. 11608–11615, November 2006.

[57] J. P. Gordon, “Theory of the soliton self-frequency shift,” *Optics Letters*, vol. 11, pp. 662–664, October 1986.

[58] E. N. Tsoy and C. M. de Sterke, “Dynamics of ultrashort pulses near zero dispersion wavelength,” *Journal of Optical Society of America B*, vol. 23, pp. 2425–2433, November 2006.

[59] A. M. Zheltikov, “Perturbative analytical treatment of adiabatically moderated soliton self-frequency shift,” *Physics Review E*, vol. 75, p. 037603, March 2007.

[60] A. C. Judge, O. Bang, B. J. Eggleton, B. T. Kuhlmey, E. C. Mägi, R. Pant, and C. Martijn de Sterke, “Optimization of the soliton self-frequency shift in a tapered photonic crystal fiber,” *Journal of Optical Society of America B*, vol. 26, pp. 2064–2071, November 2009.

[61] A. C. Judge, O. Bang, and C. Martijn de Sterke, “Theory of dispersive wave frequency shift via trapping by a soliton in an axially nonuniform optical fiber,” *Journal of Optical Society of America B*, vol. 27, pp. 2195–2202, November 2010.

[62] Z. Chen, A. J. Taylor, and A. Efimov, “Soliton dynamics in non-uniform fiber tapers: analytical description through an improved moment method,” *Journal of Optical Society of America B*, vol. 27, pp. 1022–1030, May 2010.

[63] G. P. Agrawal, *Nonlinear Fiber Optics.* Academic Press, 4 ed., 2007.

[64] L. Yin, Q. Lin, and G. P. Agrawal, “Soliton fission and supercontinuum generation in silicon waveguides,” *Optics Letters*, vol. 32, pp. 391–393, February 2007.

[65] A. I. Maimistov, “Evolution of single waves close to solitons of schrödinger nonlinear equation,”

[66] W. Krolikowski, O. Bang, N. Nikolov, D. Neshev, J. Wyller, J. Rasmussen, and D. Edmundson, “Modulational instability, solitons and beam propagation in nonlocal nonlinear media,” *J. Opt. B: Quantum Semiclass*, vol. 6, p. S288, 2004.

[67] Q. Kong, Q. Wang, O. Bang, and W. Krolikowski, “Analytical theory for dark nonlocal solitons,” *Optics Letters*, vol. 35, pp. 2152–2154, 2010.

[68] E. N. Tsoy, A. Ankiewicz, and N. Akhmediev, “Dynamical models for dissipative localized waves of the complex ginzburg-landau equation.,” *Physics Review E*, vol. 73, no. 3, p. 036621, 2006.

[69] J. Dudley and J. Taylor, *Supercontinuum Generation in Optical Fibers.* Cambridge University Press, 2010.

[70] M. C. H. J. Hebling, K.-L. Yeh and K. A. Nelson, “High-power thz generation, thz nonlinear optics, and thz nonlinear spectroscopy,” *IEEE J. Sel. Top. Quantum Electron.*, vol. 14, pp. 345–353, March/April 2008.

[71] N. Karpowicz, J. Dai, X. Lu, Y. Chen, M. Yamaguchi, H. Zhao, X.-C. Zhang, L. Zhang, C. Zhang, M. Price-Gallagher, C. Fletcher, O. Mamer, A. Lesimple, and K. Johnson, “Coherent heterodyne time-domain spectrometry covering the entire ”terahertz gap”,” *Applied Physics Letters*, vol. 92, p. 011131, 2008.

[72] M. M. Awad and R. A. Cheville, “Transmission terahertz waveguide-based imaging below the diffraction limit,” *Applied Physics Letters*, vol. 86, pp. 221107 –221107–3, may 2005.

[73] D. Chen and H. Chen, “A novel low-loss terahertz waveguide: Polymer tube,” *Optics Express*, vol. 18, pp. 3762–3767, Feb 2010.

[74] M. Lu, W. Li, and E. R. Brown, “Second-order bandpass terahertz filter achieved by multilayer complementary metamaterial structures,” *Optics Letters*, vol. 36, pp. 1071–1073, Apr 2011.

[75] R. Mendis, A. Nag, F. Chen, and D. M. Mittleman, “A tunable universal terahertz filter using artificial dielectrics based on parallel-plate waveguides,” *Applied Physics Letters*, vol. 97, pp. 131106 –131106–3, sep 2010.

[76] J. Li, “Terahertz modulator using photonic crystals,” *Optics Communications*, vol. 269, no. 1, pp. 98 – 101, 2007.

[77] H.-T. Chen, W. J. Padilla, M. J. Cich, A. K. Azad, R. D. Averitt, and A. J. Taylor, “A metamaterial solid-state terahertz phase modulator,” *Nature Photonics*, vol. 3, pp. 148–151, 2009.

[78] M. Zalkovskij, C. Z. Bisgaard, A. Novitsky, R. Malureanu, D. Savastru, A. Popescu, P. U. Jepsen, and A. V. Lavrinenko, “Ultrabroadband terahertz spectroscopy of chalcogenide glasses,” *Applied Physics Letters*, vol. 100, p. 031901, 2012.

[79] P. Kučel, H. Němec, F. Kadlec, and C. Kadlec, “Gouy shift correction for higly accurate refractive index retrieval in time-domain terahertz spectroscopy,” *Optics Express*, vol. 18, no. 15, pp. 15338–15348, 2010.

[80] Picometrix Homepage *http://www.picometrix.com/pico_products/terahertz_tr4000.asp.*

[81] T. Löffler, T. Hahn, M. Thomson, F. Jacob, and H. G. Roskos, “Large-area electro-optic ZnTe terahertz emitters,” *Optics Express*, vol. 41, July 2005.

[82] D. J. Cook and R. M. Hochstrasser, “Intense terahertz pulses by four-wave rectification in air,” *Optics Letters*, vol. 25, no. 16, pp. 1210–1212, 2000.

[83] M. Kress, T. Löffler, S. Eden, M. Thomson, and H. G. Roskos, "Terahertz-pulse generation by photoionization of airwith laser pulses composed of both fundamental and second-harmonicwaves," *Optics Letters*, vol. 29, no. 10, pp. 1120–1122, 2004.

[84] E. V. Loewenstein, "The history and current status of fourier transform spectroscopy," *Applied Optics*, vol. 5, p. 845, 1966.

[85] S. N. Taraskin, S. I. Simdyankin, S. R. Elliott, J. R. Neilson, and T. Lo, "Universal features of terahertz absorption in disordered materials," *Physics Review Letters*, vol. 97, no. 5, p. 055504, 2006.

[86] A. F. Ioffe and A. R. Regel, "Non-crystalline, amorphous and liquid electronic semiconductors," *Prog. Semicond*, 1960.

[87] M. C. Beard, G. M. Turner, and C. A. Schmuttenmaer, "Transient photoconductivity in gaas as measured by time-resolved terahertz spectroscopy," *Physical Review B*, vol. 62, pp. 15764–15777, December 2000.

[88] D. G. Cooke. PhD thesis.

[89] R. Ulbricht, E. Hendry, J. Shan, T. F. Heinz, and M. Bonn, "Carrier dynamics in semiconductors studied with time-resolved terahertz spectroscopy," *Rev. Mod. Phys.*, vol. 83, pp. 543–586, 2011.

[90] M. G. Kuzyk and C. W. Dirk, *Characterization Techniques and Tabulations for Organic Nonlinear Materials.* Marcel Dekker, 1 ed., 1998.

[91] L. Razzari, F. H. Su, G. Sharma, F. Blanchard, A. Ayesheshim, H.-C. Bandulet, R. Morandotti, J.-C. Kieffer, T. Ozaki, M. Reid, and F. A. Hegmann, "Nonlinear ultrafast modulation of the optical absorption of intense few-cycle terahertz pulses in n-doped semiconductors," *Physics Review B*, vol. 79, p. 193204, 2009.